FAR INFRARED SPECTROSCOPY OF $CsNiCl_3$ TYPE CRYSTALS

A thesis
submitted for the Degree
of
Doctor of Philosophy in Physics
in the
University of Canterbury

by

R.E.M. Vickers

University of Canterbury
1985

To

Helen

ACKNOWLEDGEMENTS

I wish to thank in particular my supervisor, Dr. John Campbell, for his support and availability throughout the term of my Ph.D. Drs. Glynn Jones and Rod Syme deserve a special thanks for taking a continuing interest in my work.

Ross Ritchie and K. K. Lai are thanked for help with growing crystals. Greg Haslett deserves credit for the hardware design in interfacing the PET microcomputer to the interferometer. Terry Rowe who did most of the mechanical work on the bolometer, I thank for always being willing to make yet another change to the bolometer. I also thank John de Voil for keeping the far infrared radiation source going and Bruce Bradshaw for building the stainless steel liquid nitrogen dewar.

Above all I thank my wife, Helen, and my parents for their constant support and encouragement.

ABSTRACT

A far infrared interferometer has been interfaced to a microcomputer and programs developed to enable fourier transform spectroscopy to be carried out in real time.

A He^3 cooled bolometer-superconducting magnet system has been constructed for far infrared Zeeman spectroscopy. The bolometer element is magnetically shielded from the field using superconducting lead.

The theory of the transmission of polarized radiation through slabs of non-isotropic dielectric crystals mounted on a dielectric substrate is developed. The resulting equations allow general features of far infrared transmission spectra to be examined. For example they show that for "thicker" crystals, the transverse optical mode absorption lines are asymmetric while the longitudinal optical mode absorption lines are symmetric. For large angles of incidence, an extra absorption line is predicted to occur above the longitudinal optic mode frequency for crystals of low dielectric constant.

The infrared-active phonon spectra of thirteen crystals of the $CsNiCl_3$ type structure are reported and assigned to specific lattice modes.

Using polarized, Zeeman spectroscopy, two magnon lines are identified in the quasi 1 dimensional antiferromagnet $RbCoBr_3$ at 100.0±0.5 cm^{-1} and 120.0±0.5 cm^{-1}, each having a g value of 3.8±0.4. These lines are fitted using a perturbed Ising model to give a longitudinal interchain exchange strength of 51 cm^{-1} and a relative longitudinal interchain exchange value of 0.06 for $RbCoBr_3$ at 1.7 K.

A possible antiresonance line is reported at 114.6 cm^{-1} for $RbCoBr_3$ and preliminary work is reported in the search for magnons in other $CsNiCl_3$ type crystals.

CONTENTS

CHAPTER Page

1 INTRODUCTION

2 EXPERIMENTAL

FIGURES

LIST OF TABLES

CHAPTER 1

INTRODUCTION

1.1 THE AIMS OF THIS WORK

The first objective of this project was to upgrade the far infrared interferometer so that it would be under computer control and spectra could be obtained in real time. The second phase was to design and construct a sensitive, He^3 cooled bolometer/superconducting magnet system to allow Zeeman studies of magnetic crystals, particularly those which are under intensive investigation by the solid state research group.

With these improvements, a study of magnons in quasi one-dimensional antiferromagnets of the $CsNiCl_3$ type structure was to be carried out. To do this it would first be necessary to have a full understanding of the phonons in these crystals. The phonon study also necessitated the development of the theory for the transmission of off-axis electromagnetic radiation through a non-isotropic dielectric supported by an isotropic substrate.

1.2 FAR INFRARED SPECTROSCOPY

The standard sources available for the far infrared region of the electromagnetic spectrum are essentially black bodies. The radiation intensity produced by these sources in this region ($10cm^{-1}$ to $1000cm^{-1}$) is quite small since we are operating in the long wavelength tail of a blackbody curve.

Dispersive techniques further reduce the intensity at the detector by several orders of magnitude. These handicaps are minimized by using interferometric techniques (where all the radiation is incident on the detector) and sensitive detectors.

Interferometry relies on the interference between two coherent radiation beams whose relative path difference can be varied. This produces a record of intensity versus path difference (an interferogram). A Fourier transform of the interferogram produces a plot of intensity versus frequency (a spectrum).

A real time system calculates the spectrum as the interferogram is being produced. A low resolution spectrum can be calculated as soon as the first few points of the interferogram have been recorded. As more of the interferogram is collected (as the path difference is increased) so the resolution of the calculated spectrum increases. Thus a real time process enables decisions to be made on the suitability of the experimental conditions without waiting to collect a full interferogram. This represents a large increase in useful experimental time. The interfacing of a computer to the interferometer and the design of software to control the interferometer and to calculate spectra in real time was therefore a vital part of this project.

Detectors of thermal radiation (low photon energy) rely on the incoming radiation heating the device and changing some measurable property of the device. This can be gas pressure (as in the Golay cell), pyroelectricity (pyroelectric detector), electron mobility (InSb Rollin detector) or electrical resistance (bolometer). It is the latter that is the most common.

Simple resistance thermometers can be used as bolometers. However for a very sensitive bolometer the change in resistance must be as large as possible for a given small heat input. The most sensitive use superconductors near their critical temperature. These have the serious defect that the temperature control of the element must be maintained to within 1/1000th of a degree Kelvin.

The most common type of bolometers use semiconductors such as carbon resistors or doped germanium crystals. For these, the temperature coefficient of resistance increases markedly at low temperatures so doped germanium bolometers are operated at the very low temperatures of 4.2K (liquid helium), 1.5K (pumped liquid helium), 0.4K (pumped liquid He^3 isotope) or 0.1K (He^3-He^4 dilution refrigerator).

For this work a He^3-cooled, germanium bolometer with a miniature, closed refrigerator was designed and built. This method of cooling was chosen because of the simplicity of the refrigerator design. The new bolometer along with a new cryostat was constructed so that a superconducting magnet could be incorporated into the system. This enabled investigations to be carried out on the effect of a magnetic field on excitations within a crystal.

1.3 MAGNONS IN CSNICL$_3$ TYPE CRYSTALS

In a magnetically ordered structure in its lowest energy state the magnetic moment of a magnetic ion or atom is in a fixed direction with respect to the nearest magnetic neighbours. In a ferromagnetic material they are parallel; for a canted ferromagnet, a fixed but small angle; for an antiferromagnet, antiparallel.

If/the orientation of one magnetic moment is disturbed the disturbance can propogate through the crystal. By analogy with atomic displacement waves travelling through a crystal (phonons), the propagating magnetic disturbance is called a spin wave or magnon. The quantum of energy associated with the wave gives information about the magnetic forces in the system.

Many different techniques can be used for studying magnetic effects; including magnetic susceptibility, sidebands on optical spectra, electron spin resonance, nuclear magnetic resonance, neutron diffraction, Raman spectroscopy and far infrared spectroscopy. The latter two techniques have the advantage of being able to observe directly and accurately the magnons at the Brillouin zone centre (K=0).

The magnetic case that is most simple to treat theoretically is the one-dimensional chain of ordered magnetic moments. One system that has been found to be nearly one dimensional is the CsNiCl$_3$ type structure where the magnetic transition metal ions (Mn,Fe,Co,Ni) form antiferromagnetically ordered linear chains which are well separated from each other.

Raman spectroscopy has proved a useful tool for investigating magnons in these structures but many of the crystals are highly absorbing in the visible spectrum which reduces the scattering efficiency and makes it hard to identify the magnon lines. More recently far infrared laser techniques, together with conventional far-infrared absorption, have been used to study the magnon spectra.

So far only $CsCoCl_3$, $CsCoBr_3$ and $RbCoCl_3$ have been extensively studied using these techniques. This thesis reports work using far infrared absorption, together with an applied magnetic field, to investigate magnons in $RbCoBr_3$. Preliminary work has also been attempted to identify magnons in other $CsNiCl_3$ type crystals.

1.4 PHONONS IN $CsNiCl_3$ TYPE CRYSTALS

A full knowledge of the phonon spectra of these crystals helps in the identification and understanding of the magnon spectra. Because the crystal structure has a centre of inversion the phonons seen by Raman spectroscopy and infrared absorption are mutually exclusive. As shown in chapter 4, the infrared spectra consists of two phonons polarized parallel to the crystal c axis (i.e. parallel to the transition metal chains) and three phonons polarized perpendicular to the c axis. Accurate positions for the infrared active phonons have not been previously reported. To obtain accurate line positions thin, single crystals are needed. Single crystal samples also have the advantage that polarized spectra may be obtained which is often helpful in lessening the chance of a phonon absorption obscuring any magnons present.

1.5 RADIATION TRANSMISSION THROUGH A DIELECTRIC SLAB

For thin, isotropic crystals with radiation at normal incidence the minimum transmission is at the frequency of the transverse optic phonon. At non-normal incidence another minimum occurs at the longitudinal optic phonon frequency.

For this project a theoretical study was undertaken to determine expressions governing the transmission of electomagnetic radiation through anisotropic, thin crystals. This was then used to explain the absorption spectra of $CdCl_2$ type crystals. The theory was later generalised to the case of an anisotropic slab of any thickness. For the $CsNiCl_3$ crystals the theory had to be extended to include several different phonon modes in each crystallographic direction.

1.6 STRUCTURE OF THIS THESIS

Chapter 2 covers the experimental aspects of this work; the computer control of the interferometer, the computation of spectra in real time, the design and construction of the new bolometer, and the development of techniques of crystal growth and sample preparation.

The theory of transmission of electromagnetic radiation through thick slabs of anisotropic dielectric is developed in chapter 3. The published paper in appendix 2 summarizes this for the limited case of thin films.

Chapter 4 presents the general theory of factor group analysis and normal mode co-ordinate analysis for phonons in crystals. This is then applied specifically to the $CsNiCl_3$ type crystal structure. The polarized, infrared-active phonon spectra of these crystals is reported and discussed in the latter half of this chapter.

Chapter 5 summarizes the current theory of magnons in cobalt compounds of the $CsNiCl_3$ structure. Experimental results for the magnons in $RbCoBr_3$ are presented and compared to those in $CsCoCl_3$. A possible antiresonance line in $RbCoBr_3$ is also reported. The last part of this chapter outlines preliminary work undertaken for the search for magnons in other transition metal compounds of this type.

A short conclusion in chapter 6 examines how the aims of this thesis have been fulfilled and suggests further avenues of study that have been raised by this work.

CHAPTER 2

EXPERIMENTAL

The far infrared spectra were obtained using a Grubb Parsons IS3 Michelson interferometer. A Commodore PET microcomputer was interfaced to it to control the machine and to calculate the resulting spectra in real time.

A small He^3 cooled, doped germanium bolometer with a multiple sample holder is used for most of the spectra presented in this work. This bolometer (Vickers 1981) needed to be modified to eliminate minor problems in its He^3 refrigerator. Because of the success of this bolometer a new He^3 cooled bolometer equipped with a 5 Tesla superconducting magnet was developed for Zeeman measurements. The larger size of the new bolometer and magnet required a new cryostat system to be designed and constructed.

New techniques were developed to obtain thin samples of $CsNiCl_3$ type crystals.

2.1 COMPUTER CONTROL OF THE INTERFEROMETER AND REAL TIME FOURIER TRANSFORM CALCULATIONS.

At the start of this project the Fourier transform calculations to produce the spectra were carried out on the University's mainframe computer, a Burroughs B6700. This required the interferogram to be collected on papertape which was then carried over to the computer centre. Under the best circumstances a spectrum could be obtained half an hour after the interferogram had been produced, but often a wait of several hours (and sometimes overnight) was necessary if the queues were long. This was a most inefficient use of experimental time particularly when the usual shortage of liquid helium meant that every run should count. Many a run was wasted on a sample that was not optimum either in thickness, concentration or cutoff frequency.

A major experimental aim of this project was to interface a microcomputer to the interferometer to control the interferometer , to collect data and to compute the spectrum in real time. A real time computation is advantageous in that with only a few points of the interferogram collected a low resolution spectrum can be produced. The spectrum is initially of poor resolution but as more data is collected the resolution improves. At any time then the operator can decide to terminate that particular spectral run.

2.1.1 Computer Interface and Program Development

To collect data and do a real time Fourier transform calculation on it requires that the computer have full control of the interferometer. Without this full control there is a danger that the interferometer will get out of step with the computer and the computer thinks that, for example, it is calculating the nth point while the interferometer has actually stepped beyond the (n+1)th point.

The computer used to control the interferometer is a Commodore PET model 4032. The system is interfaced to the interferometer by the addition of a graphics board, two 8 bit digital-to-analog converters (D-A), a 12 bit analog to digital converter (A-D), a board to drive the stepping motor and a PIA board to control the pen up/down function on an x-y chart recorder and to test a stepping motor limit switch.

The graphics board enables the computer to display a screen with 312 times 198 pixles which gives enough resolution to display as standard a spectrum 250 wavenumbers wide with one wavenumber resolution. The eight bit D-As are useful for drawing the spectra on an x-y chart recorder. All the interface boards are driven from the KIM bus of the graphics board (figure 2.1). All the electronic parts of the interfacing were designed and built by Physics Department technicians.

In controlling the interferometer the computer reads the signal from the lock-in amplifier, outputs this data immediately to a 5.25 inch floppy disc, advances the stepping motor, and then calculates that points contribution to the Fourier transform. The computer then checks if the correct time interval has passed and repeats the process.

The Fourier transform ideally should not take more time than the desired time interval between successive steps of the interferometer. The implementation of the real time transform was dependent on the computer therefore being able to calculate the transform within one second, the normal stepping time. This only proved possible by writing large sections of the transform program in machine code as well as providing a "look up" cosine table rather than calculating it each time. For a calculation of 250 spectral points the time

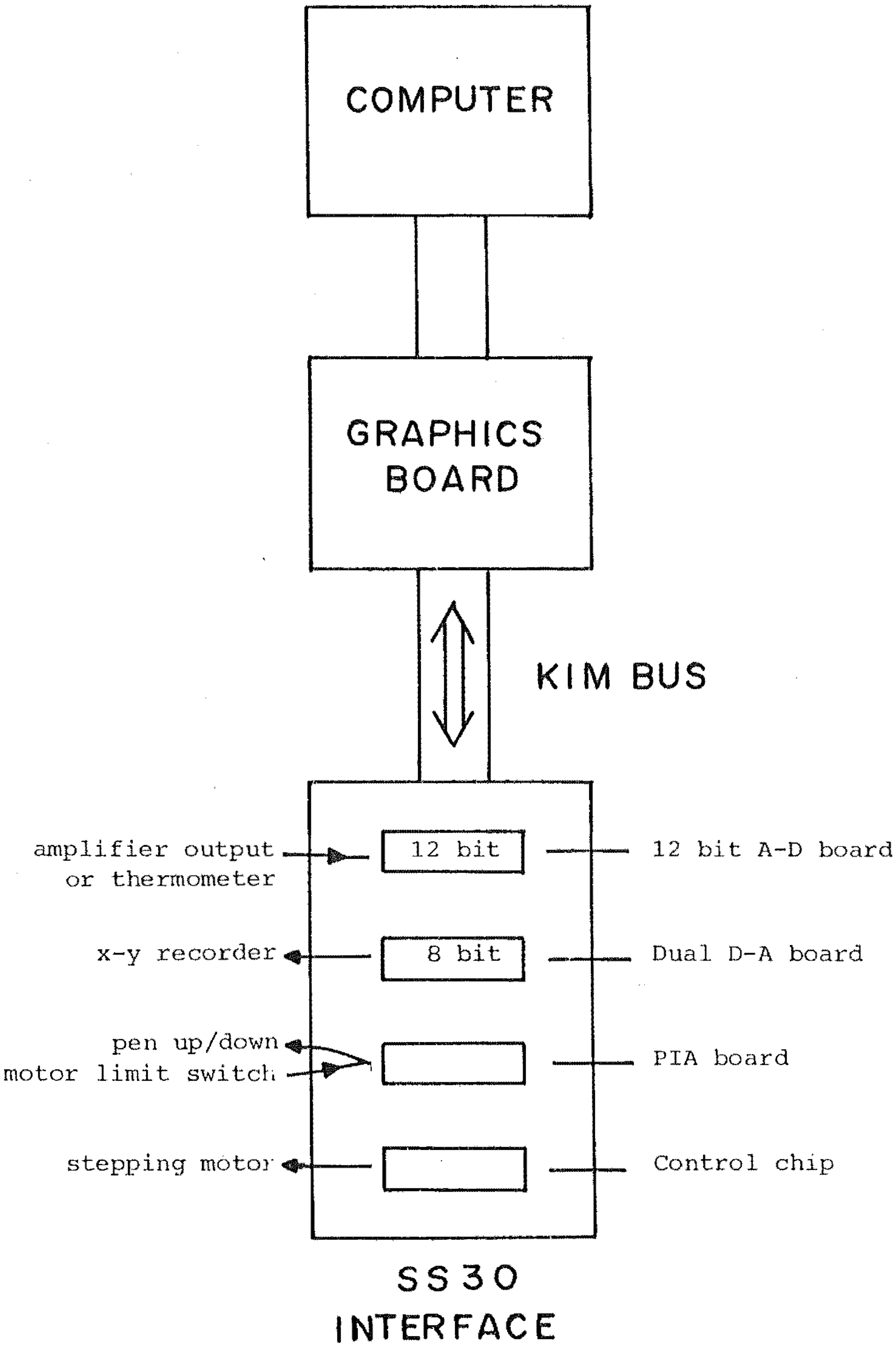

FIGURE 2.1 Interface between microcomputer and interferometer

taken was 0.6 seconds (see appendix 1 for the text of the program). The calculation could be sped up by putting more of the program in machine code, but round-off errors were then introduced into the calculation. A combination of Basic and machine code was the most suitable.

The operation of the interferometer had to cease whilst the computer updated the spectrum on the screen, a process which took 15 seconds. Initially the screen was updated every fifty data points. This added approximately a third to the time taken to obtain one spectrum. It was therefore found more convenient to update the screen automatically after 2 points and at the end of the run. In between it could be updated on demand by pushing U on the keyboard.

2.1.2 The Fourier Transform

The far infrared interferometer is a two beam interferometer which produces a record (the interferogram) of intensity as a function of difference in path length of the two beams. The Fourier transform of the interferogram produces a plot of intensity as a function of frequency (the spectrum). In theory the transform should be calculated for all points between a path difference of minus infinity to plus infinity. This is of course impractical. In practice interferograms are collected using finite sampling intervals and finite path differences.

Sampling at finite intervals introduces no errors into the spectrum provided the maximum frequency (in reciprocal wavelength) of the spectrum is less than the inverse of twice the stepping interval (Bell 1972). This means that if the cut-off frequency of the spectrum is low then the stepping interval can be large and so for a given maximum path difference the interferogram can be collected more quickly.

Scanning over a finite path difference range (-L to +L) limits the resolution of the spectrum to approximately 1/L. The truncating of the interferogram at -L and L also introduces into the spectrum negative intensities and side lobes. This problem can be overcome, with a slight degradation in resolution, by apodization of the interferogram. In this technique the interferogram is multiplied by a smoothly varying function that is maximum at zero path difference and zero at the maximum path difference(L). Typical apodizing functions are $1-x/L$ and $\mathrm{Cos}(\pi x/2L)$.

If the interferogram from 0 to L and from 0 to -L is identical then a Cosine transform can be used with a resulting simplification of the computation of spectrum. Also in this case only one side needs to be collected and the time taken to collect an interferogram and calculate the spectrum is halved.

The biggest practical problem with this method is that the interferogram is not always sampled at exactly zero path difference (the central maximum intensity point). This error (the zero error) introduces an asymmetry into the interferogram. However in practise this can be taken into account by a small modification to the single-sided Fourier transform. The asymmetry, and indeed all linear phase errors, can be eliminated by fitting a parabola to the points just before and just after the maximum point to locate the true central maximum and find a value for the zero error (figure 2.2). The Fourier transform is then calculated with the zero error (e) added to the path difference i.e. the interferogram is effectively from 0+e to L+e. The effect of having a zero error in the sampled interferogram can be seen in figure 2.3. The result is a "tilt" in the calculated spectrum.

The real time, single sided, linear apodized, cosine, Fourier transform used is as follows (Bell 1972):

$$I(\nu) = 2*\sum_{n}[I(n\Delta+e)-I(\infty)]*(1-\frac{n}{n'})\cos(2\pi(n*\Delta+e)*\nu)$$

where

ν is the frequency in wavenumbers (reciprocal centimetres)

Δ is the distance of each step in centimetres

n is the number of points from the central maximum

n' is the maximum number of points to be sampled

$1-\frac{n}{n'}$ is the linear apodization function

e is the zero error calculated from

$$e = \frac{I(1)+I(-1)}{2[I(-1)+I(1)-2I(0)]} * \Delta ,$$

I(0) being the maximum value in the interferogram and I(−1), I(+1) being the values of the points before and after the central point respectively.

A modification was made to the the above Fourier transform algorithm. The first point in the interferogram (I(0)) should only have half the contribution of the rest of the points in the single sided transform. This is because the

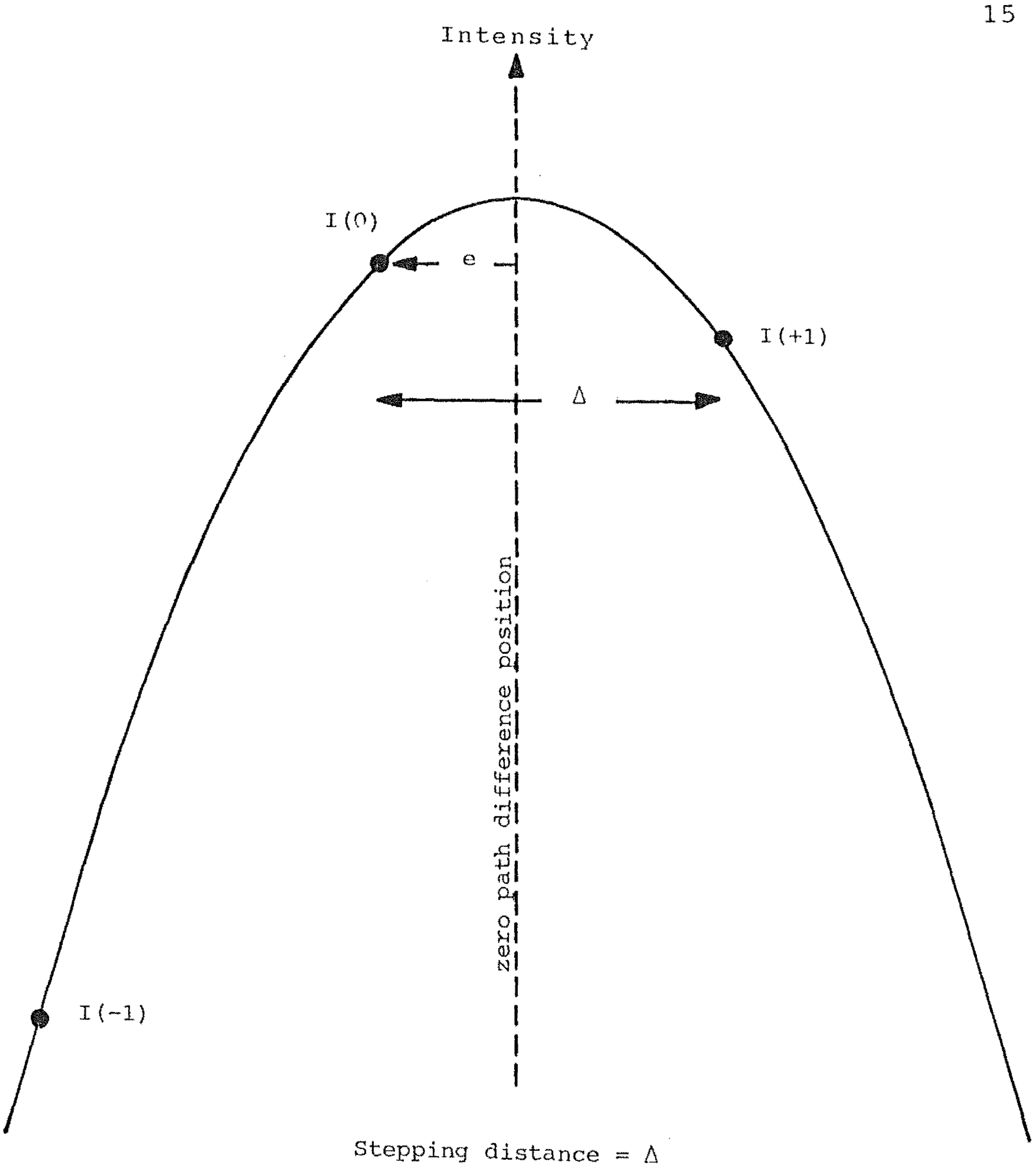

Figure 2.2 Fitting a parabola to the three central points to determine the zero error (e).

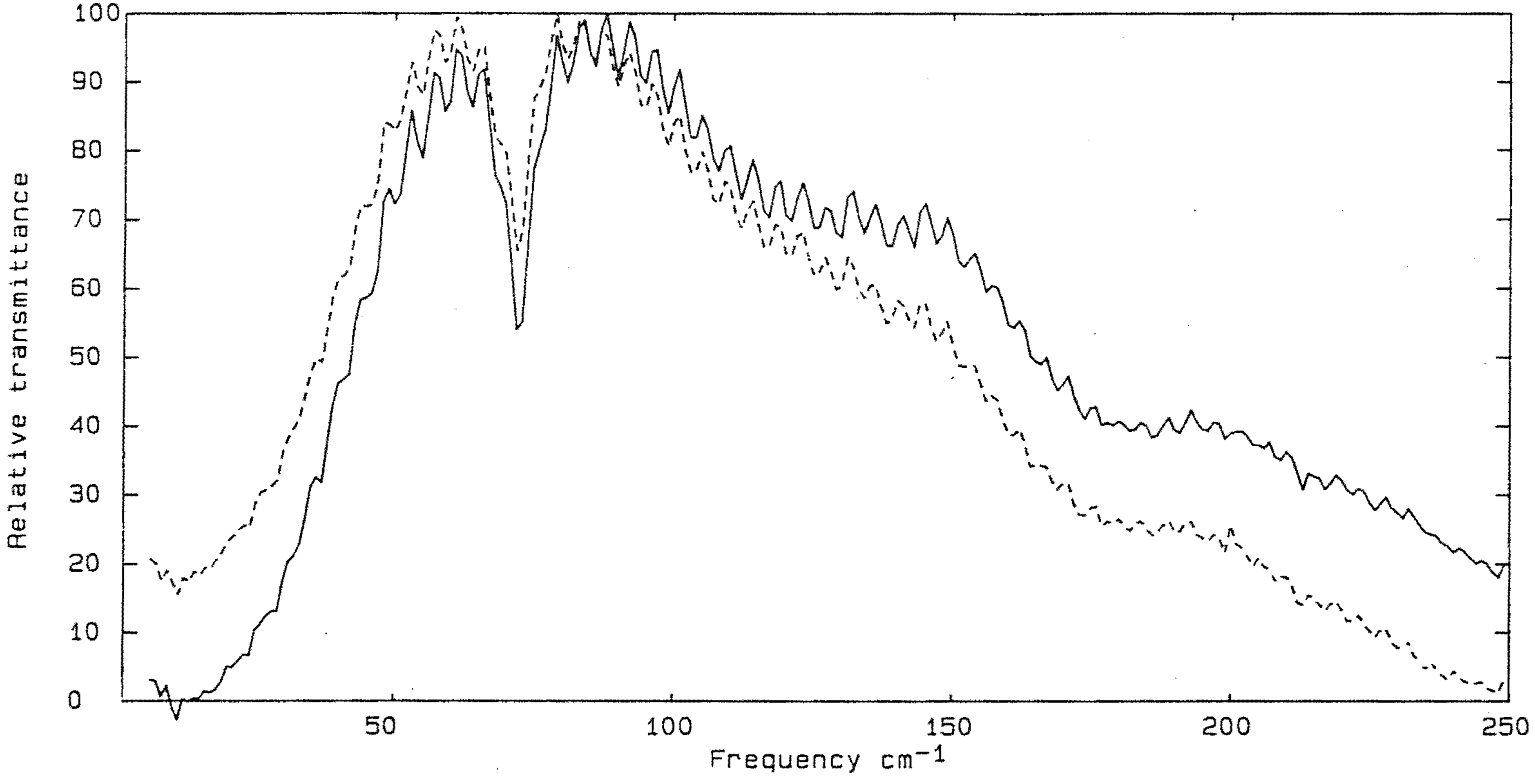

Figure 2.3 Calculated spectra showing the effect of a zero error.

———— zero error taken into account ($e/\Delta = -0.43$)

-------- zero error ignored

first point belongs to both sides (+ve and -ve path difference) of the interferogram for the case of no zero error. When there is a zero error, the value of the first point is multiplied by $0.5+0.5*e/\Delta$ which means that the first point is halved for no zero error, is zero for a fractional zero error of -0.5 and unchanged for a fractional zero error of 0.5. The fractional zero error (e/Δ) cannot be above 0.5 or below -0.5. Figure 2.4 shows how different methods of treating the maximum point give different results. The main difference seems to be in the "height" of the 'zero intensity' line.

Figure 2.5 illustrates the difference between spectra calculated from the same interferogram using the methods of Watts (Mertz 1965) and Forman et al (1966) on a mainframe computer and using the algorithm above for the real time analysis on the PET microcomputer. The spectra are substantially the same.

To check the calibration of the interferometer and the accuracy of the algorithm used, a water vapour spectrum was compared to the results of Hall and Dowling (1967). Figure 2.6 and table 2.1 show that the algorithm used gives results consistent with this reference.

2.1.3 Monitoring the Bolometer

During the cool down of the bolometer the computer is used to monitor the temperature of various parts of the bolometer and the level of the liquid helium. One kilo-ohm Allen-Bradley resistors were used as the temperature sensors. A constant current was passed through them using a 7 Volt power supply and large load resistor in series. The resultant

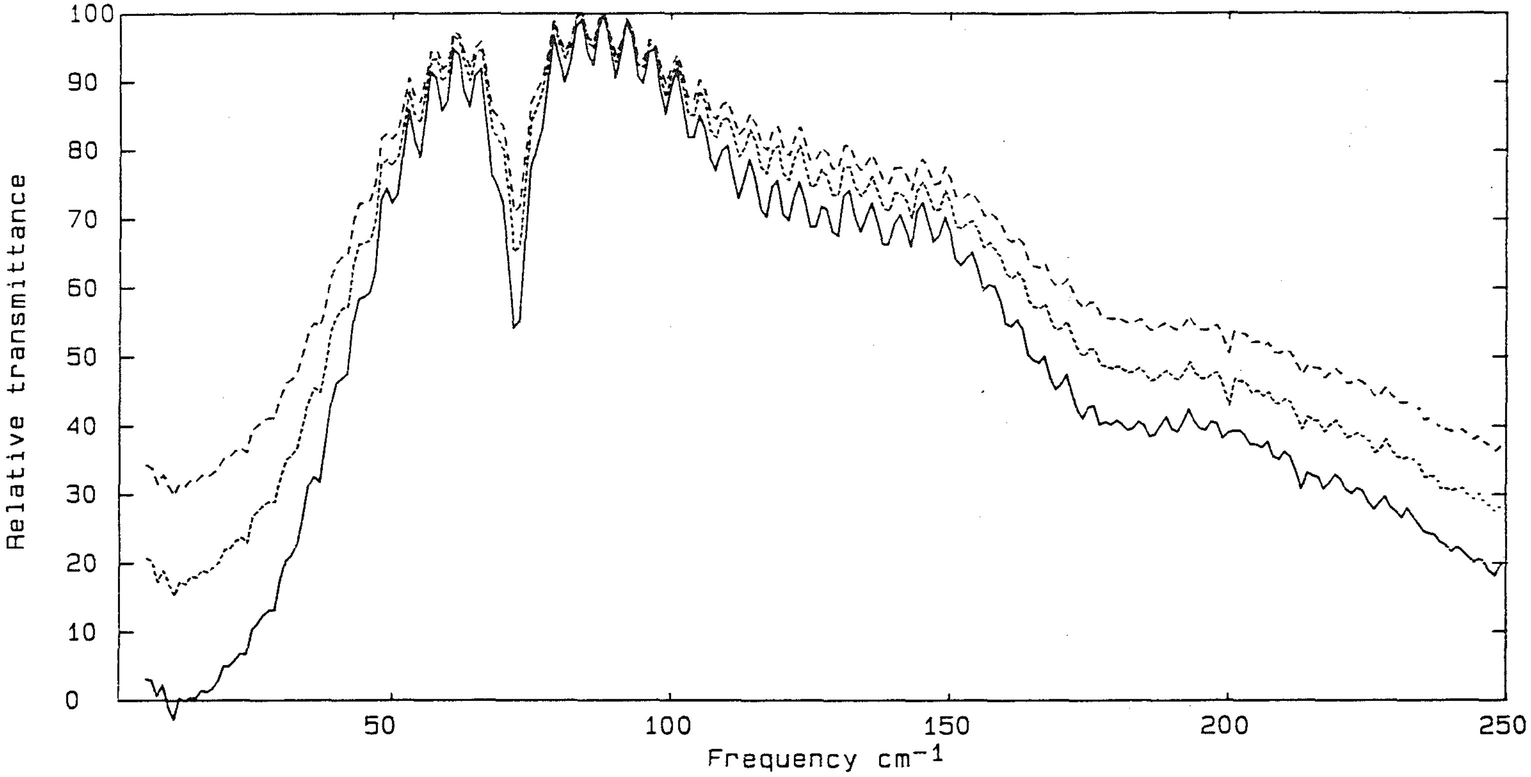

Figure 2.4 The effect of treating the maximum value I(0) of the interferogram in different ways.

——— I(0) multiplied by 0.5 + fractional zero error (e/Δ)

– – – – I(0) multiplied by 1

- - - - - I(0) multiplied by 0.5

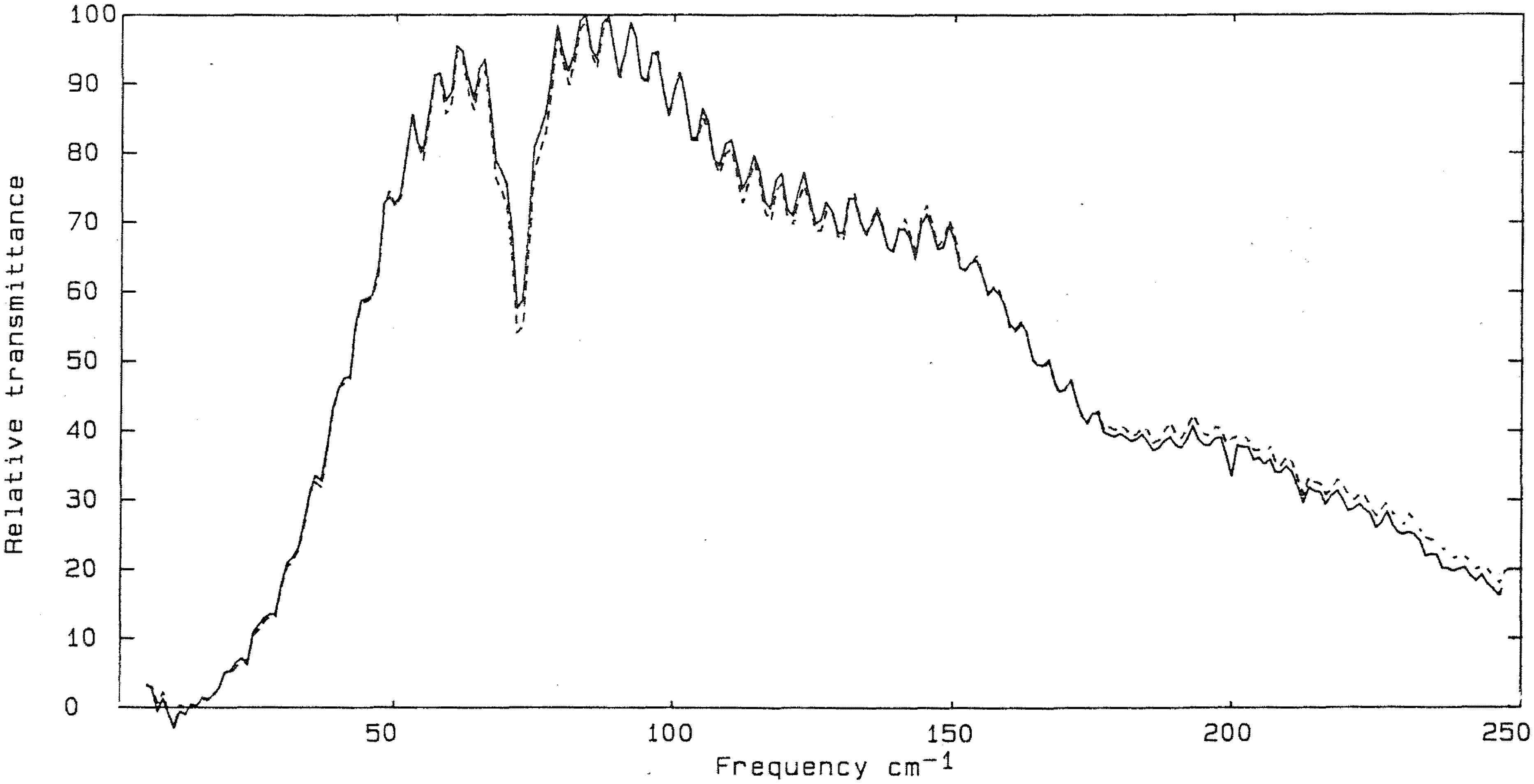

Figure 2.5 Spectra calculated from the same interferogram using two different systems.

——— Watts method using the mainframe computer

----- Real time transform using the PET microcomputer

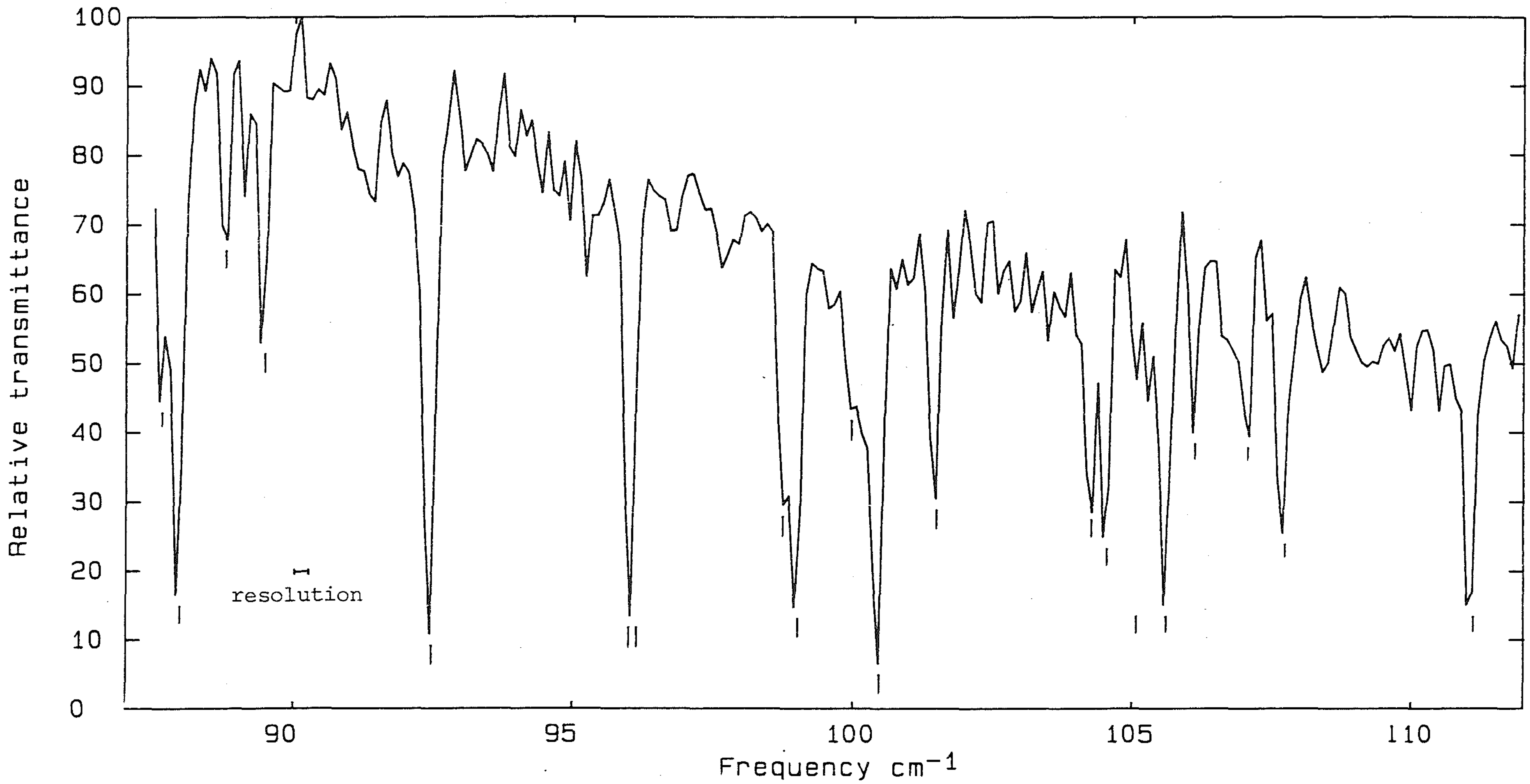

Figure 2.6 Calibrating the interferometer by measuring the spectrum of water vapour. The markers show the line positions of the values quoted by Hall and Dowling (1967).

Hall and Dowling (cm^{-1})	This work (cm^{-1})
87.759	87.7
88.077	88.0
88.877	88.9
89.581	89.5
92.515	92.5
96.067	96.1
96.212	---
98.800	98.8
99.066	99.0
100.021	100.0
100.521	100.5
101.523	101.5
104.288	104.3
104.570	104.5
105.113 $	***
105.639	105.6
106.139	106.1
107.075	107.1
107.738	107.7
111.120	111.0

TABLE 2.1 Comparison of water vapour line positions.

For this work the resolution is 0.25cm^{-1}.

--- not resolved

*** not found

$ only seen in one spectrum

potential drop across each Allen-Bradley resistor was read by the computer via the analog-to-digital converter. The load resistance which kept the current constant had to be increased from 170 Kilo-ohms to 610 Kilo-ohms as the temperature dropped. Two calibration scales were used corresponding to this change in load resistor. The first was for the room temperature to liquid helium temperature range, and the second for the pumped helium temperature range.

The liquid helium level was monitored in a similar manner using a strip of "superconducting" wire running the length of the helium Dewar. The wire was 0.5mm in diameter and had a resistance of 2.5 ohms at liquid nitrogen temperature. The wire consisted of 61 filaments of 34 micrometre diameter Niobium/Titanium (53.5% Nb, 46.5% Ti) superconducting wire imbedded in a cupronickel matrix (75% Cu, 25% Ni). This many stranded wire was chosen because of its mechanical strength and durablility. To ensure that the wire did not become superconducting above the liquid helium level a current of at least one amp needed to be put through the wire. The level detector worked well when the helium was superfluid but did not work so well when there was rapid boil off of helium such as when first pumping on the helium vapour.

The computer had only one A-D converter and so this was manually switched between the various thermometers and the superconducting wire. The last readings of each of the above were displayed simultaneously in an easily read form on the computer screen (figure 2.7).

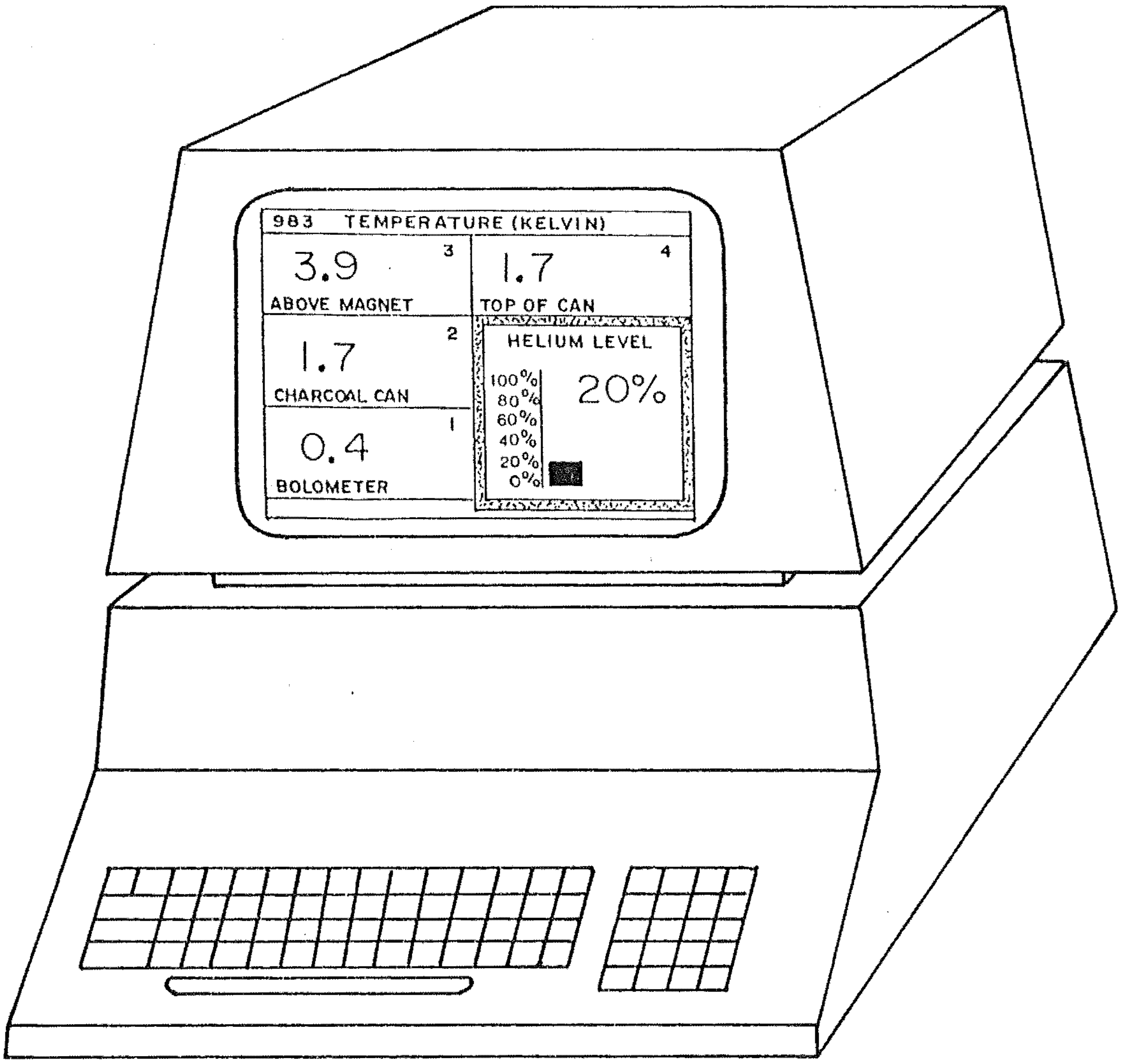

Figure 2.7 The display on the computer screen when monitoring the liquid helium level and the various temperatures associated with the He^3 bolometer. Only one can be recorded at a time. The number in the top right hand corner of the appropriate box flashes to show which is being monitored.

2.2 THE DETECTION SYSTEM

2.2.1 The Detector Element

The sensitivity of a bolometer is measured by it's responsivity (S), the change in the output potential drop across the element divided by the radiation power absorbed by the element. Standard bolometer theory (Zwerdling et al 1968) gives.

$$S(f) = \frac{S(0)}{[(1+(2\pi f\tau)^2]^{1/2}}$$

where τ is the response time given by $\tau = \frac{C}{(G_D - I^2 R\alpha)}$

$$\text{and} \quad S(0) = \frac{IR\alpha}{(G_d - I^2 R\alpha)}$$

where f is the frequency with which the radiation is chopped

R is the resistance of the element at the operating temperature

α is the temperature coefficient of resistance for the element material

C is the thermal capacity of the element

G_d is the dynamic thermal conductance between the element and the 0.4 Kelvin block

given by $G_d = \frac{d(I^2R)}{dT}$

I is the current through the element

T is the temperature of the element.

The element, cut from a single crystal of Germanium double doped with Antimony and Indium, used in these bolometers was given to Dr J. A. Campbell by Professor A. J.

Sievers of Cornell University. It was from the same boule he has used in all of his He^3 bolometers.

The signal-to-noise ratio of the bolometer is best when the element's resistance is large, its mass is small and the temperature is low.

The resistance is maximized by making the element as long and thin as possible (6mm*1mm*1mm) giving a resistance of 1.2 megohm at a temperature of 0.4 Kelvin. The temperature of the element was determined by measuring the element's resistance as a function of helium gas pressure above the liquid helium bath in which the element was immersed. A function of the form $R=R_\infty * e^{(a/\sqrt{T})}$ (Draine and Sievers 1976) is then used to fit the data (figure 2.8) giving R_∞ = 30 ohms and a= 6.7 $K^{1/2}$. Draine and Sievers (1976) found this equation to be valid to 0.1 Kelvin so the fitted equation can be extrapolated to measure the temperature of the element below pumped helium temperatures.

Making the element's cross-section smaller also decreases the element's mass which decreases its thermal capacitance enabling the element to respond faster to radiation changes and so increases its response for a given frequency. In Figure 2.9 the signal is plotted as a function of chopping frequency. Fitting the responsivity equation above to the data gives a response time of 1.6 milliseconds.

If the element's thickness is decreased below 1mm the element becomes too fragile and is easily broken. This thickness is sufficient to absorb radiation well when the

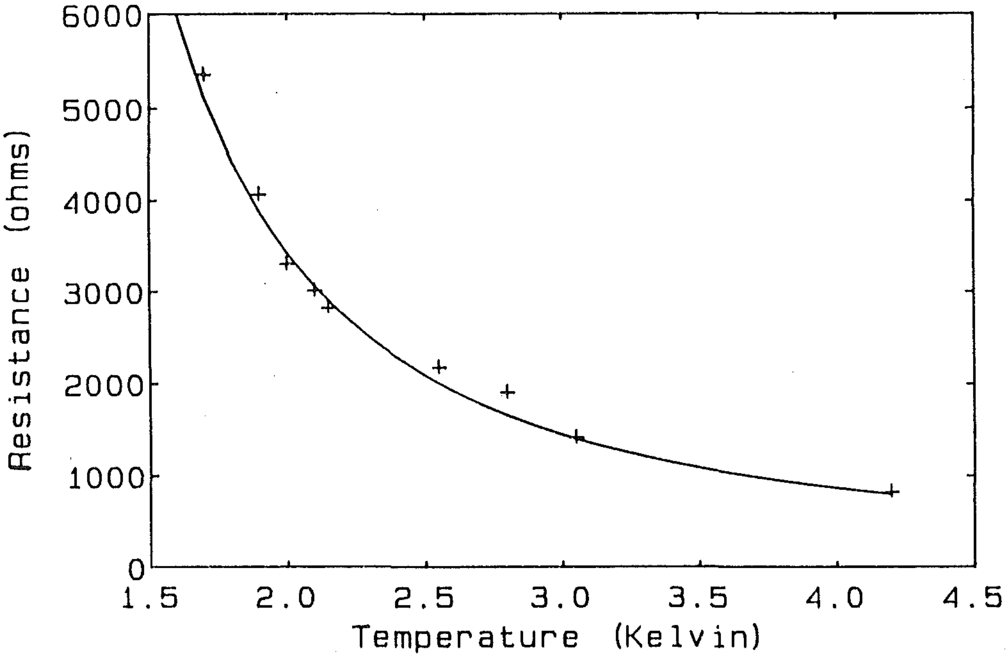

Figure 2.8 Resistance of the bolometer element as a function of temperature. The expression $R=R_{\infty}e^{a/\sqrt{T}}$ is fitted to the data yielding the parameters $R_{\infty} = 30$ohms, $a = 6.7\ K^{\frac{1}{2}}$.

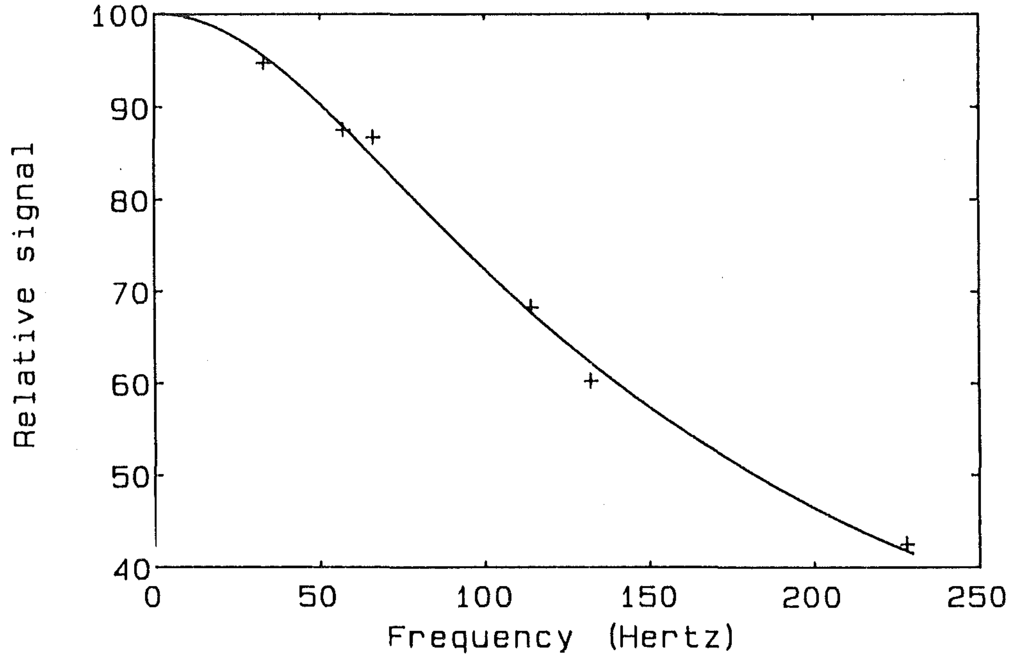

Figure 2.9 Frequency response of the bolometer element and associated electronics. The expression $[1+(2\pi\tau f)^2]^{-\frac{1}{2}}$ is fitted to the data yielding a response time τ of 1.6ms.

element is placed in a integrating spherical cavity (figure 2.10).

The element was attached to a cooled copper block by a pair of varnished copper wires of diameter 0.9mm and length 16mm. One of the wires was soldered to the copper block. The other wire is clamped to the block in order to give a thermal contact while at the same time electrically isolating this wire from the block. The wires were soldered onto the element using Indium solder and a ten Watt soldering iron whose heat output had been decreased by plugging into a variac at 180 Volts.

At first glance at the responsivity equation above,it may seem that decreasing the thermal conductivity of the wires, by reducing their thickness, would give a better response. However this would also mean that the element would be at a higher temperature for a fixed heat input.

The signal-to-noise ratio of the bolometer (typically 2 millivolt maximum signal to 0.7 micro-volts rms noise) was comparable to the bolometers at Cornell University (Dr J. A Campbell Private communication, Drew and Sievers 1969). For this reason and the scarcity of liquid helium the responsivity of the bolometer element was not determined accurately. For the element above, the signal is at a maximum when the current through the element is 0.5 microamps. This is a trade off between a greater current giving more Joule heating of the element and consequent decreased signal, and the greater current giving increased voltage change (i.e. increased signal). The maximum signal-to-noise ratio is at

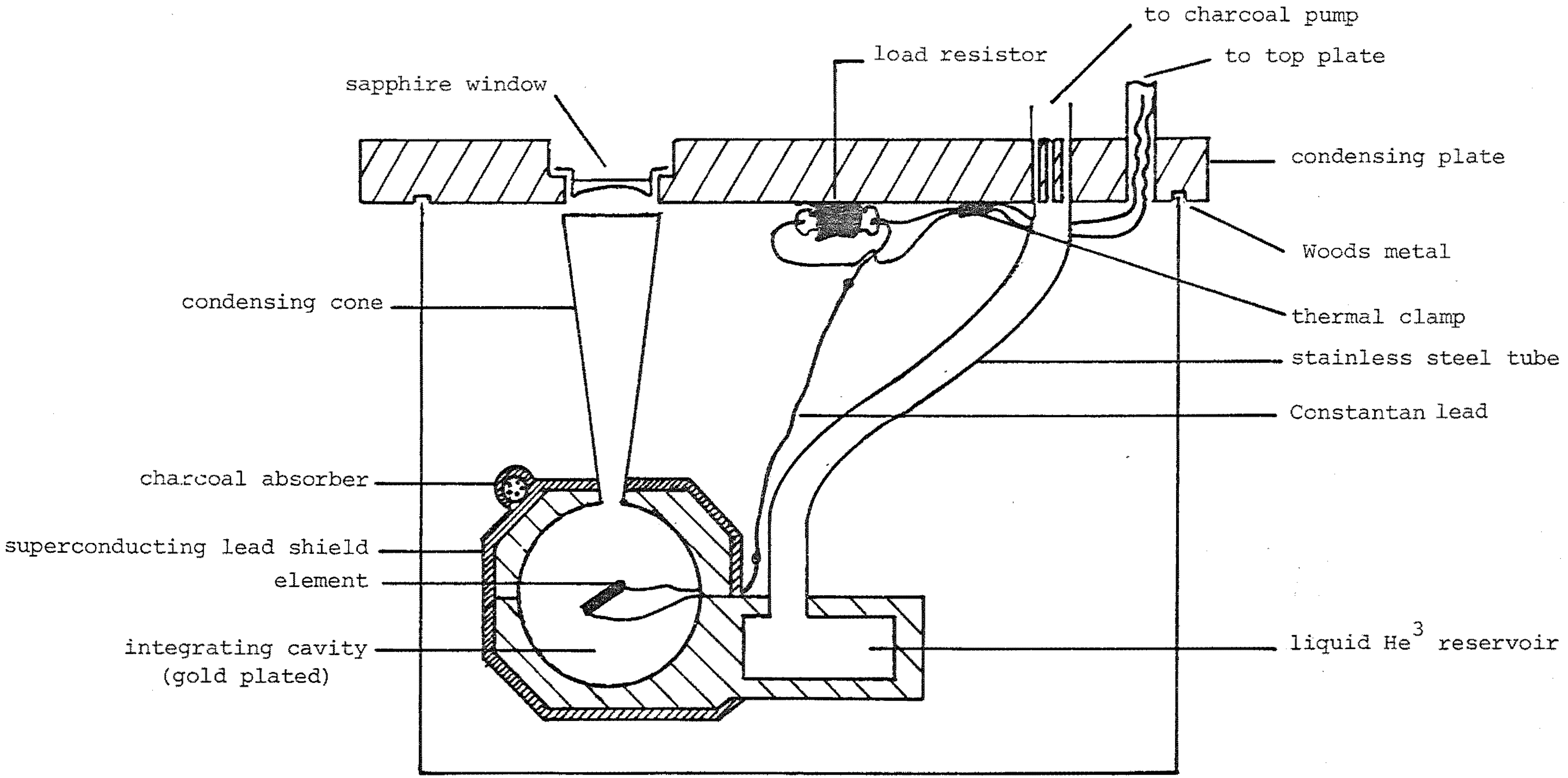

Figure 2.10 The detector chamber for the large bolometer.

about 100HZ chopping frequency which is a compromise between more signal at lower frequencies and less "1/f" noise at higher frequencies.

2.2.2 Signal Amplification

A constant current is applied to the bolometer element by a high stability, wire wound, ten megohm load resistor and a small 9 Volt no. 216 Eveready battery. Neither cooling the resistor to 1.7 Kelvin nor using a larger 9 Volt battery appreciably decreased the noise of the bolometer.

The radiation intensity is varied using a mechanical chopper. The resulting a.c. voltage drop across the element was amplified by a Princeton Applied Research Model 186A lock-in amplifier. The reference signal is generated by an infrared emitting diode / phototransistor pair positioned on either side of the chopper blades.

The chopper blades are turned by a tape recorder motor whose frequency can be varied continuously between 33 and 57 Hertz. The motor has no bearings so the metal shaft must be lubricated with Edwards 704 silicon oil approximately every 20 hours of running. In order to cover a greater frequency range several aluminium blades with different numbers of apertures were available. Normally a two aperture blade was used giving a chopping frequency of 114 Hertz. Care was taken to avoid any multiple of the 50 Hertz mains frequency.

2.2.3 The Helium 3 Refrigerator

A self contained activated charcoal pump, immersed in pumped liquid helium, following the design of Sievers and his co-workers (Walton et al. (1971).) forms the basis of the He^3 cooled bolometer constructed and used in this work.

The pump makes use of the ability of activated charcoal to adsorb He^3 once the charcoal is cooled to below about 40 Kelvin. The charcoal chamber is therefore initially isolated from the helium bath by a vacuum space until the He^3 gas has condensed. Then helium gas is let into the vacuum space. The charcoal cools to the bath temperature (1.7 K) and adsorbs He^3 gas. The resultant lowering of vapour pressure above the condensed He^3 cools the element block to 0.4 Kelvin.

Two bolometers were used; a smaller bolometer constructed prior to this work and a larger bolometer which needed to be designed and built for the superconducting magnet system.

The smaller bolometer had a slight problem with its refrigerator that prolonged the cooldown by up to two hours. The bolometer element would warm suddenly and then cool again. This was attributed to most of the charcoal not being in good thermal contact with the bath (Vickers 1981). Thermal contact with the warmer, inner charcoal granules was via the He^3 gas and also via the surrounding charcoal granules, each of which had only a small area of contact with its neighbours. Initially the He^3 gas in the can was at the same temperature as the charcoal (90K). When the can was cooled to

1.7K, by admitting helium gas to the vacuum space surrounding the can, the outer granules cooled to 1.7K and adsorbed the He^3 gas in the can. This thermally isolated the inner granules. The colder replacement He^3 gas coming from the tube to the liquid He^3 reservoir was thus initially heated by the inner charcoal granules. It expanded and sent a heat pulse to the detector block through the He^3 gas. Large changes of pumping speed and temperature were thus produced.

The problem was cured by ensuring that all the activated charcoal granules were in better thermal contact with the outer wall of the charcoal container. A perforated brass sleeve was inserted into the charcoal pump (figure 2.11) so as to confine the charcoal granules to a narrow space next to the container wall. The volume of charcoal granules used was also thereby reduced from 100ml to 10ml. This arrangement enabled all the charcoal to cool uniformly and quickly to 1.7 Kelvin and so adsorb He^3 steadily without sudden variations in pumping speed for up to 12 hours of operation.

The small bolometer occasionally exhibited a puzzling periodic oscillation in signal of period 3 seconds and amplitude 0.05 millivolts (figure 2.12). The oscillation ceased only when the helium bath was disturbed. This could be achieved by suddenly increasing the pressure above the helium bath or knocking the Dewar. This did not always solve the problem and the oscillations would eventually reappear.

The only tentative explanation for the phenomenon is that the oscillation is due to thermal oscillations within

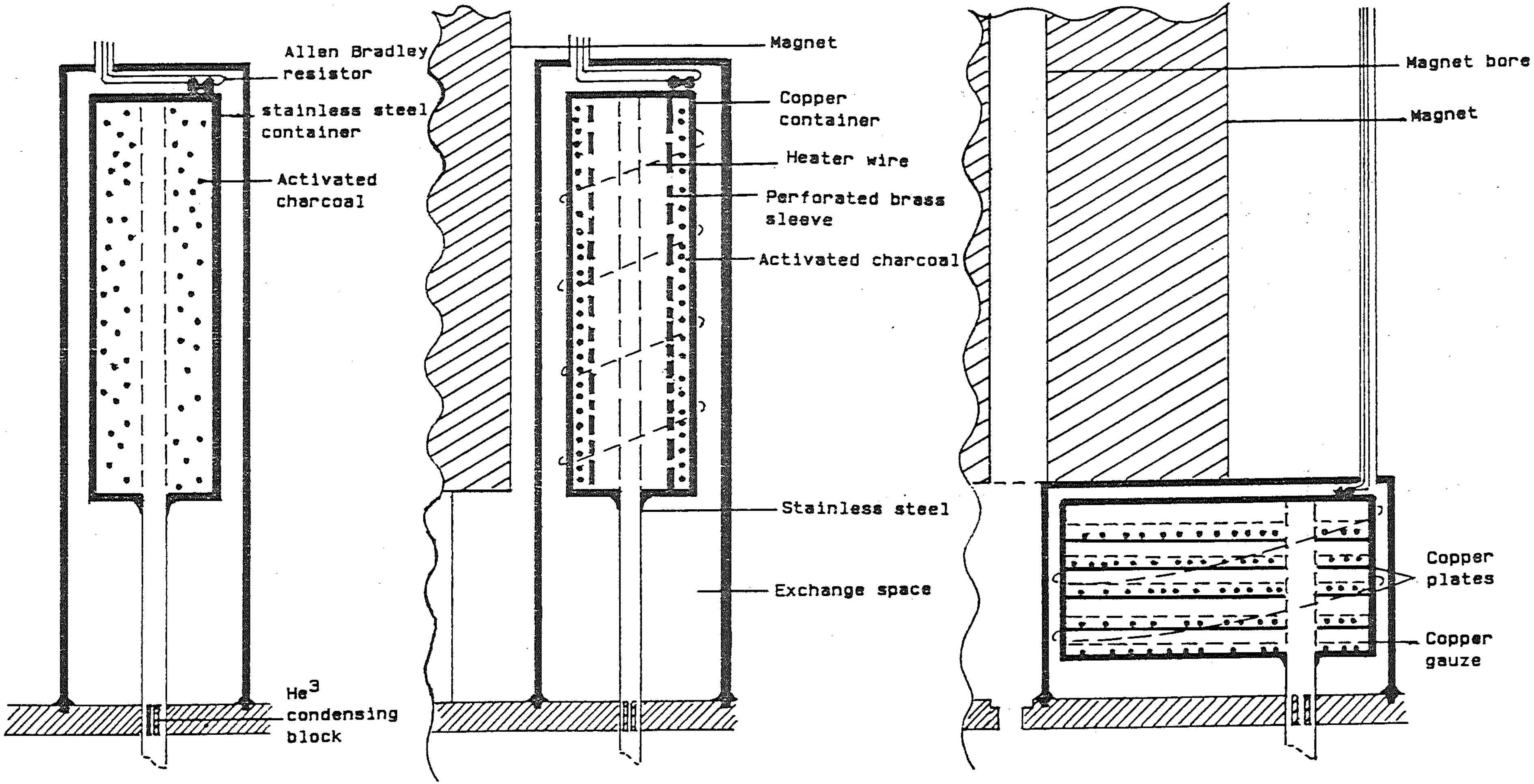

(a) Old design (b) Present design (c) Proposed design

Figure 2.11 Comparison of charcoal pump designs.

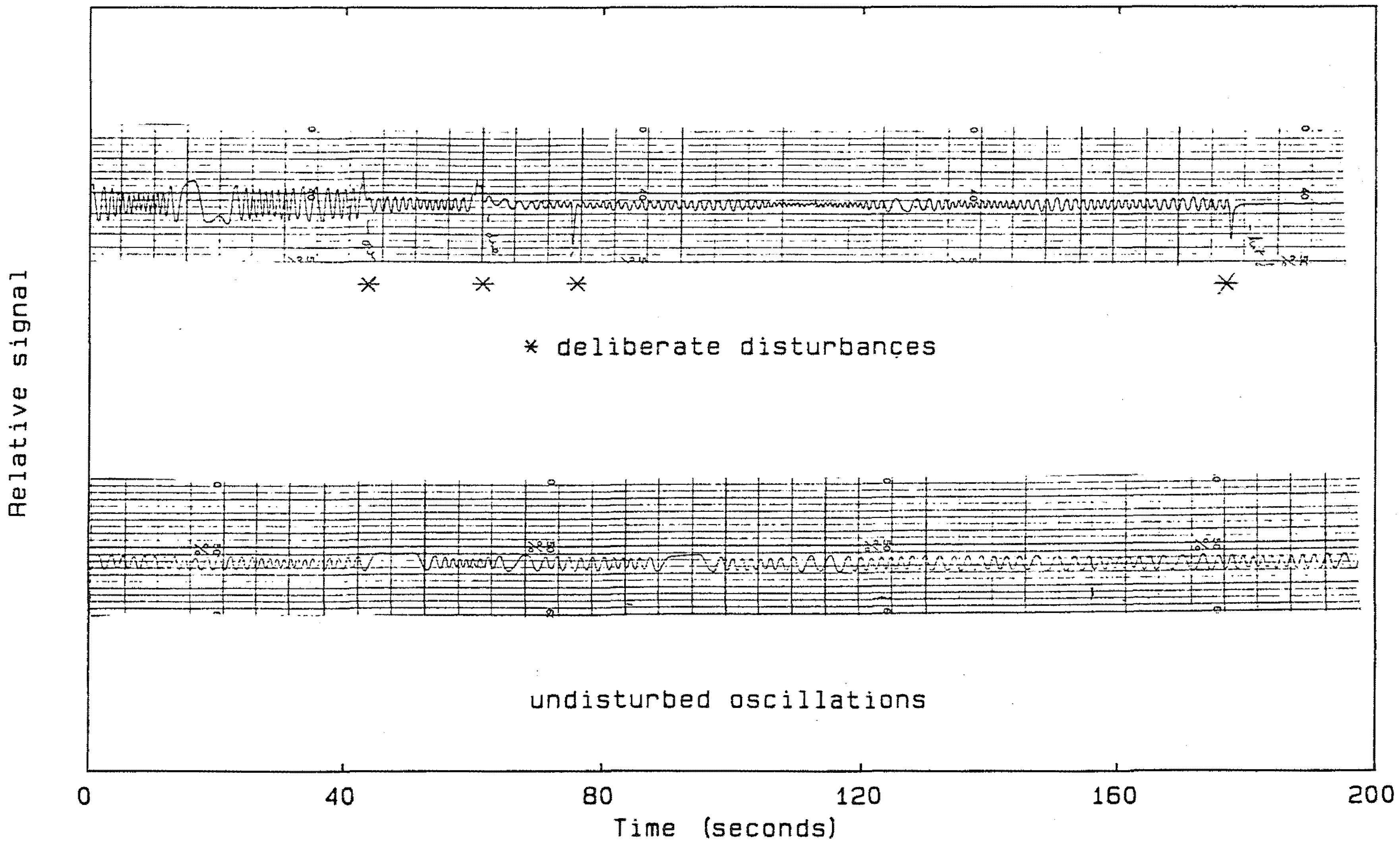

Figure 2.12 Periodic oscillations in signal observed for the small bolometer.

the He^3 pump. This oscillation can then be disturbed by fluctuations in the helium bath temperature. The bath temperature remained constant throughout the oscillations so the oscillations did not have their origin in the helium bath. This problem would ruin about one spectral run in ten. Further investigations would be needed to find the origin of this problem and so solve it.

The charcoal pump for the new He^3 bolometer/magnet system was of the same basic design as the modified version for the small bolometer except that the charcoal can was made of copper (rather than the stainless steel of the original) in order to assist the cooling of the charcoal when the can is thermally connected to the bath.

At room temperature the charcoal pump was filled with He^3 gas at a pressure of 9.5 atmospheres which has decreased to 8.4 atmospheres pressure after two years. This refrigerator will remain operational for typically 12 hours. Occasionally longer runs were needed. For these occasions a heater wire (43cm of 0.2 ohms per cm. nicrome wire) was wrapped around the charcoal can and attached using GE7031 low temperature varnish. Provided only a small amount of exchange gas had been admitted into the the space around the charcoal can during the initial cool down, then 10 Volts across the heater terminals was sufficient to heat the charcoal above 40 Kelvin and so expel the He^3 gas and recondense it in the detector block. The temperature of the element is monitored during this procedure and the heater is kept on until the element temperature starts to rise. On one occasion the bolometer was kept operational for 26 hours using this technique.

For the new larger bolometer, the He^3 refrigerator tube between the condensing plate and the detector block was curved to allow for the large separation between the refrigerator axis and the magnet axis (figure 2.10). There was no noticeable flexing of this tube when the He^3 chamber was initially pressurised so Bourdon tube flexing was not expected to be a problem when the refrigerator cooled to 0.4 Kelvin. The periodic oscillations in signal that occurred for the small bolometer did not occur in the new one. Perhaps the curved tube prevented them? Also in the new bolometer sufficient volume was allowed inside the detector block to condense all the He^3 gas present. This was not the case in the small bolometer where the liquid He^3 extended up the stainless steel connecting tube.

2.2.4 A suggested design for a future charcoal pump

The radiation throughput for the magnet system could be markedly improved by eliminating the need for the six 90 degree reflections used in order to have the radiation electric vector parallel to the magnetic field of the magnet (see figure 2.18). This could be done by using a magnet with a transverse access. To maximize running time the sample and magnet need to be as low as possible in the Dewar.

In the present bolometer the magnet is alongside the charcoal pump. If the charcoal pump were shortened to be less than 5 cm high then the magnet could be above the charcoal pump. This would enable the light pipe to be centrally located within the Dewar and the magnet could then take up the full width of the Dewar, increasing the space available to the magnet from a 9cm diameter cylinder to a 14cm diameter cylinder. A suggested design for the shortened charcoal pump is shown in figure 2.11c. The main difference is that the charcoal is stacked in thin layers on copper platforms rather than confined to the sides of the container.

2.2.5 Superconducting magnet

For the far infrared Zeeman experiments a British Oxygen model FLM4, 5 Tesla superconducting magnet was purchased. It had a clear bore of 2.5cm and was fitted with a superconducting switch and a magneto-resistance field measurer. Details of the magnet are given in figure 2.13 and the axial field as a function of distance along the axis in figure 2.14.

Care was needed in choosing the high current leads to the magnet. If the wire diameter is too small the Joule heating of the wire noticeably heats the bath liquid and the magnet terminals. For high currents the later was found to drive the magnet normal. If the wire diameter is too large then the helium boil-off rate is increased, and the available running time of the magnet thereby decreased, by the heat in-flow conducted along the wires. As a compromise, copper tubing 10cm long and 1cm diameter was bolted to the magnet terminals. Two 1mm diameter copper leads were soldered into the copper tube. Half way up the Dewar each lead was soldered to two 1.3mm diameter copper wires which were increased to 2.1mm diameter at the room temperature terminal. The leads

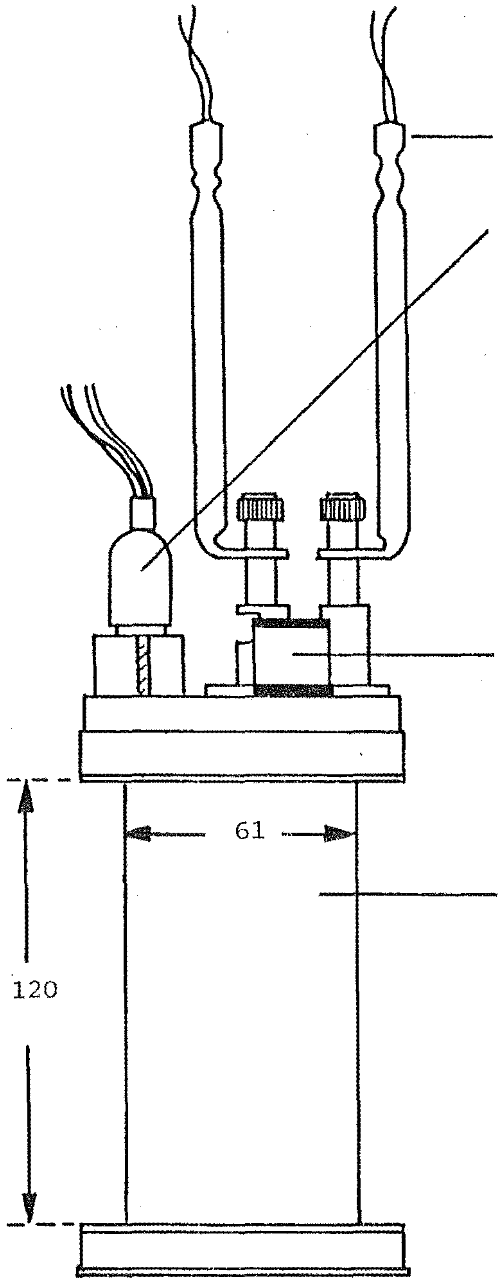

Current leads

Magneto-resistance probe leads
operating current 5 mA

Tesla	mV
0	25.66
1	28.21
2	32.95
3	38.75
4	44.925

Superconducting switch

heater resistance	100 Ω
operating current	200 mA

Superconducting magnet

maximum field	5 Tesla
maximum current	56.43 amp
calibration	0.0886 T/amp

maximum sweep rate

6	amp/min	to	30 amp
3	"	"	40 amp
1.2	"	"	50 amp
0.6	"	"	max

Clear bore	25 mm
Winding 1D	28.6 mm

FIGURE 2.13 Manufacturer's data for the superconducting magnet

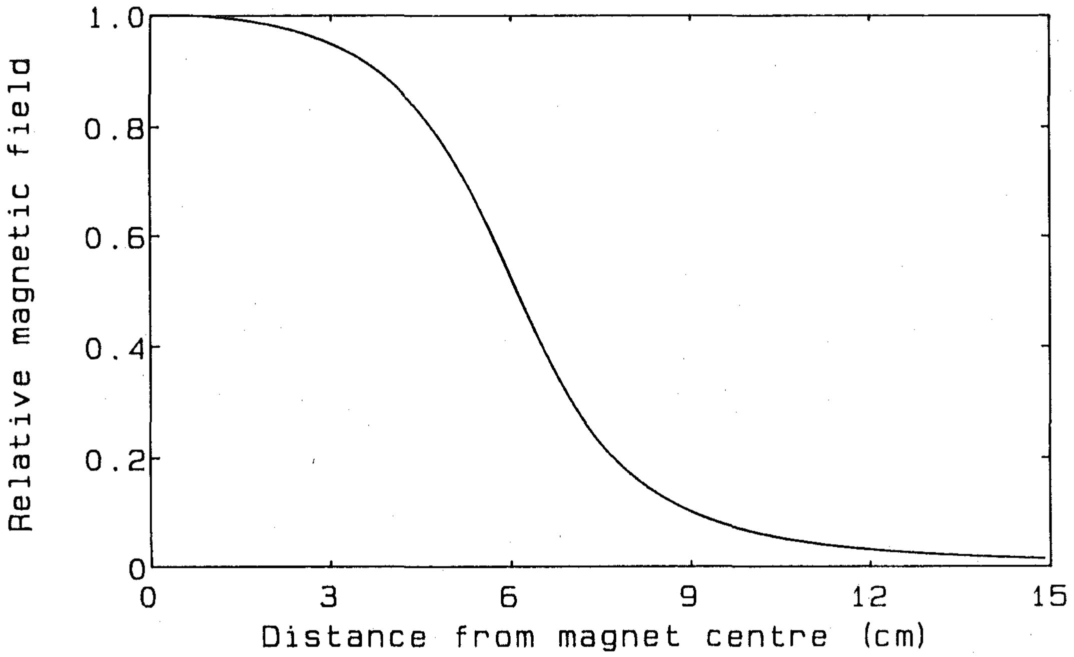

$$\frac{B_Z}{B_O} = \frac{1}{0.5F(\alpha,\beta)}\left\{(\beta-x)\ln\frac{\alpha+\sqrt{\beta^2+(\beta-x)^2}}{1+\sqrt{1+(\beta-x)^2}} + (\beta+x)\ln\frac{\alpha+\sqrt{\beta^2+(\beta+x)^2}}{1+\sqrt{1+(\beta+x)^2}}\right\}$$

where $F(\alpha,\beta) = \beta\ln\dfrac{\alpha+\sqrt{\alpha^2+\beta^2}}{1+\sqrt{1+\beta^2}}$

$$\alpha = \frac{d_2}{d_1}$$

$$\beta = \frac{\ell}{d_1}$$

$$x = \frac{2Z}{d_1}$$

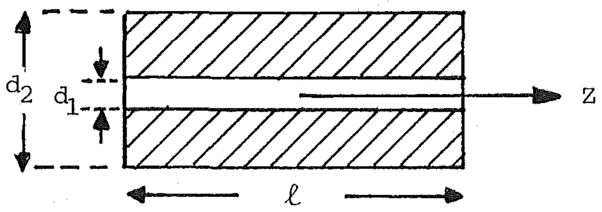

Figure 2.14 Axial variation of magnetic field for the 5 Tesla magnet (following Campbell 1968).

were spiralled down the bolometer supports to increase the length of the conduction path.

2.2.6 The Dewar system

To accommodate the superconducting magnet, a large Dewar system was designed and built. The liquid helium Dewar needed to be long as the liquid helium bath was to be pumped to reduce its temperature to 1.7 Kelvin. As a general rule of thumb for glass Dewars, approximately half the initial charge of liquid helium at 4.2 Kelvin is evaporated in cooling the apparatus and the rest of the liquid helium to 1.7K. The width of the Dewar needed to be such that the magnet would fit alongside the charcoal pump. The liquid helium cryostat was therefore made of pyrex with an inner diameter of 15cm,an outer diameter of 22cm and an overall length of 104cm. This was as large as the university glass blower could make. As a consequence the outer liquid nitrogen cryostat had to be constructed in stainless steel in the physics department workshop. It has inner diameter 30cm, outer diameter 38cm, length 95cm and has superinsulation in the vacuum wall. The Dewar system is shown in figure 2.15.

The top of the pyrex Dewar was formed from a 190cm Q fitting, using standard couplings to join it to the metal top plate of the cryostat system. The top plate has supports resting on the lip of the stainless steel cryostat. A phosphor bronze spring supports the base of the pyrex Dewar to allow for the difference in thermal contraction between pyrex and stainless steel as they are cooled.

The helium boil off is minimized by silvering the

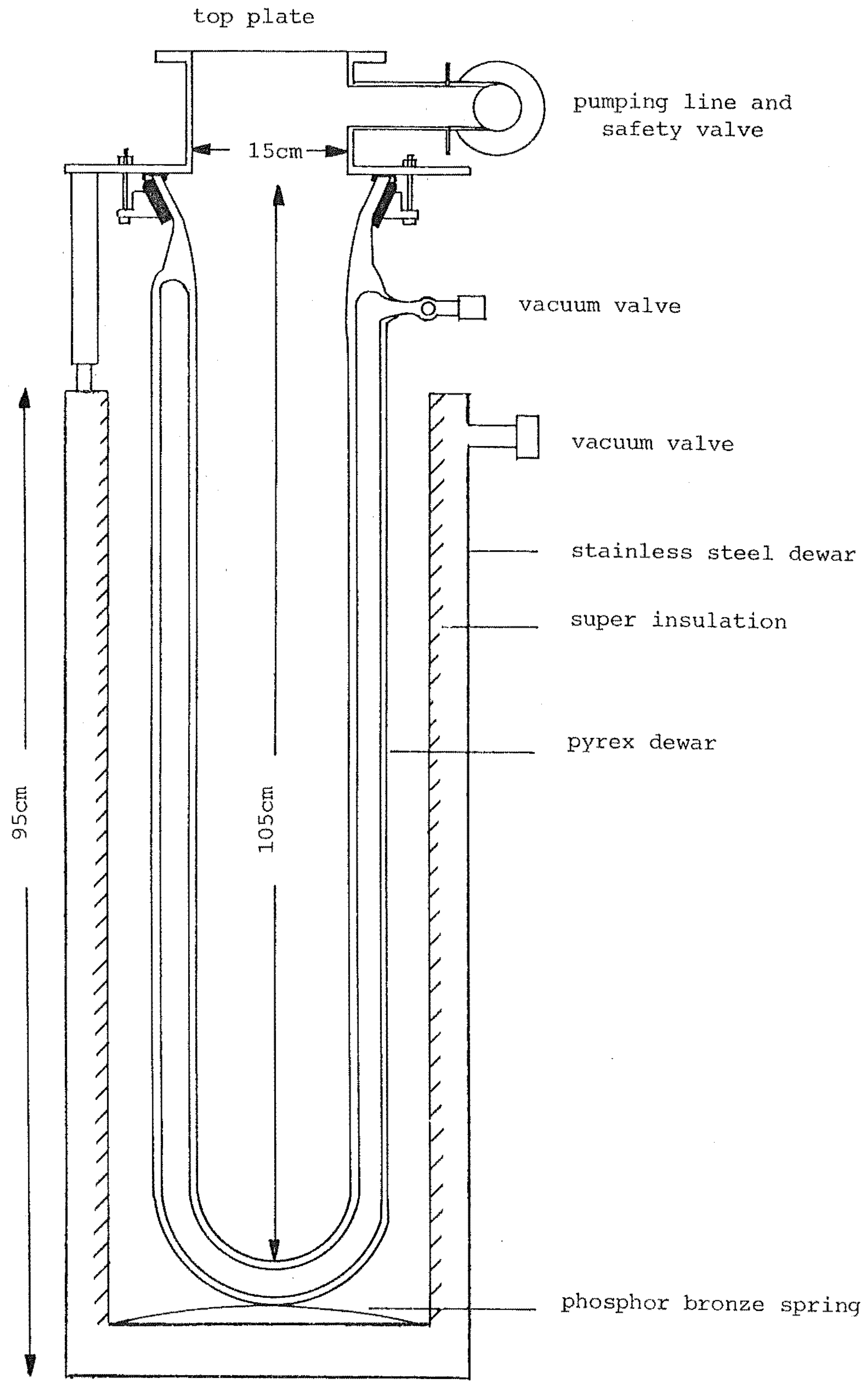

Figure 2.15 Cross-section of the dewar system for the large bolometer.

walls of the vacuum space within the glass Dewar. In the past we have silvered such Dewars ourselves. This one was coated much more cheaply by the Dominion Mirror and Glass Co. Ltd. Aluminium discs were placed in the pyrex Dewar at 15cm and 30cm below the top to make the cooldown more efficient. They prevent cold helium atoms striking first the room temperature top plate. The system has a helium evaporation rate,for a 10 Torr bath vapour pressure, of 0.4 litres per hour.

The liquid helium bath is pumped with a 450 litre/minute single stage rotary pump. To prevent temperature fluctuations in the bath, due to pressure fluctuations caused by the oscillating volume of the rotary pump, a large ballast volume was used. This was in the form of 3.5m of 100mm bore PVC sewer pipe (figure 2.16). The pipe was clamped to a concrete shear wall of the building to reduce the effects of the mechanical vibrations of the pump. Direct vibrations along the pump walls were reduced by inserting in the line thin-walled copper bellows with rubber discs between divisions to prevent collapse of the divisions when the internal pressure of the pipe is low. The connection between Dewar and ballast volume was by 2m of 50mm PVC tube. A 50mm bore stainless steel butterfly valve manufactured by the National Dairy Association for the dairy industry was tested and found to be a perfectly adequate vacuum valve of local manufacture.

Overall, the effective pumping speed of the system at the pyrex Dewar was 300 litres per minute giving a lowest possible vapour pressure of 5 Torr and thereby a lowest

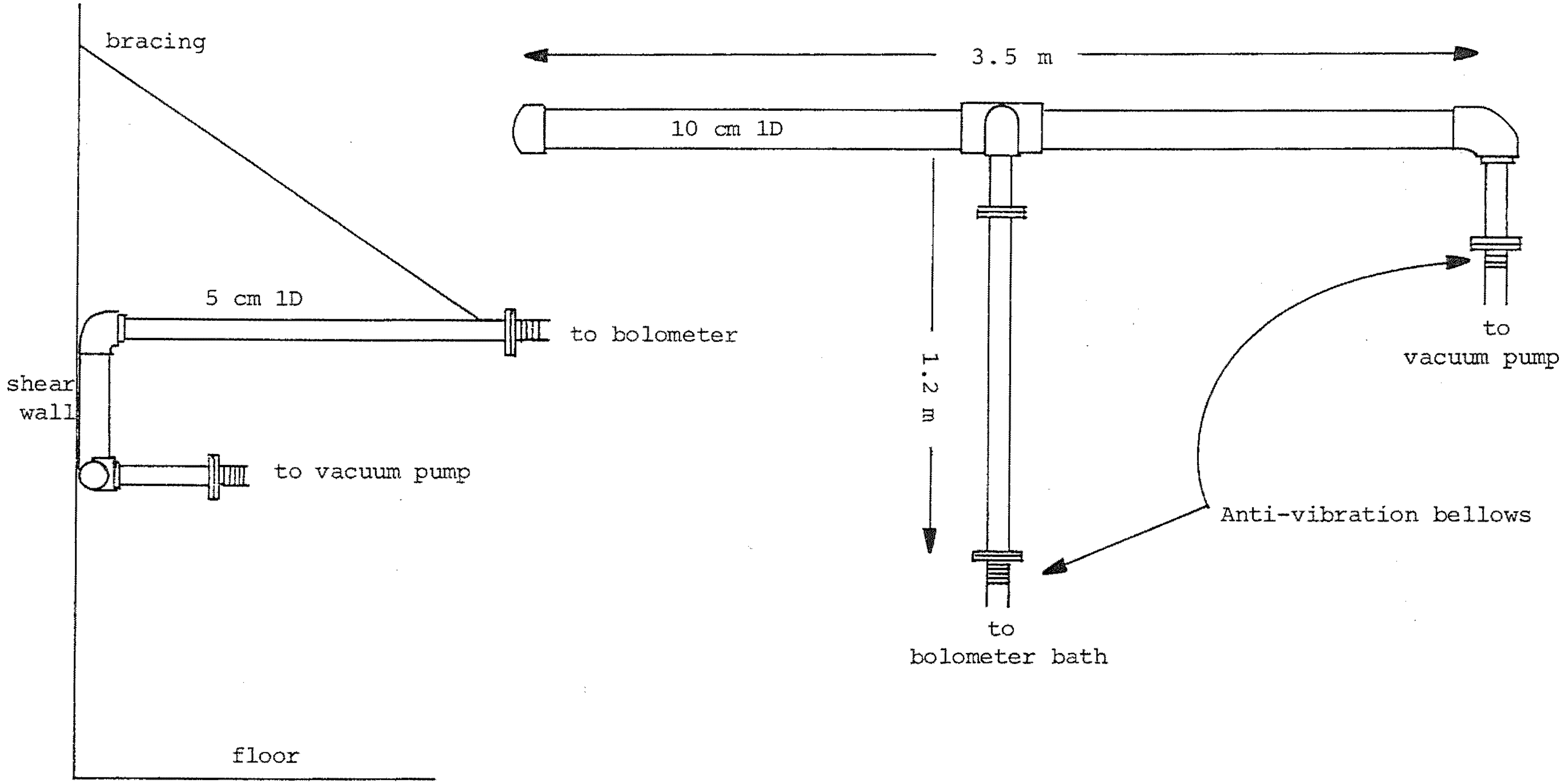

FIGURE 2.16 Details of the ballast volume and pumping line between vacuum pump and bolometer

possible liquid helium temperature of 1.6 Kelvin.

2.2.7 The effect of a magnetic field on the detector

A problem which was not foreseen was the severe, non-reversible decrease in signal due to the effect of the magnetic field on the bolometer element (figure 2.17a). The signal output was unaffected by magnetic fields of up to 0.019 Tesla at the detector element. However as the field increased above this value to 0.037 Tesla the signal output dropped smoothly by a factor of five making the detector effectively unuseable. Above this field there was no further degradation in performance.

This drop in signal persisted when the magnetic field had been reduced to zero although it did recover by about 15 percent. The signal output could only be returned to the initial value by heating the element.

The element resistance changed similarly except it increased by 40% (figure 2.17a). This change was roughly as expected since germanium temperature sensors are well known to exhibit severe magnetoresistance (Sample et al. 1977).

In both these cases there was at least thirty seconds delay between the magnetic field change and the element's response. This was attributed to eddy currents induced in the cooling block or the element. These would heat the latter and therefore lower its resistance. This hypothesis is supported by the decrease in the element's resistance as the field was decreased and the increase in resistance after the field reached zero in figure 2.17a.

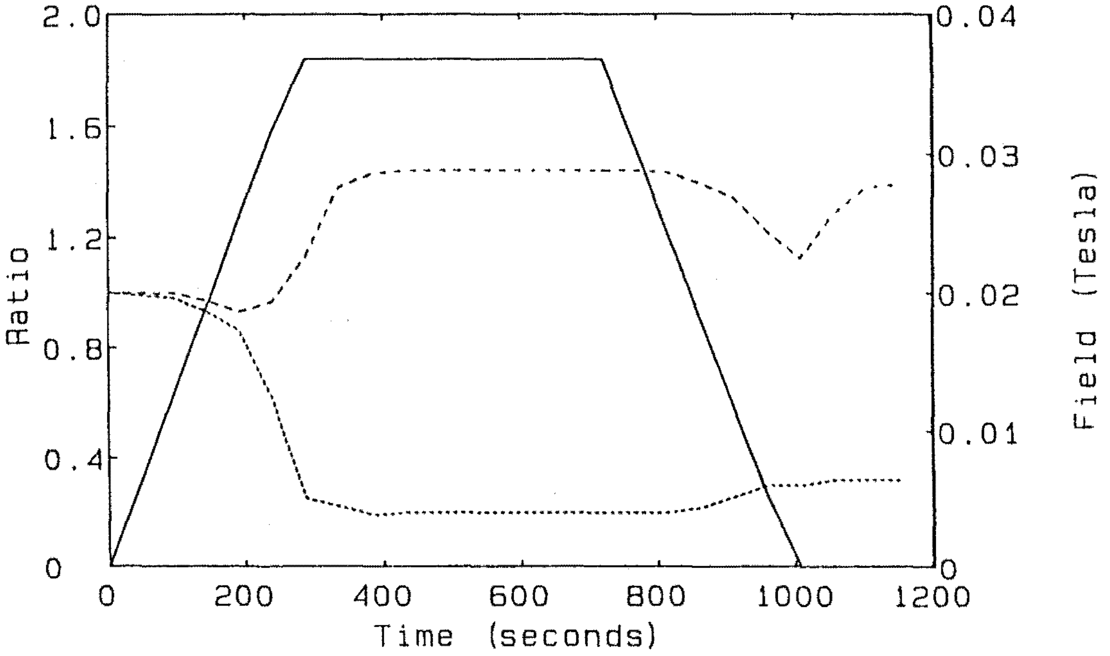

(a) With no superconducting shielding

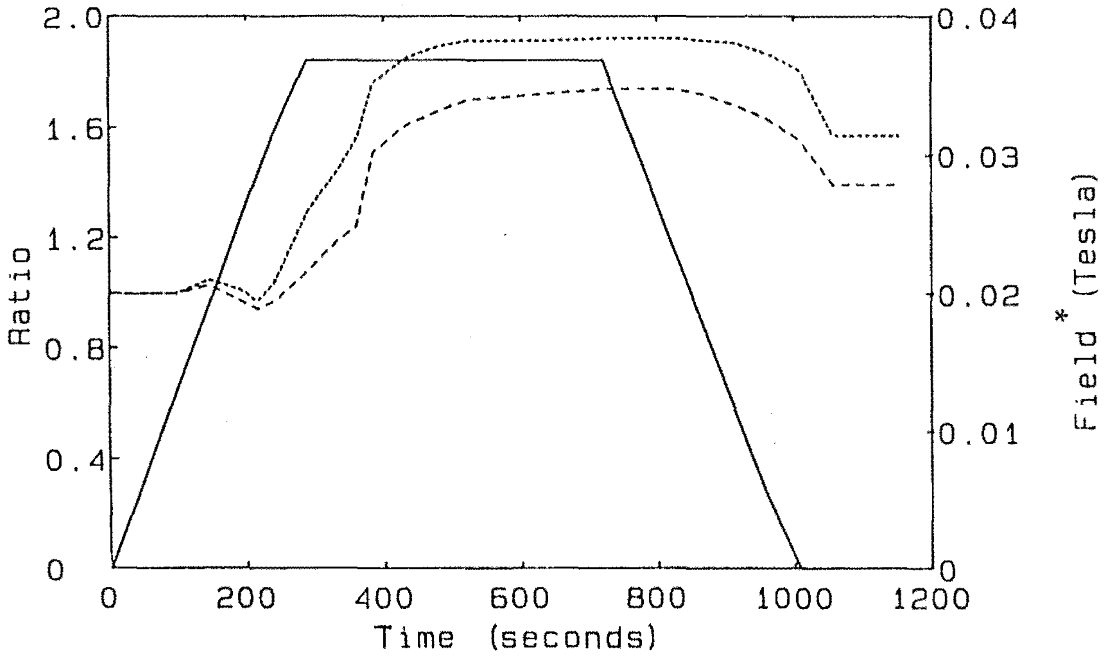

(b) With partial superconducting shielding

Figure 2.17 The effect of a magnetic field on the resistance of the bolometer element and on the output signal. Both are normalized against the initial zero field values. (*This is the field that would have been present at the element had no lead shielding been present.)

—— magnetic field ---- resistance ······ signal

There are several possibilities that would cause the signal output to decrease with a magnetic field present at the element; the element is absorbing less, more radiation is being absorbed other than in the element or the thermal capacity of the element has increased.

One possibility for the effect was suggested by the fact that the critical magnetic field for superconducting indium (0.028 Tesla) falls right in the middle of the magnetic field range over which the signal output changes (0.019 to 0.037 Tesla). The element has a generous lump of indium solder at each end for ease of attaching the electrical leads. The change from superconducting to a normal state will alter the amount of radiation being absorbed by the indium and hence the temperature of the element.

The detector element was then partially magnetically shielded by placing a superconducting lead shield across the top of the element holder. For the magnetic field range used in these tests, the field at the lead sheet did not exceed the critical field for lead. However there was still a weak magnetic field at the detector due to fringing fields around the edge of the superconducting shield.

With this partial shielding the resistance of the element increased with magnetic field slightly more than for the unshielded case (1.8 times compared to 1.4 times). Of more significance, the signal output now followed the resistance change and almost doubled in value (figure 2.17b).

Both element resistance and signal output still had a non-reversible component. This tends to indicate some sort of trapping phenomena as the main problem.

With liquid helium supplies limited no more effort was expended trying to understand this effect. It was merely negated using full magnetic shielding.

The element holder was completely surrounded with a superconducting lead shield as shown in figure 2.10. Care was taken to weld the shield together with a miniature blow torch without introducing non-superconducting material into the lead. This allowed superconducting paths in all directions in the shield.

Lead has a critical field of 0.08 Tesla. To allow a maximum field of 5 Tesla at the centre of the magnet, while having a field of less than 0.04 Tesla at the lead shield, the magnet was raised 5cm to give a total distance from magnet centre to lead shield of 17cm as required by figure 2.14.

Under these conditions the detector output was unaffected by the magnet.

2.2.8 Sample holders

The smaller bolometer system has a sample holder capable of holding multiple samples, filters and polarizers. It consists of two circular discs one above the other, each having four positions which can be rotated into the radiation beam (Vickers 1981). The bottom disc is very easily removed for when hygroscopic samples have to be mounted in a dry box. The samples themselves are mounted in sample holders that simply drop into the spaces in the rotating discs.

The larger bolometer system needed to have a sample holder such that the field of the magnet was parallel to the electric vector of the radiation (figure 2.18). As the radiation propogates down the bore of the magnet, the only way this could be achieved was to reflect the radiation perpendicular to the magnet bore, through the sample and then reflect the radiation once again parallel to the magnet bore. This all had to be done within the magnet's bore of diameter 2.5cm and so limiting the light pipe diameter to 0.7cm at the sample position. The sample holder was detachable from the light pipe so that samples could be mounted within a dry box.

The polarizers used were gold strips on mylar with 394 lines per centimetre (Buckbee Mears Ltd.). Short wavelength, room temperature radiation was prevented from reaching the element by black polythene which is opaque for frequencies above 500 cm^{-1}. It is inserted over the sapphire window to the detector can.

2.2.9 Cool Down Procedure

Before the first experiment with the new bolometer is performed, the lower can containing the element is evacuated and approximately 20ml of helium gas at atmospheric pressure is let into the can. The gas provides a good thermal link between the detector block and the outer can ensuring that the detector block cools with the rest of the apparatus. When the block cools below 40K the helium gas is adsorbed by 5ml of activated charcoal attached to the detector block (figure 2.10).

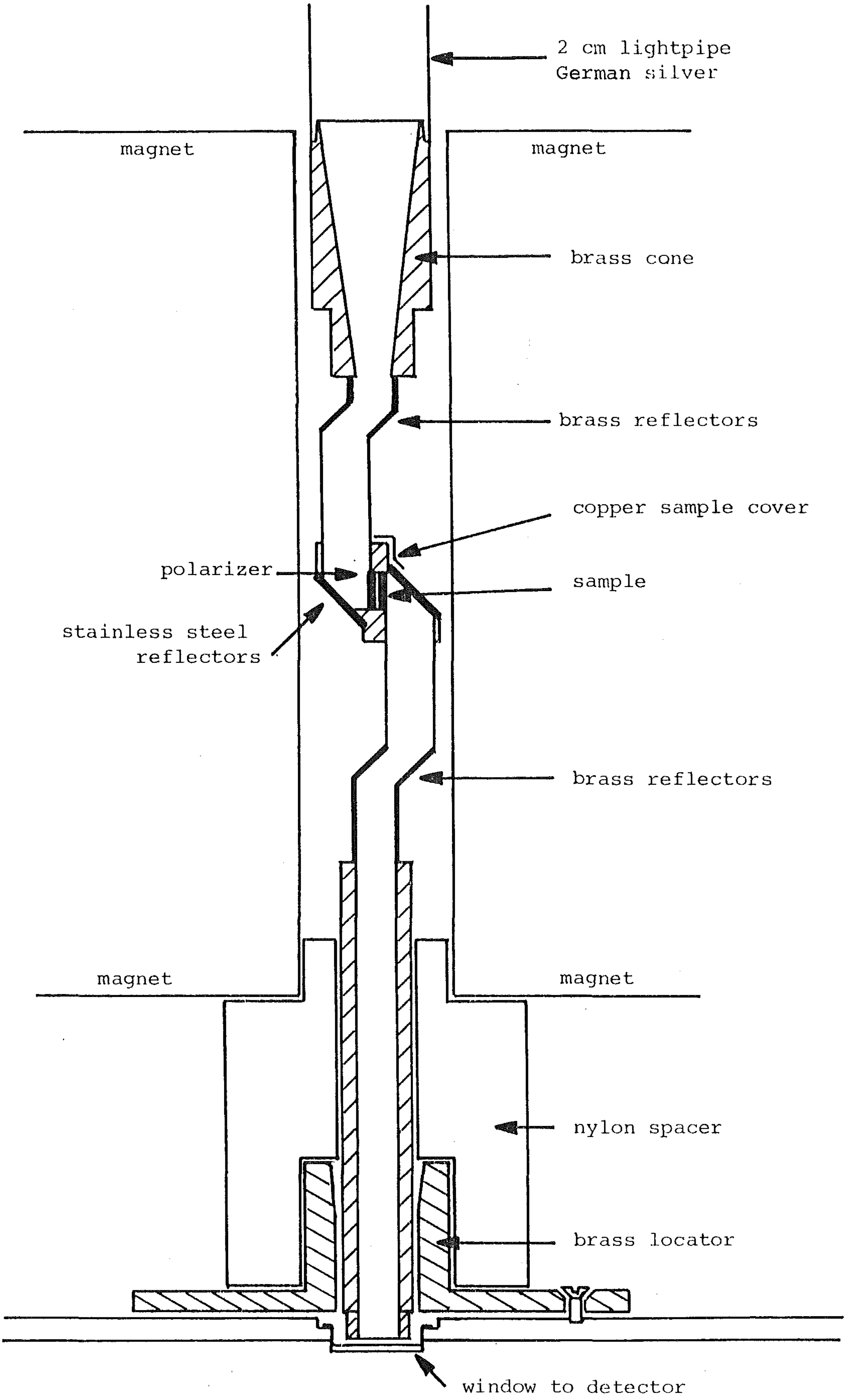

FIGURE 2.18 Cross-section through magnet and sample holder

Before each experiment the vacuum space around the charcoal pump of the refrigerator is evacuated and back-filled with air at room pressure. The samples are then inserted into the holder, the detector system lowered into place and the cryostat evacuated and back-filled with dry helium gas. The whole system is cooled overnight by the liquid nitrogen cryostat. Fifty liquid litres are needed for the initial cooldown and fifty more litres are needed to top up during the experiment.

Liquid helium is transferred into the inner glass Dewar and the transfer tube withdrawn. The helium is pumped to below 20 Torr to allow the He^3 to condense. During the transfer up to eight liquid litres of helium will boil off. A puff of helium gas is then inserted into the chamber around the charcoal pump to cool the charcoal and activate the pump. The helium bath rapidly starts to boil. At this stage the pressure in the liquid helium Dewar is allowed to return to room pressure. Care needs to be taken that the pressure inside the pyrex Dewar does not exceed atmospheric. More liquid helium is then transferred into the Dewar. While transferring, the pressure inside the Dewar is pumped down to about 350 Torr. When the transfer is complete the pressure is allowed to climb back to atmospheric to enable the transfer tube to be withdrawn. The Dewar is then pumped back to below 20 Torr. This procedure means that a maximum amount of liquid helium remains in the Dewar after the cool down procedure.

From the start of the liquid helium transfer until the detector is ready to record spectra,the time elapsed is typically 3.5 hours. The procedure uses about thirty litres of liquid helium and gives a total operating time of 24 hours. This time includes three rejuvinations of the charcoal pump.

2.3 SAMPLE PREPARATION

2.3.1 Crystal Growth

The AMX_3 (A = Cs,Rb: M = Mg,Mn,Fe,Co,Ni: X= Br,Cl) type crystals were prepared using the Bridgman-Stockbarger method. Salts of the type AX and MX_2 were dryed and mixed together in the correct stociometric quantities. The appropriate halogen acid gas (e.g. Hydrogen Bromide for bromide compounds) was passed through the mixture to remove hydroxyl ions as the mixture was slowly heated , for half a day, to just above its melting point. The mixture was then sealed in 1cm diameter quartz tubes and slowly lowered through a temperature gradient. This varied from 50 degrees per centimetre to 70 degrees per centimetre and lowering rates were between 0.6mm and 4mm per hour giving total growth times from 2 days to 2 weeks. For most crystals a lowering rate of 1mm per hour and a temperature gradient of 60 degrees Celsius per centimetre was used. The most difficult crystal to grow was $RbCoBr_3$ which needed the slowest lowering rate. Even then only about half of the attempts to grow this crystal were successful.

As these crystals are hygroscopic the capsules were broken open in a dry box kept at lower than fifteen percent humidity.

2.3.2 Sample Preparation

The samples cleaved parallel to the crystallographic c axis and so samples of the order of a millimetre or two thicknesses were prepared by cleaving. Thinner samples were prepared by sticking the cleaved surface of a thick sample onto a sapphire substrate. Once stuck on the substrate the crystal samples were carefully thinned using coarse P400 grade Carborundum emery paper and then fine C135E Carborundum polishing paper. Samples as thin as 50 microns were achieved.

The sapphire substrates were 1mm thick. Their lower sides are roughened with a dentist's diamond wheel to prevent "thin film" interference in the substrate.

Most samples were stuck to the sapphire substrate using cyanoacrylate (Aron Alpha) glue. For some ($RbMnBr_3$, $CsMgBr_3$, $RbFeCl_3$, $CsFeCl_3$, $CsNiCl_3$ and $RbNiCl_3$) this method did not work. In these cases double sided sellotape was used.

For very thin samples stuck on sellotape, the crystal tended to powderize. Also the sellotape tended to lift from the substrate when cooled to low temperatures. This was overcome by liberally coating the edges of the sellotape with vacuum grease. The grease solidifies to a glass at lower temperatures and bonds the sellotape to the substrate.

CHAPTER 3

RADIATION TRANSMISSION THROUGH A DIELECTRIC SLAB

3.1 INTRODUCTION

The analysis of far infrared absorption spectra of phonons in anisotropic, dielectric crystals requires a knowledge of the way radiation is transmitted through the dielectric medium.

Born and Huang (1954) derived an expression for the transmission of radiation at normal incidence through thin films of isotropic dielectric, by matching the electric and magnetic fields of the radiation at the film surfaces. They showed that very thin films have a transmission minimum at the transverse optical phonon frequency (ν_{TO}).

These results were extended by Berreman (1963) to the case of non-normal incidence. For radiation polarised with the electric vector normal to the plane of incidence (the s polarized wave) the transmission minimum is at the transverse optical frequency while for radiation polarised with the electric vector in the plane of incidence (the p polarized wave) an additional minimum occurs at the longitudinal optical frequency (ν_{LO}).

Campbell and Vickers (1983) (appendix 2) generalised Berreman's results to the case of anisotropic thin films for their study of phonons in $CdCl_2$ type crystals. This work is now extended to the case of thick slabs of anisotropic dielectric crystals mounted on a substrate.

3.2 NOTATION

Consider an anisotropic crystal of thickness d in the x direction, infinitely long in the y and z directions and supported on one side by a substrate (figure 3.1). The dielectric constants within the crystal are assumed to be resolved into independent components along the x,y and z directions only and one of the crystal axes is aligned parallel to the crystal surface.

This means that the dielectric tensor is of the form

$$\begin{matrix} \varepsilon_{xx} & 0 & 0 \\ 0 & \varepsilon_{yy} & 0 \\ 0 & 0 & \varepsilon_{zz} \end{matrix}$$

This applies for all crystal structures with point groups with functions x^2, y^2, z^2 as the basis for the irreducible representation $A_{1(g)}$ namely:

D_2 D_{2h} C_{2v}

where ε_{xx}, ε_{yy} and ε_{zz} are independent;

D_4, D_{4h}, C_{4v}, D_{2d}, D_3, D_{3d}, C_{3v}, D_6, D_{6h}, C_{6v} and D_{3h}

where $\varepsilon_{xx} = \varepsilon_{yy}$;

and T, T_h, O, O_h, and T_d where $\varepsilon_{xx} = \varepsilon_{yy} = \varepsilon_{zz}$.

The radiation is incident in the x-y plane. Since the electromagnetic wave travels in the x-y plane its wave vector in the z direction (K_z) is always zero. The time dependence of the radiation is $e^{-i(2\pi\nu c)t}$

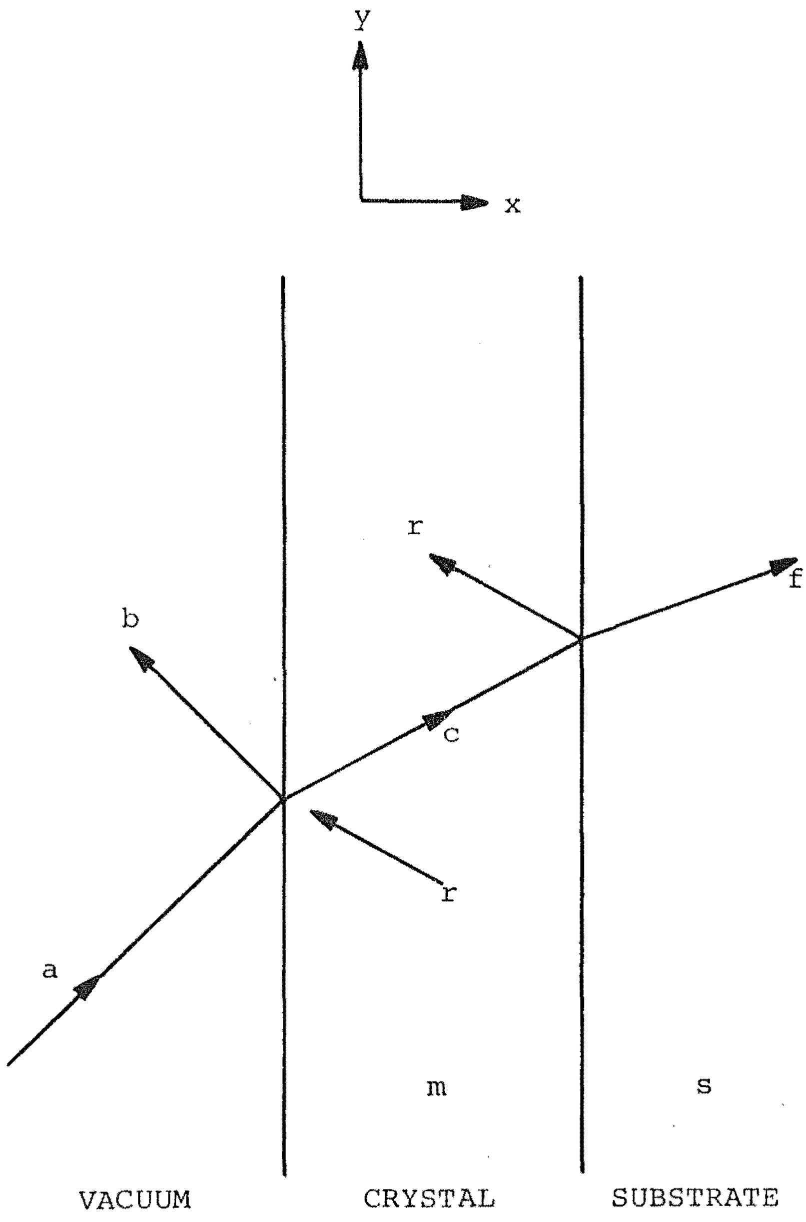

Figure 3.1 Transmission of off-axis radiation through a slab of dielectric bonded to a substrate. The lower r is from a reflection of another ray off the crystal-substrate interface.

The following notation is used in this chapter

c	is the speed of light in vacuum
E_y^b	the y component of the electric field for the ray b as in figure 3.1
ν	the wave frequency in units of reciprocal wavelength
$K = 2\pi\nu$	the magnitude of the electromagnetic wave vector in vacuum
K_x^m	the x component of the wavector in the crystal
ε	the dielectric constant of the isotropic substrate
ε_x	the x component of the dielectric function in the crystal (i.e ε_{xx}).

Parameters labelled with single primes refer to real parts, and with double primes refer to imaginary parts, of functions.

3.3 S POLARISED RADIATION

For s polarization, the electric vector is perpendicular to the plane of incidence. Hence E_x, E_y, B_z and K_z are all zero.

The electric and magnetic fields tangential to an interface are continuous across the interface. For a non-magnetic dielectric, so also is the component of the magnetic field perpendicular to the surface. The electric and magnetic fields of the various rays at the first surface (position X_1,Y_1) are therefore related by

$$E_z^a\, e^{i(K_xX_1+K_yY_1)} + E_z^b\, e^{-i(K_xX_1-K_yY_1)}$$
$$= E_z^c\, e^{i(K_x^mX_1+K_y^mY_1)} + E_z^r\, e^{-i(K_x^mX_1-K_y^mY_1)}$$

$$-B_y^a\, e^{i(K_xX_1+K_yY_1)} + B_y^b\, e^{-i(K_xX_1-K_yY_1)}$$
$$= -B_y^c e^{i(K_x^mX_1+K_y^mY_1)} + B_y^r\, e^{-i(K_x^mX_1-K_y^mY_1)}$$

$$B_x^a\, e^{i(K_xX_1+K_yY_1)} + B_x^b\, e^{-i(K_xX_1-K_yY_1)}$$
$$= B_x^c e^{i(K_x^mX_1+K_y^mY_1)} + B_x^r\, e^{-i(K_x^mX_1-K_y^mY_1)}$$

where the sign reversal on B_y^a and B_y^c is to ensure that $\underline{E} \times \underline{H}$ (the Poynting vector) is in the direction of travel for the relevant ray as shown in figure 3.2(a).

At the second surface (position X_2, Y_2)

$$E_z^c\, e^{i(K_x^mX_2+K_y^mY_2)} + E_z^r\, e^{-i(K_x^mX_2-K_y^mY_2)} = E_z^f\, e^{i(K_x^sX_2+K_y^sY_2)}$$

$$-B_y^c\, e^{i(K_x^mX_2+K_y^mY_2)} + B_y^r\, e^{-i(K_x^mX_2-K_y^mY_2)} = -B_y^f\, e^{i(K_x^sX_2+K_y^sY_2)}$$

$$B_x^c\, e^{i(K_x^mX_2+K_y^mY_2)} + B_x^r\, e^{-i(K_x^mX_2-K_y^mY_2)} = B_x^f\, e^{i(K_x^sX_2+K_y^sY_2)}$$

For s polarised radiation in a non-isotropic dielectric, Maxwell's equations in the crystal reduce to

$$K_x^mB_y - K_y^mB_x = -2\pi\nu c\mu_o\varepsilon_o\varepsilon_zE_z$$

$$K_y^mE_z = 2\pi\nu cB_x$$

$$K_x^mE_z = -2\pi\nu cB_y$$

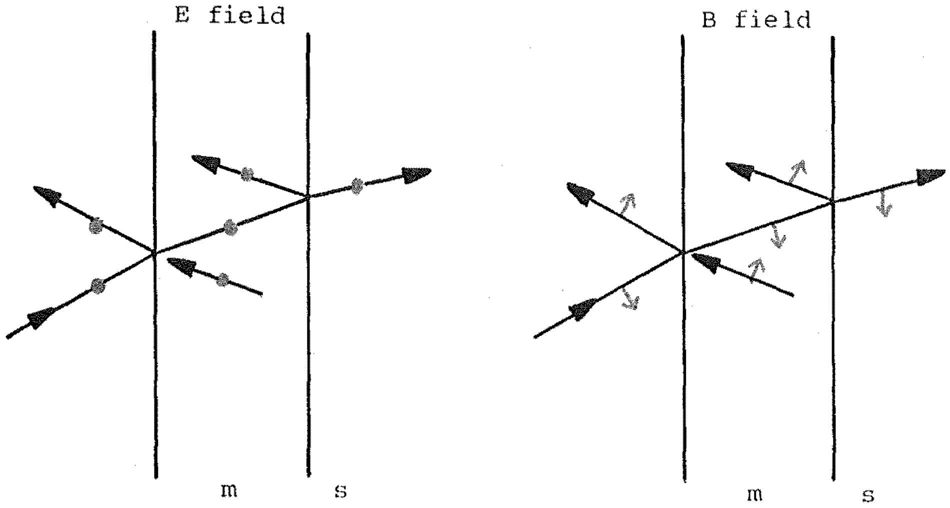

(a) S Polarization

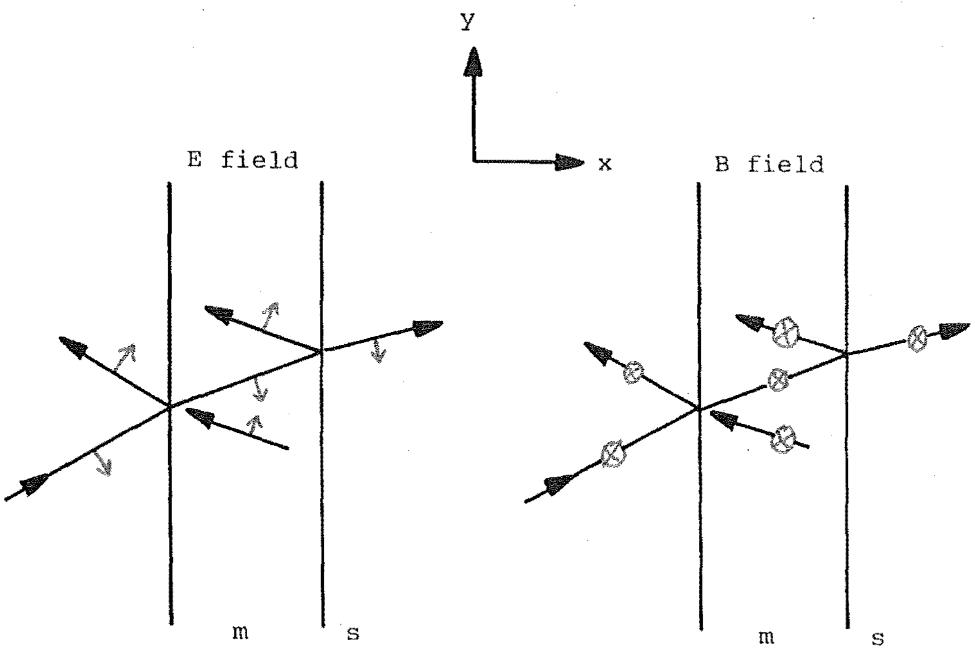

(b) P Polarization

FIGURE 3.2 The relative polarization directions for off-axis rays such that $\underline{E} \times \underline{B}$ is in the direction of travel.

● parallel to z axis ⊗ anti-parallel to z axis where ε_z is the dimensionless, relative dielectric function in the z direction. Similar expressions are obtained for the substrate and the vacuum.

Using these Maxwell's equations, the slab equations can be rewritten in terms of the z component of the electric fields :

$$E_z^a\, e^{i(K_x X_1+K_y Y_1)} + E_z^b\, e^{-i(K_x X_1-K_y Y_1)} = E_z^c\, e^{i(K_x^m X_1+K_y^m Y_1)} + E_z^r\, e^{-i(K_x^m X_1-K_y^m Y_1)} \qquad (3.1)$$

$$E_z^a\, e^{i(K_x X_1+K_y Y_1)} - E_z^b\, e^{-i(K_x X_1-K_y Y_1)} = \frac{K_x^m}{K_x}[E_z^c\, e^{i(K_x^m X_1+K_y^m Y_1)} - E_z^r\, e^{-i(K_x^m X_1-K_y^m Y_1)}] \qquad (3.2)$$

$$E_z^a\, e^{i(K_x X_1+K_y Y_1)} + E_z^b\, e^{-i(K_x X_1-K_y Y_1)} = \frac{K_y^m}{K_y}[E_z^c\, e^{i(K_x^m X_1+K_y^m Y_1)} + E_z^r\, e^{-i(K_x^m X_1-K_y^m Y_1)}] \qquad (3.3)$$

$$E_z^c\, e^{i(K_x^m X_2+K_y^m Y_2)} + E_z^r\, e^{-i(K_x^m X_2-K_y^m Y_2)} = E_z^f\, e^{i(K_x^s X_2+K_y^s Y_2)} \qquad (3.4)$$

$$E_z^c\, e^{i(K_x^m X_2+K_y^m Y_2)} - E_z^r\, e^{-i(K_x^m X_2-K_y^m Y_2)} = \frac{K_x^s}{K_x^m} E_z^f\, e^{i(K_x^s X_2+K_y^s Y_2)} \qquad (3.5)$$

$$E_z^c\, e^{i(K_x^m X_2+K_y^m Y_2)} + E_z^r\, e^{-i(K_x^m X_2-K_y^m Y_2)} = \frac{K_y^s}{K_y^m} E_z^f\, e^{i(K_x^s X_2+K_y^s Y_2)} \qquad (3.6)$$

Comparing equations 3.1 and 3.3 gives $K_y=K_y^m$. Similarly equations 3.6 and 3.4 give $K_y^m=K_y^s$ i.e the wavector in the direction parallel to the slab surface is independent of the slab material.

The slab equations therefore reduce to four equations :

$$E_z^a e^{iK_xX_1} + E_z^b e^{-iK_xX_1} = E_z^c e^{iK_x^mX_1} + E_z^r e^{-iK_x^mX_1}$$

$$E_z^a e^{iK_xX_1} - E_z^b e^{-iK_xX_1} = \frac{K_x^m}{K_x}[E_z^c e^{iK_x^mX_1} - E_z^r e^{-iK_x^mX_1}]$$

$$E_z^c e^{iK_x^mX_2} + E_z^r e^{-iK_x^mX_2} = E_z^f e^{iK_x^sX_2}$$

$$E_z^c e^{iK_x^mX_2} - E_z^r e^{-iK_x^mX_2} = \frac{K_x^s}{K_x^m} E_z^f e^{iK_x^sX_2}$$

These equations can be solved to obtain the ratio of the amplitude of the transmitted electric vector to the amplitude of the incident electric vector to give

$$\frac{E_z^f e^{iK_x^sX_2}}{E_z^a e^{iK_xX_1}} = \frac{4\left(\frac{K_x^m}{K_x^s}\right)}{\left(1+\frac{K_x^m}{K_x}\right)\left(1+\frac{K_x^m}{K_x^s}\right) e^{-iK_x^md} - \left(1-\frac{K_x^m}{K_x}\right)\left(1-\frac{K_x^m}{K_x^s}\right) e^{+iK_x^md}} \qquad (3.7)$$

where $d=X_2-X_1$.

The relative intensity transmission through the crystal and into the substrate is determined by multiplying the amplitude transmission ratio by its complex conjugate and by the ratio of the refractive indices of the material on either side of the slab (to take into account the change of wave speed in a medium). Before doing so, it is more convenient to first separate the relative wave vectors into real and imaginary parts to allow for them being complex i.e for an absorbing crystal.

The parameters in the amplitude transmission are

$$\frac{K_x^m}{K_x^s}\ ,\quad \frac{K_x^m}{K_x}\quad \text{and}\quad K_x^m$$

and $K_x = K\cos\theta$ where θ is the angle of incidence at the first surface.

Let

$$\frac{K_x^m}{K} = \zeta'+i\zeta'' \qquad \text{where } \zeta' \text{ and } \zeta'' \text{ are both real}$$

$$\frac{K_x^m}{K_x} = \eta'+i\eta'' = \frac{\zeta'+i\zeta''}{\cos\theta}$$

$$\frac{K_x^s}{K_x} = S$$

Using Maxwell's equations $K_x^{m^2}+K_y^2=\varepsilon_z.K^2$ (since K_y^m equals K_y) gives

$$(\zeta'+i\zeta'') = \varepsilon_z'-\sin^2\theta + i\varepsilon_z'' \quad .$$

Squaring and equating real and imaginary parts gives

$$\zeta'^2-\zeta''^2 = \varepsilon_z'-\sin^2\theta$$

$$2\zeta'.\zeta'' = \varepsilon_z''$$

which can be solved for ζ' and ζ''.

Similarly for S which is entirely real

$$S^2 = \frac{\varepsilon-\sin^2\theta}{\cos^2\theta}$$

When the radiation is at normal incidence ζ' is equal to the refractive index of the crystal, while ζ'' is equal to the absorption coefficient of the crystal.

This then yields an Intensity Transmission Ratio of

$$T = \frac{16(\eta'^2+\eta''^2)n}{D}$$

where $D =$

$$[(1+\eta')^2+\eta''^2][(S+\eta')^2+\eta''^2]\ e^{4\pi\nu\zeta''d}$$
$$+\ [(1-\eta')^2+\eta''^2].[(S-\eta')^2+\eta''^2]\ e^{-4\pi\nu\zeta''d}$$
$$-2[(1-\eta'^2+\eta''^2).(S^2-\eta'^2+\eta''^2)\ -4S\eta''^2]\cos(4\pi\nu\zeta'd)$$
$$-4\eta''[S(1-\eta'^2-\eta''^2)+S^2-\eta'^2-\eta''^2]\sin(4\pi\nu\zeta'd)\}$$

and n is the refractive index of the substrate.

Note that the intensity transmission function assumes that the substrate is isotropic and non-absorbing. Also it has made no allowance for reflections from the second surface of the substrate which is assumed to either have non-parallel surfaces or its second surface roughened to avoid standing waves within the substrate. This is normally so in an experiment.

A small correction should be made for losses in transmission due to reflection from the second surface of the substrate. However this correction is independent of frequency and is therefore not important as infrared spectra are always normalised to the maximum transmission.

3.4 P POLARISED RADIATION

For p polarized radiation the electric vector is in the plane of incidence. Hence E_z, B_y,B_x and K_z are all zero.

At an interface between two non-magnetic dielectrics, the tangential components of the electric and the magnetic fields are continuous. For the normal components of the electric field it is the displacement field ($D_x=\varepsilon_0\varepsilon_xE_x$) which is continuous. Let ε_x be the relative dielectric for the x direction of the crystal and ε the dielectric constant of the isotropic substrate. Using figure 3.2 (b) to establish ray and field vector directions, the electric and magnetic fields are therefore related across the first boundary (X_1,Y_1) by

$$E_x^a\, e^{i(K_xX_1+K_yY_1)} + E_x^b\, e^{-i(K_xX_1-K_yY_1)} = \varepsilon_x[\, E_x^c\, e^{i(K_x^mX_1+K_y^mY_1)} + E_x^r\, e^{-i(K_x^mX_1-K_y^mY_1)}]$$

$$-E_y^a\, e^{i(K_xX_1+K_yY_1)} + E_y^b\, e^{-i(K_xX_1-K_yY_1)} = -E_y^c e^{i(K_x^mX_1+K_y^mX_1)} + E_y^r\, e^{-i(K_x^mX_1-K_y^mY_1)}$$

$$B_z^a\, e^{i(K_xX_1+K_yY_1)} + B_z^b\, e^{-i(K_xX_1-K_yY_1)} = B_z^c\, e^{i(K_x^mX_1+K_y^mX_1)} + B_z^r\, e^{-i(K_x^mX_1-K_y^mY_1)} .$$

Matching magnetic and electric fields at the second surface (X_2,Y_2) gives

$$\varepsilon_x [E_x^c e^{i(K_x^m X_2 + K_y^m Y_2)} + E_x^r e^{-i(K_x^m X_2 - K_y^m Y_2)}] = \varepsilon E_x^f e^{i(K_x^s X_2 + K_y^s Y_2)}$$

$$-E_y^c e^{i(K_x^m X_2 + K_y^m Y_2)} + E_y^r e^{-i(K_x^m X_2 - K_y^m Y_2)} = -E_y^f e^{i(K_x^s X_2 + K_y^s Y_2)}$$

$$B_z^c e^{i(K_x^m X_2 + K_y^m Y_2)} + B_z^r e^{-i(K_x^m X_2 - K_y^m Y_2)} = B_z^f e^{i(K_x^s X_2 + K_y^s Y_2)}$$

For p polarised radiation, Maxwell's equations inside the crystal reduce to

$$K_x^m E_y - K_y^m E_x = 2\pi\nu c B_z$$

$$K_y^m B_z = -2\pi\nu c \mu_o \varepsilon_o \varepsilon_x E_x$$

$$K_x^m B_z = -2\pi\nu c \mu_o \varepsilon_o \varepsilon_y E_y$$

with similar equations for the substrate.

Applying Maxwell's equations to the slab equations yields a set of 6 equations in E_y only.

$$E_y^a e^{i(K_x X_1 + K_y Y_1)} + E_y^b e^{-i(K_x X_1 - K_y Y_1)}$$

$$= \varepsilon_y \frac{K_y^m K_x}{K_x^m K_y} [E_y^c e^{i(K_x^m X_1 + K_y^m Y_1)} + E_y^r e^{-i(K_x^m X_1 - K_y^m Y_1)}] \quad (3.8)$$

$$E_y^a e^{i(K_x X_1 + K_y Y_1)} - E_y^b e^{-i(K_x X_1 - K_y Y_1)}$$

$$= E_y^c e^{i(K_x^m X_1 + K_y^m Y_1)} - E_y^r e^{-i(K_x^m X_1 - K_y^m Y_1)} \quad (3.9)$$

$$E_y^a\, e^{i(K_xX_1+K_yY_1)} + E_y^b\, e^{-i(K_xX_1-K_yY_1)}$$

$$= \varepsilon_y \frac{K_x}{K_x^m}[E_y^c\, e^{i(K_x^mX_1+K_y^mY_1)} + E_y^r\, e^{-i(K_x^mX_1-K_y^mY_1)}] \quad (3.10)$$

$$E_y^c\, e^{i(K_x^mX_2+K_y^mY_2)} + E_y^r\, e^{-i(K_x^mX_2-K_y^mY_2)} = \frac{\varepsilon\, K_x^mK_y^s}{\varepsilon_y K_y^mK_x^s} E_y^f\, e^{i(K_x^sX_2-K_y^sY_2)} \quad (3.11)$$

$$E_y^c\, e^{i(K_x^mX_2+K_y^mY_2)} - E_y^r\, e^{-i(K_x^mX_2-K_y^mY_2)} = E_y^f\, e^{i(K_x^sX_2-K_y^sY_2)} \quad (3.12)$$

$$E_y^c\, e^{i(K_x^mX_1+K_y^mY_2)} + E_y^r\, e^{-i(K_x^mX_1-K_y^mY_2)} = \frac{\varepsilon\, K_x^m}{\varepsilon_y K_x^m} E_y^f\, e^{i(K_x^sX_2-K_y^sY_2)} \quad (3.13)$$

Comparing equations 3.8 and 3.10 shows that $K_y=K_y^m$ and similarly equations 3.11 and 3.13 give $K_y^m=K_y^s$. The slab equations therefore reduce to four equations.

$$E_y^a\, e^{iK_xX_1} + E_y^b\, e^{-iK_xX_1} = \varepsilon_y \frac{K_x}{K_x^m}[E_y^c\, e^{iK_x^mX_1} + E_y^r\, e^{-iK_x^mX_1}]$$

$$E_y^a\, e^{iK_xX_1} - E_y^b\, e^{-iK_xX_1} = E_y^c\, e^{iK_x^mX_1} - E_y^r\, e^{-iK_x^mX_1}$$

$$E_y^c\, e^{iK_x^mX_2} + E_y^r\, e^{-iK_x^mX_2} = \frac{\varepsilon\, K_x^m}{\varepsilon_y K_x^s} E_y^f\, e^{iK_x^sX_2}$$

$$E_y^c\, e^{iK_x^mX_2} - E_y^c\, e^{-iK_x^mX_2} = E_y^f\, e^{iK_x^sX_2}$$

These equations can be solved to obtain the ratio of the amplitude of the y component of the transmitted electric vector to the amplitude of the y component of the incident electric vector.

$$\frac{E_y^f e^{iK_x^s X_2}}{E_y^a e^{iK_x X_1}} = \frac{4\dfrac{\varepsilon_y K_x^s}{\varepsilon K_x^m}}{(1+\dfrac{\varepsilon_y K_x}{K_x^m})(1+\dfrac{\varepsilon_y K_x^s}{\varepsilon K_x^m})e^{-iK_x^m d} - (1-\dfrac{\varepsilon_y K_x}{K_x^m})(1-\dfrac{\varepsilon_y K_x^s}{\varepsilon K_x^m})e^{iK_x^m d}} \quad (3.14)$$

Defining

$$\rho'+i\rho'' = \frac{K_x^m}{K}$$

$$\sigma'+i\sigma'' = \frac{\varepsilon_y K_x}{K_x^m}$$

$$P = \frac{\varepsilon K_x}{K_x^s}$$

and from Maxwell's equations together with $K_y^m = K_y$

$$\frac{K_x^{m^2}}{\varepsilon_y} + \frac{K_y^2}{\varepsilon_x} = K^2$$

gives

$$(\rho'+i\rho'')^2 = \frac{\varepsilon_y(\varepsilon_x - \sin^2\theta)}{\varepsilon_x}$$

$$(\sigma'+i\sigma'')^2 = \frac{\varepsilon_y \varepsilon_x \cos^2\theta}{\varepsilon_x - \sin^2\theta}$$

$$P^2 = \frac{\varepsilon^2 \cos^2(\theta)}{\varepsilon - \sin^2(\theta)}$$

squaring and equating real and imaginary parts

$$\rho'^2 - \rho''^2 = \varepsilon_y' - \frac{(\varepsilon_y'.\varepsilon_x' + \varepsilon_y''.\varepsilon_x'').\sin^2\theta}{\varepsilon_x'^2 + \varepsilon_x''^2}$$

$$2\rho'\rho'' = \varepsilon''_y + \frac{(\varepsilon'_y.\varepsilon''_x - \varepsilon''_y.\varepsilon'_x).\sin^2\theta}{\varepsilon'^2_x + \varepsilon''^2_x}$$

$$\sigma'^2 - \sigma''^2 = \frac{[(\varepsilon'^2_x + \varepsilon''^2_x)\varepsilon'_y + (\varepsilon''_x\varepsilon''_y - \varepsilon'_x\varepsilon'_y)\sin^2\theta]\cos^2\theta}{(\varepsilon'_x - \sin^2\theta)^2 + \varepsilon''^2_x}$$

$$2\sigma'\sigma'' = \frac{[(\varepsilon'^2_x + \varepsilon''^2_x)\varepsilon''_y - (\varepsilon'_x\varepsilon''_y + \varepsilon''_x\varepsilon'_y)\sin^2(\theta)]\cos^2(\theta)}{(\varepsilon'_x - \sin^2\theta)^2 + \varepsilon''^2_x} \quad (3.14a)$$

which can be solved for ρ', ρ'', σ' and σ''.

The ratio of the intensity of the radiation transmitted into the substrate to the intensity of the radiation incident on the crystal can then be found.

$$T = \frac{16(\sigma'^2 + \sigma''^2)n}{D}$$

where D =

$$[(1+\sigma')^2+\sigma''^2][(P+\sigma')^2+\sigma''^2]\ e^{4\pi\nu\rho''d}$$

$$+[(1-\sigma')^2+\sigma''^2][(n'-\sigma')^2+\sigma''^2]\ e^{-4\pi\nu\rho''d}$$

$$-2[(1-\sigma'^2+\sigma''^2)(P^2-\sigma'^2+\sigma''^2)\ -4P\sigma''^2]\cos(4\pi\nu\rho'd)$$

$$-4\sigma''[n'(1-\sigma'^2-\sigma''^2)+n'^2-\sigma'^2-\sigma''^2]\sin(4\pi\nu\rho'd)$$

Note that this intensity transmission function assumes that the substrate is isotropic and non-absorbing. Also it has made no allowance for reflections from the second surface of the substrate which is assumed to either have non-parallel surfaces or to have its second surface roughened to avoid standing waves within the substrate.

A small correction should be made for losses in transmission due to reflection from the second surface of the substrate. However this correction is independent of frequency and need not be of concern because it is the frequency dependence of the transmission intensity which is important.

3.5 THE DIELECTRIC FUNCTION

The only term in the intensity transmission functions which can not be evaluated from the information already given is the frequency dependence of the dielectric "constant" for the crystal. This is derived by considering the polarization induced within the dielectric by the applied electric field of the radiation.

With the assumption of motion in one direction only (the direction of the electric field) the equation of motion for the atoms in the crystal is

$$M_\alpha d_\alpha = \sum_\beta \Phi_{\alpha\beta} \, d_\beta + e_\alpha \, E$$

where M_α is the mass of the α atom

e_α is the effective charge of the α atom

d_α is the displacement of the α atom from its equilibrium position

Writing this expression in normal co-ordinates gives

$$q_j = -\nu_j^2 q_j + \Sigma_\alpha \, b_{\alpha j} \frac{e_\alpha}{\sqrt{M_\alpha}} \, E$$

where

$$d_\alpha = \frac{\Sigma_j b_{\alpha j}}{\sqrt{M_\alpha}} q_j \quad .$$

The damping term is introduced by replacing ν_j^2 with $\nu_j^2-i\gamma\nu$ giving

$$-\nu^2 q_j = -\nu_j^2 q_j + \gamma_j \nu q_j + \Sigma_\alpha b_{\alpha j} e_\alpha E \quad .$$

Solving for q_j gives

$$q_j = \frac{\Sigma_\alpha b_{\alpha j} e_\alpha E}{\nu_j^2 - \nu^2 - i\gamma_j \nu} \quad .$$

The polarization induced in the material is

$$P = \varepsilon_o(\varepsilon - 1)E$$

$$= \varepsilon_o(\varepsilon_\infty - 1)E + N_o \Sigma e_\alpha d_\alpha$$

where ε_∞ is the dielectric constant at wavelengths greater than infrared. i.e. due only to the response of the electrons of the atoms,

ε is the relative dielectric constant of the material,

the sum is over the number of ions in a unit cell,

and N_o is the number of unit cells within a unit volume (Nakajima et al 1980).

Solving for ε:

$$\varepsilon = \varepsilon_\infty + \frac{N_o}{\varepsilon_o} \Sigma_\alpha e_\alpha d_\alpha \frac{1}{E} \quad .$$

Now replacing d_α with q_j

$$\varepsilon = \varepsilon_\infty + \frac{N_o}{\varepsilon_o} \Sigma_\alpha e_\alpha b_{j\alpha} \frac{\Sigma_\alpha b_{\alpha j} e_\alpha}{\nu_j^2 - \nu^2 - i\gamma_j \nu}$$

$$\varepsilon = \varepsilon_\infty + \frac{N_o}{\varepsilon_o} \Sigma_j \frac{(\Sigma_\alpha b_{\alpha j} e_\alpha)^2}{\nu_j^2 - \nu^2 - i\gamma_j \nu}$$

i.e.

$$\varepsilon = \varepsilon_{\infty} + \Sigma_j \frac{S_j}{\nu_j^2 - \nu^2 - i\gamma_j \nu} \qquad (3.15)$$

Only infrared active phonons are included because

$$\Sigma_{\alpha} b_{\alpha j} e_{\alpha} = 0$$

for all other modes.

The dielectric function (3.15) is then factorized using the method of Kurosawa (1961):

$$\varepsilon_z(\nu) = \varepsilon_z(\infty) . \prod_j \frac{\nu_{LOzj}^2 - \nu^2 - i\Gamma_{zj} . \nu}{\nu_{TOzj}^2 - \nu^2 - i\gamma_{zj} . \nu} \qquad (3.16)$$

with similar expressions for the x and y directions. The product is over the number of phonons in the appropriate direction. ν_j is now identified as the transverse optical mode (ν_{TOj}). The relationship between S_j, ν_{LO} and Γ, and ν_{TO} and γ can be found by matching the coefficients of ν^n for the two equations. The ν_{TO}, ν_{LO}, γ and Γ are not independent as there are 4m+1 variables in equation 3.16 compared to 3m+1 variables in 3.15 where m is the number of modes. For example equating the coefficients of ν^{2m-1} gives

$$\Sigma_j \gamma_j = \Sigma_j \Gamma_j \quad .$$

When no damping is present both γ and Γ are zero. As expected the dielectric function (equation 3.16) then reduces to that given by Kurosawa (1961).

If $\nu=0$ the dielectric function (equation 3.16) becomes the multimode Lyddane-Sachs-Teller relation

$$\varepsilon_z(0) = \varepsilon_z(\infty) \prod_j \frac{\nu_{LOzj}^2}{\nu_{TOzj}^2}$$

as given by Kurosawa (1961) and by Cochran and Cowley (1962).

3.6 EXAMPLES OF CALCULATED TRANSMISSION SPECTRA

If there is one phonon mode in each x,y and z direction of a crystal and the crystal slab is in the y-z plane then p polarized radiation in the y-z plane will have transmission minima at the frequencies of the transverse optic mode in the y direction and the longitudinal optic mode in the x direction. If the radiation is s polarized there is only one transmission minima at the frequency of the transverse optic mode in the z direction. Figure 3.3 shows this for three arbitrary phonons, one in each direction.

Figure 3.4 illustrates how increasing the damping constant broadens the line and raises the transmission minima. The minima remains at the same frequency although at the longitudinal optic frequency the line becomes slightly asymmetric around the minimum point. This phenomena will be investigated latter in the chapter.

Figure 3.5 shows the effect of thickening the crystal slab. For the minima at the transverse mode frequencies the line bottoms out and the flat bottom of the line spreads to the longitudinal optic mode frequency. This illustrates why the transverse mode frequencies for thick crystals are not in the middle of the absorption lines. To assume so is a quite common misconception.

The line at the frequency of the longitudinal optic mode for p polarized spectra remains symmetric about the

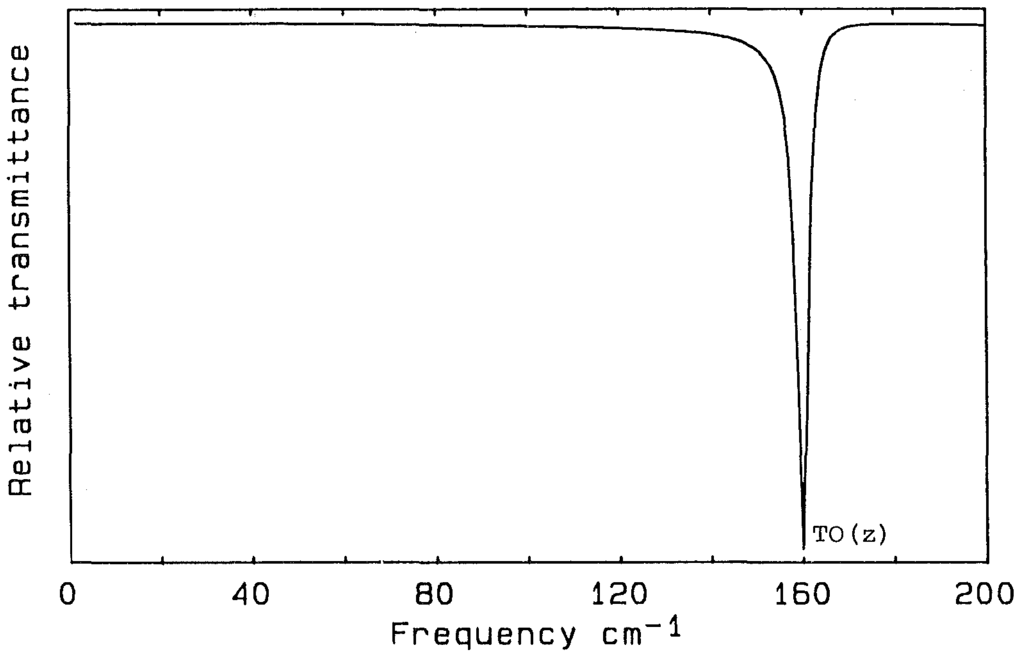

(a) S polarized

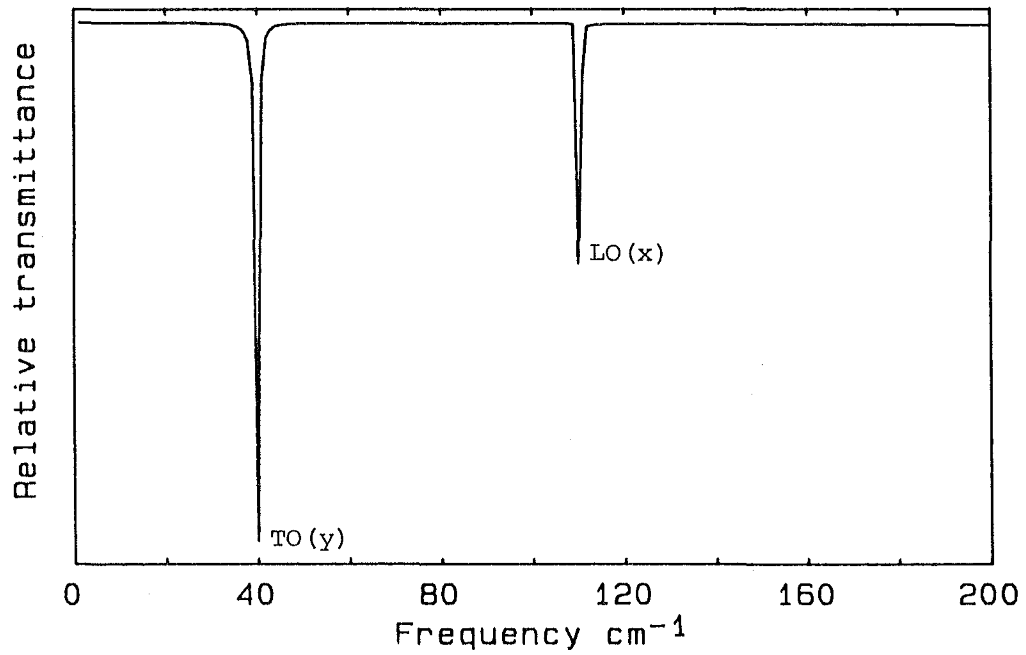

(b) P polarized

Figure 3.3 Absorption lines calculated for polarized radiation incident in the x-y plane, onto a crystal slab in the y-z plane. There is one phonon in each of the x, y and z directions and the phonon frequencies are chosen arbitrarily.

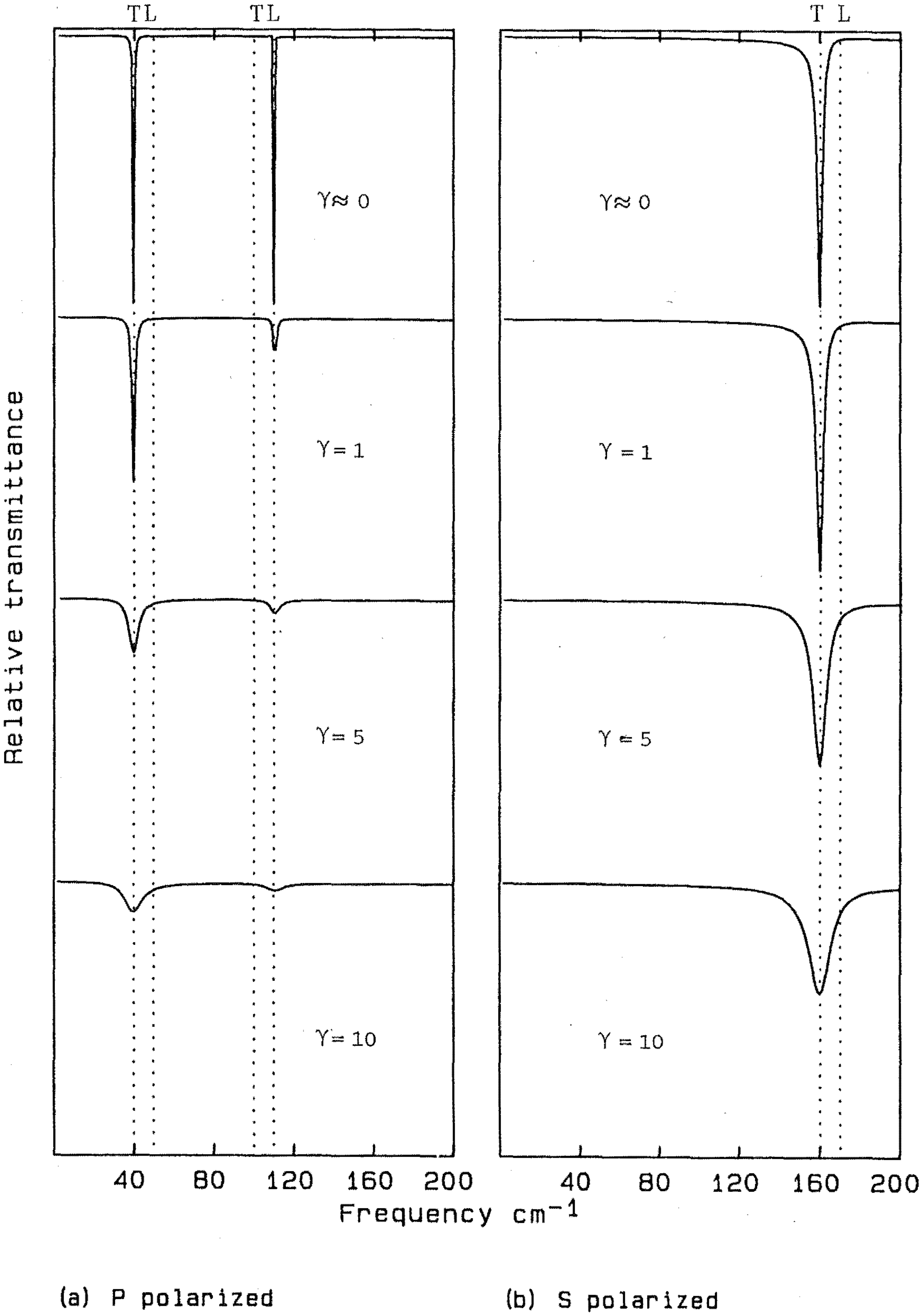

Figure 3.4 Calculated spectra for different damping constants. γ is the damping constant in wavenumbers (cm^{-1}).

longitudinal optic frequency. The sine waves to either side of the absorptions are due to standing waves in the parallel sided sample. Figure 3.6 illustrates how the slab equations will fit standing waves observed in thin parallel sided crystals.

The effect of changing the angle of incidence is illustrated in figure 3.7. For normal incidence there is only absorption at the transverse mode frequencies. As the angle of incidence increases the absorption at the longitudinal mode frequency increases. The transverse mode line in the s polarized spectrum becomes stronger while the one in the p polarized spectrum becomes weaker.

In p polarized spectra using very large angles of incidence, there is another mimima on the high frequency side of the longitudinal mode frequency. The asymmetry of the longitudinal mode for large damping term and the extra line above the longitudinal mode frequency are due to the same phenomenom. There is a transmission minima when the square root of the real part of the dielectric constant in the x direction (i.e. perpendicular to the plane of the crystal slab) is equal to the sine of the angle of incidence (see equation 3.14a). This is equivalent to the critical angle for total internal reflection in an isotropic dielectric. The effect of changing the high frequency dielectric constant and the angle of incidence is seen in figure 3.8.

The addition of more modes does not alter the frequency of the absorption lines due to the existing modes. However the strength of the mode absorptions are changed as

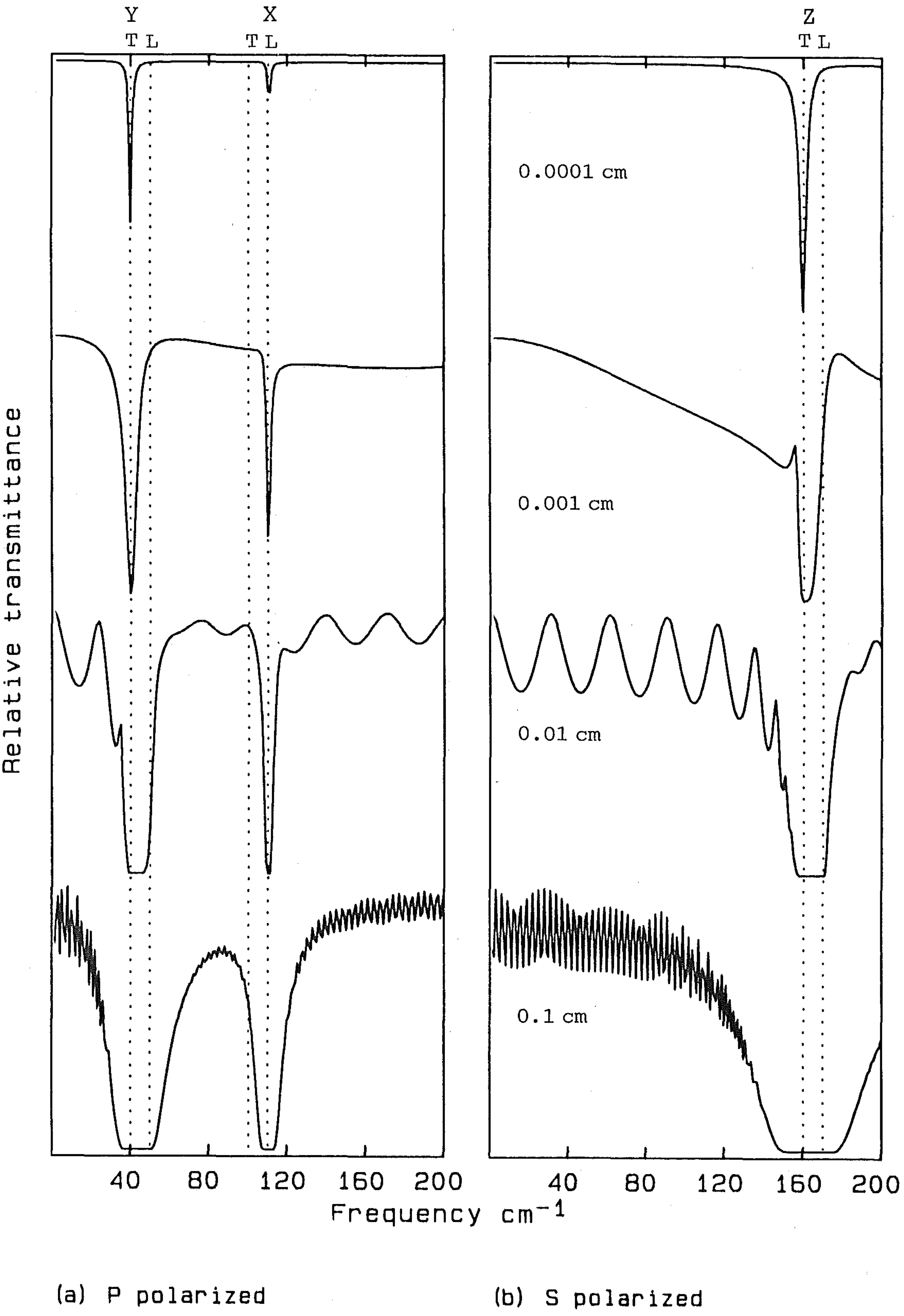

Figure 3.5 Calculated spectra for different thickness of slab without a supporting substrate.

longitudinal optic frequency. The sine waves to either side of the absorptions are due to standing waves in the parallel sided sample. Figure 3.6 illustrates how the slab equations will fit standing waves observed in thin parallel sided crystals.

The effect of changing the angle of incidence is illustrated in figure 3.7. For normal incidence there is only absorption at the transverse mode frequencies. As the angle of incidence increases the absorption at the longitudinal mode frequency increases. The transverse mode line in the s polarized spectrum becomes stronger while the one in the p polarized spectrum becomes weaker.

In p polarized spectra using very large angles of incidence, there is another mimima on the high frequency side of the longitudinal mode frequency. The asymmetry of the longitudinal mode for large damping term and the extra line above the longitudinal mode frequency are due to the same phenomenom. There is a transmission minima when the square root of the real part of the dielectric constant in the x direction (i.e. perpendicular to the plane of the crystal slab) is equal to the sine of the angle of incidence (see equation 3.14a). This is equivalent to the critical angle for total internal reflection in an isotropic dielectric. The effect of changing the high frequency dielectric constant and the angle of incidence is seen in figure 3.8.

The addition of more modes does not alter the frequency of the absorption lines due to the existing modes. However the strength of the mode absorptions are changed as

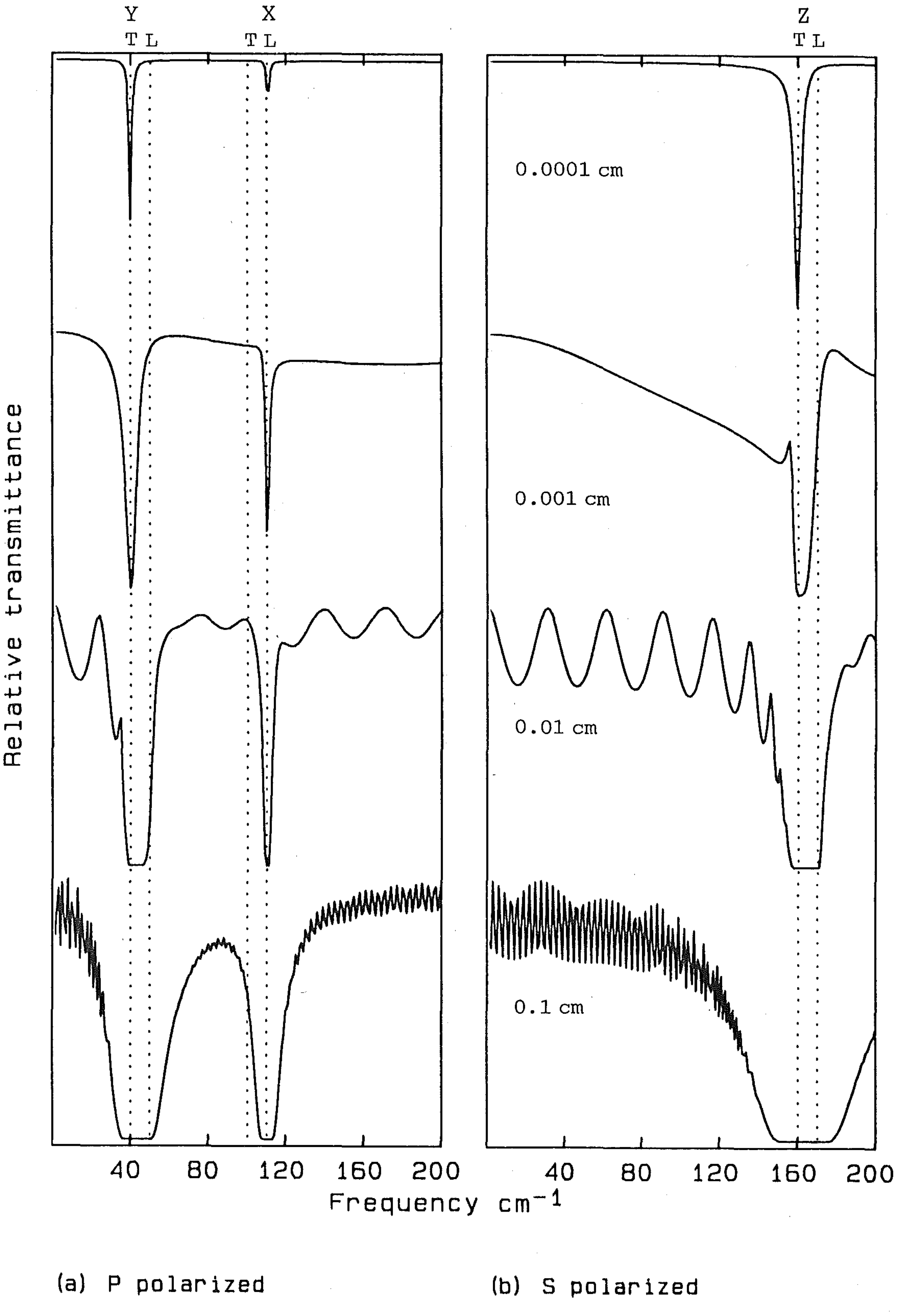

(a) P polarized

(b) S polarized

Figure 3.5 Calculated spectra for different thickness of slab without a supporting substrate.

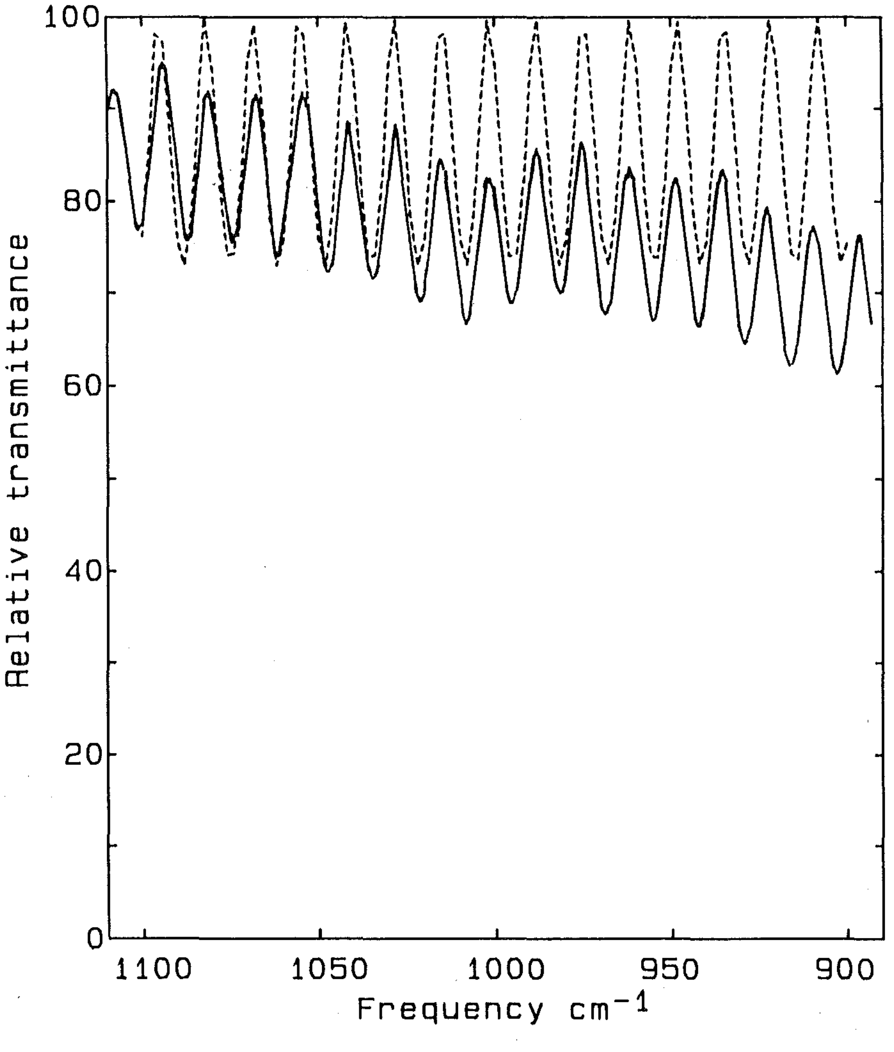

Figure 3.6 Standing waves in a cleaved film of CdI_2 of thickness 0.021cm.

——— Experimental data

------- Fitted calculation using the slab equations.

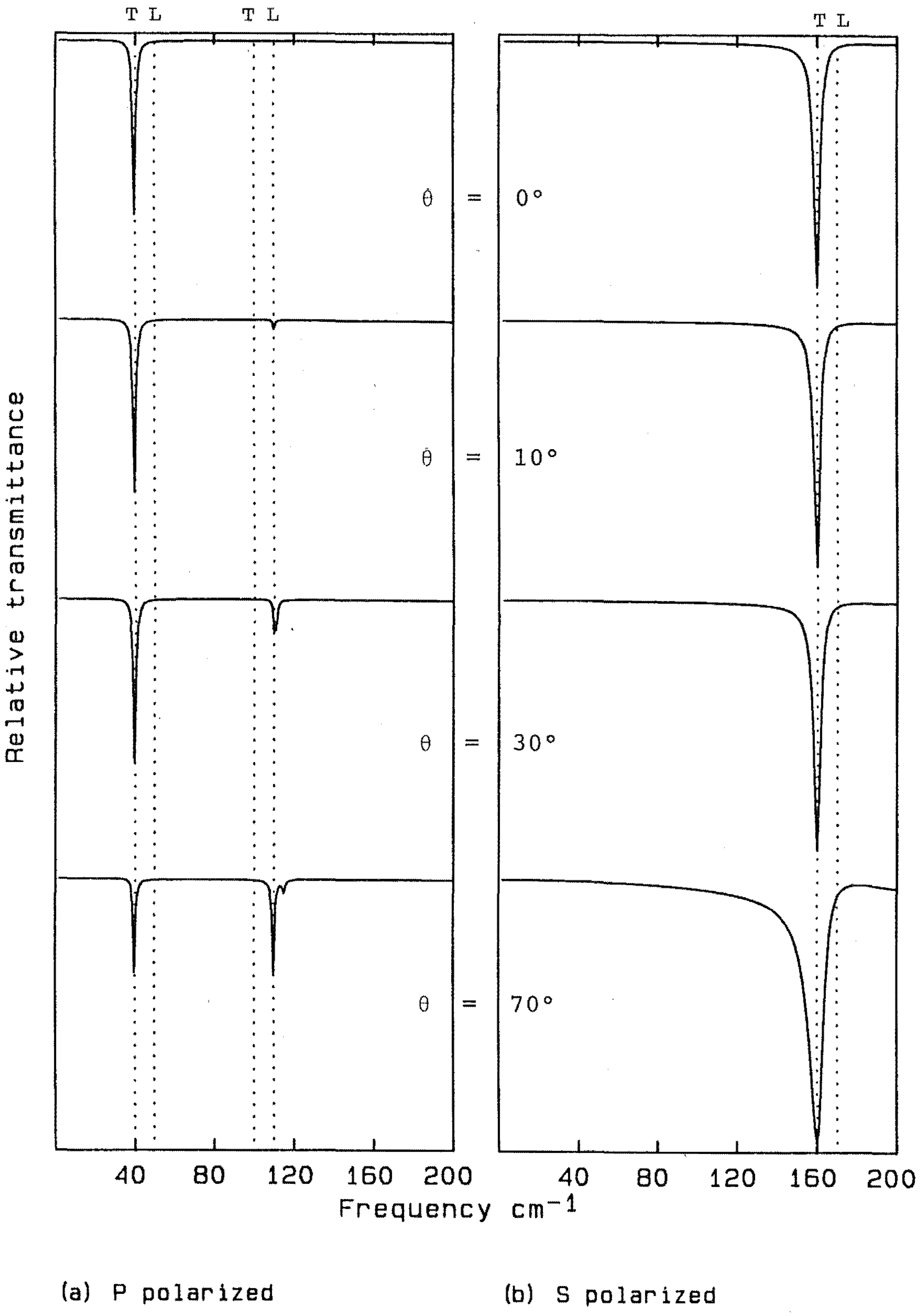

Figure 3.7 Calculated spectra for varying angles of incidence θ.

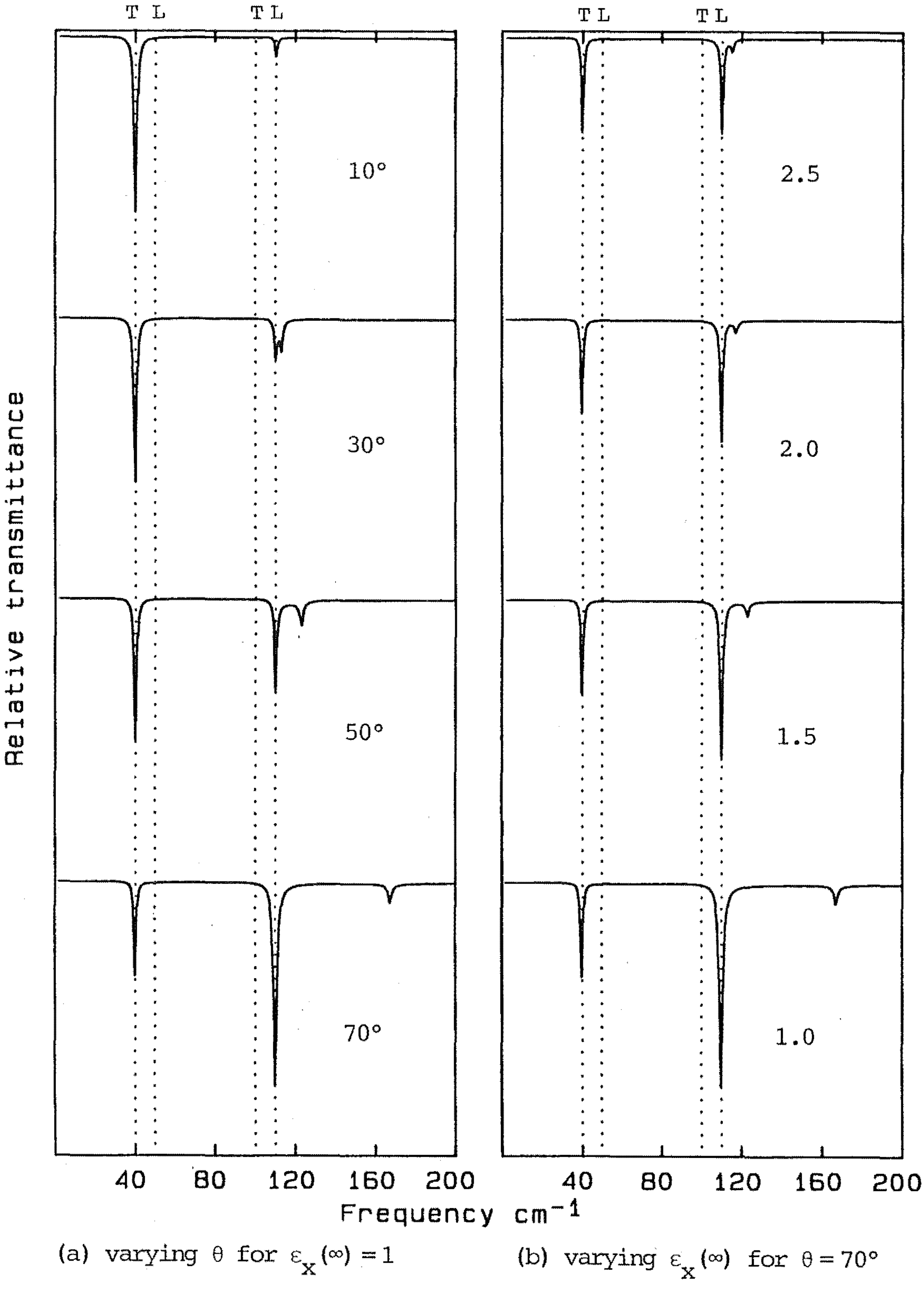

(a) varying θ for $\varepsilon_x(\infty) = 1$ (b) varying $\varepsilon_x(\infty)$ for $\theta = 70°$

Figure 3.8 Calculated spectra for varying angles of incidence (θ) and varying high frequency dielectric constant in the x direction of the crystal ($\varepsilon_x(\infty)$). All spectra are P polarized.

the frequency of the two modes in each direction become closer. Figure 3.9 illustrates this process.

For many experimental situations, the crystal surfaces are not parallel or smooth. Also the incident radiation may not be well collimated. In these cases standing waves are not expected in the crystal. The slab equations were therefore rederived for no reflection from the second surface (X_2,Y_2). The result is that only the first term in the denominator of the transmission ratio for the slabs remains. The practical result of this is seen in figure 3.10 where it can be seen that the shape of the absorption lines are essentially unchanged. The main difference is that the standing waves have disappeared.

Figure 3.11 shows a fit of the slab equations to experimental spectra of a thin crystal of $CsNiBr_3$. The crystal is immersed in liquid helium at 1.7 Kelvin. Liquid helium has a refractive index of 1.05 which is close enough to one to warrent using the slab equations as is. The essential features of the spectra are reproduced well. There are several reasons why the fit may not be exact. There may be other absorptions that are not clearly resolved such as those due to water attack or imperfect polarisation of the sample. Another reason may be that the theory, which is classical, uses a constant damping term while a quantum mechanical theory would use a frequency-dependent damping term (Berreman 1963).

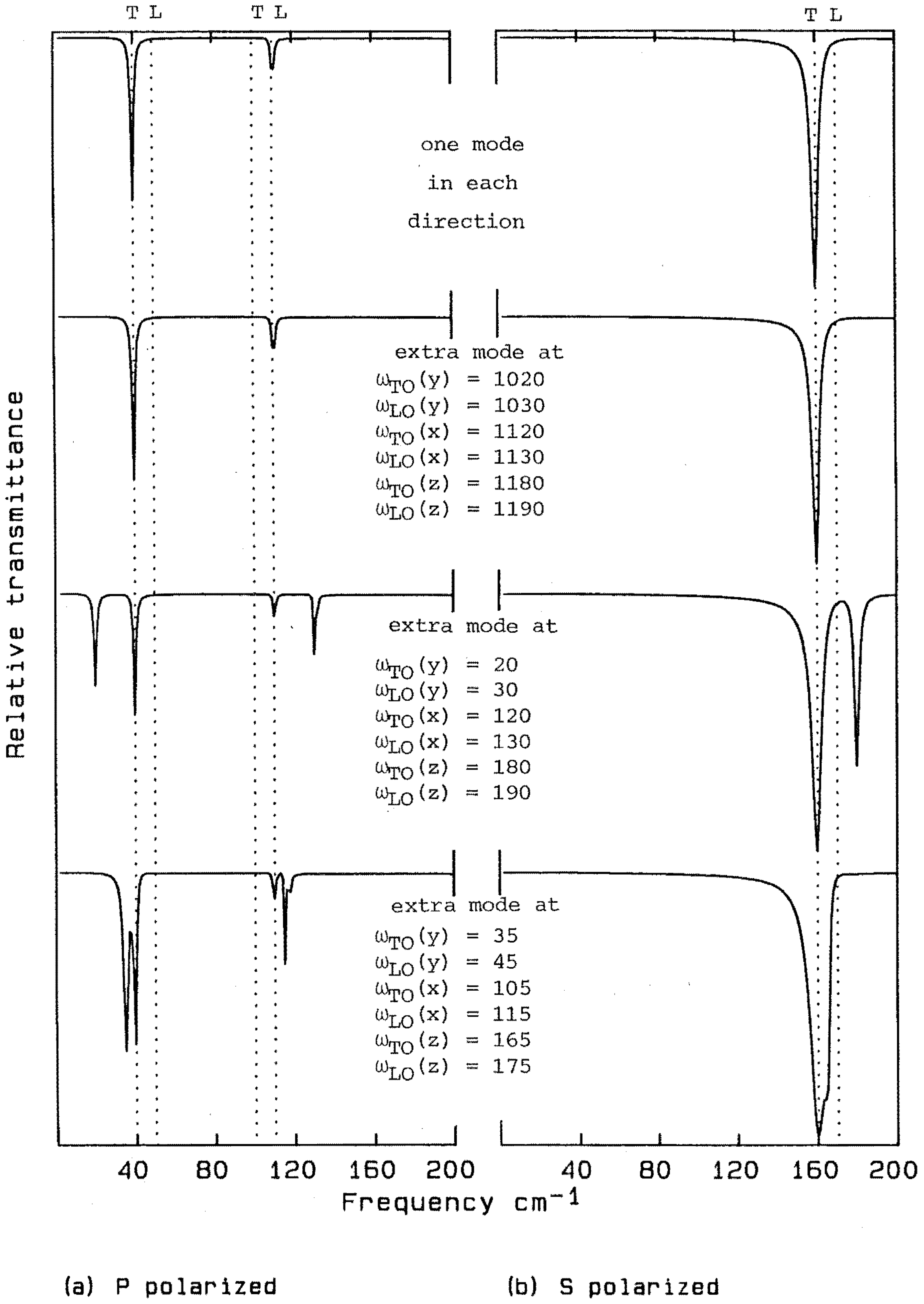

Figure 3.9 Calculated spectra showing the effect of introducing a second mode in each direction. All frequencies are in wavenumbers (cm^{-1}).

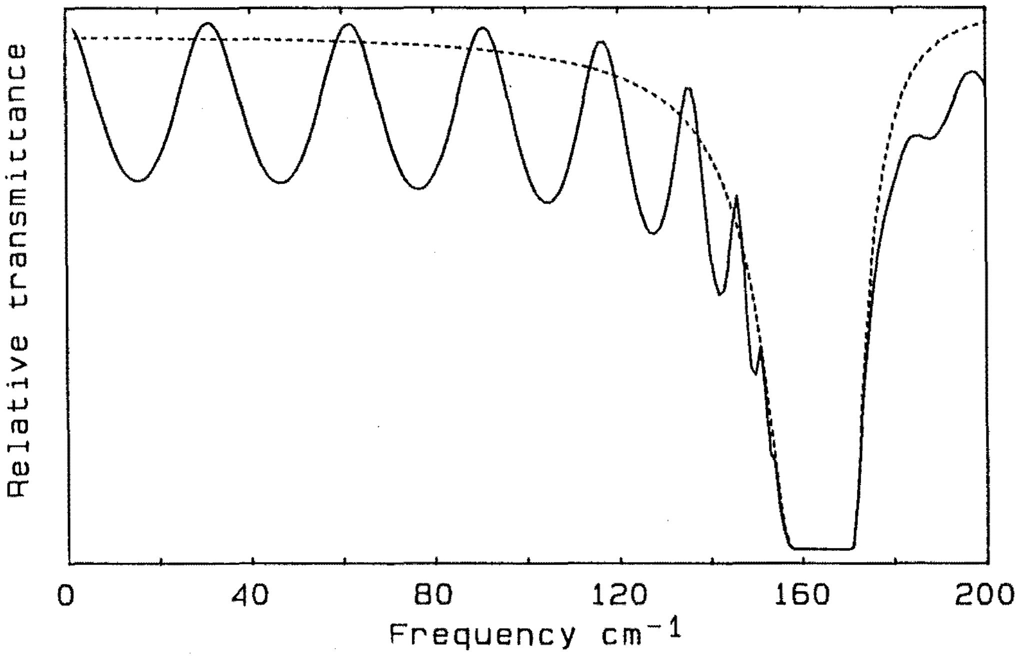

(a) S polarized

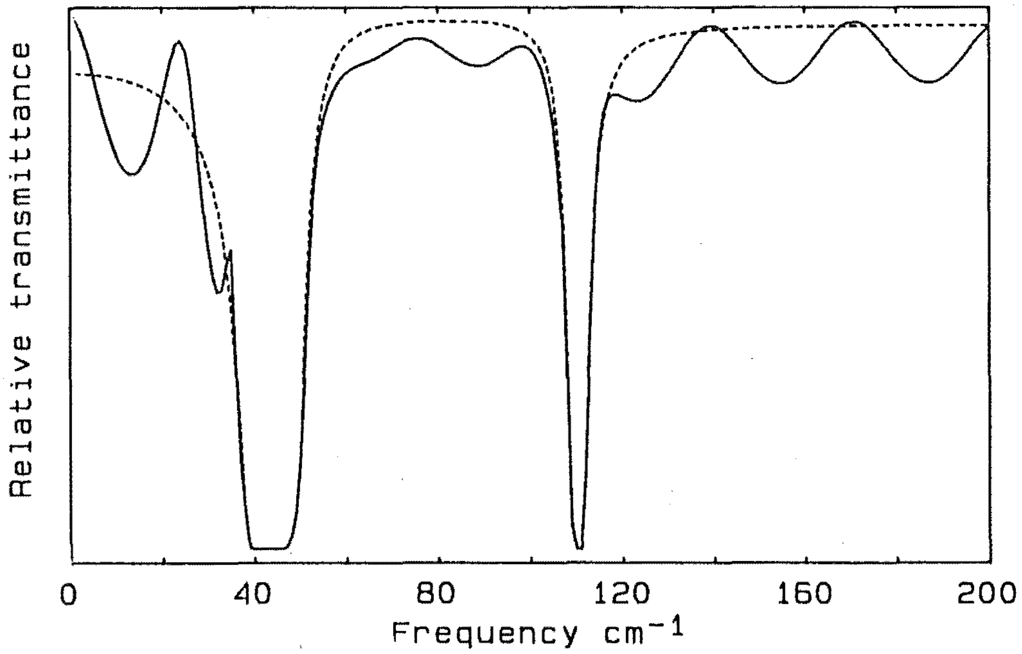

(b) P polarized

Figure 3.10 Calculated spectra with (——) and without (---) reflection from the second surface of the crystal slab.

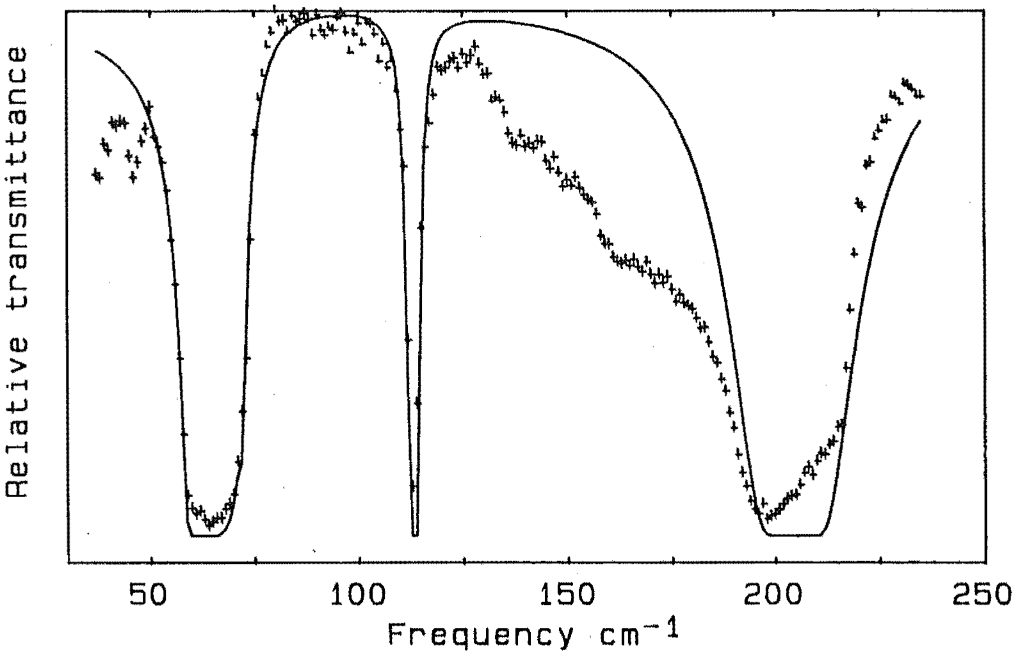

(a) S polarized

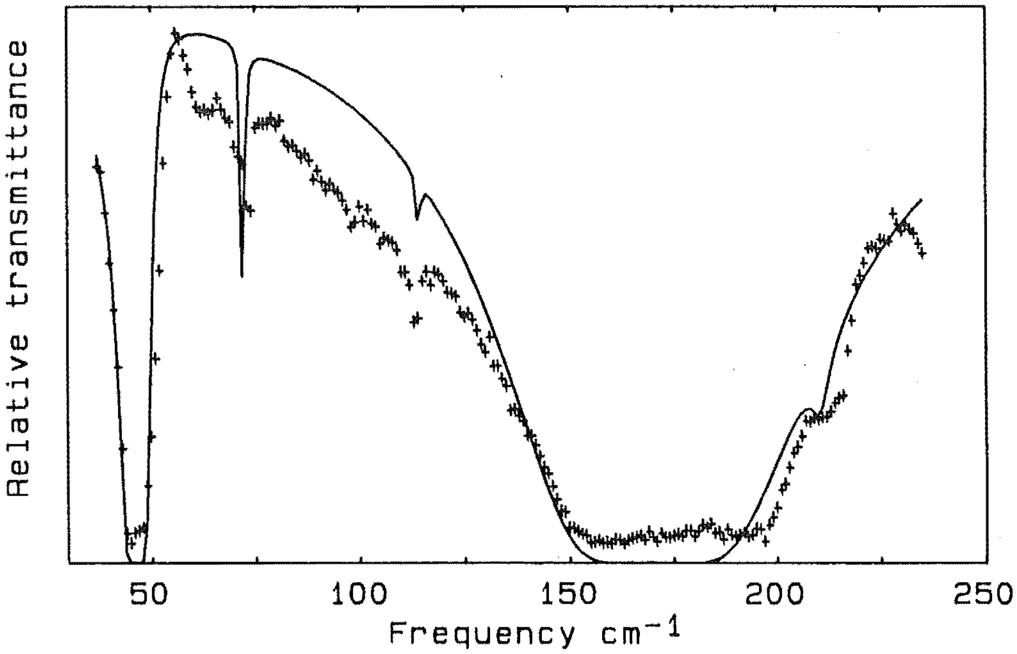

(b) P polarized

Figure 3.11 Fitting of the transmission equations to the spectra of $CsNiBr_3$ at 1.7 K. Sample thickness 0.006 cm.

+ experimental data

- fitted slab equations

3.7 SUMMARY

The slab equations show that for normal incidence of radiation onto a thin crystal, absorption lines are only expected at the transverse optic mode frequencies. As the crystal is thickened the absorption lines have zero transmission over a band of frequencies with the transverse optic mode in the low frequency side and the longitudinal optic mode in the high frequency side. The transverse optic mode is not at the centre of the band as it is too often erroneously assummed.

The longitudinal optic mode can be observed using p polarized radiation at non-normal incidence. As the crystal is thickened, the longitudinal optic lines broaden but are still centred on the longitudinal optic mode frequency.

For high angles of incidence and a material with low refractive index (at high frequencies), there is a possibility of an extra absorption line above the longitudinal optic mode frequency. This is equivalent to total internal reflection for isotropic dielectrics.

The theory derived in this chapter reproduces all the major features of the experimentally determined spectra of $CsNiCl_3$ type crystals.

CHAPTER 4

PHONONS IN AMX_3 TYPE CRYSTALS

4.1 INTRODUCTION

AMX_3 type crystals (where A is Cs or Rb; M is Mn, Fe, Co or Ni and X is Br or Cl) are good examples of one dimensional antiferromagnets (Ackerman et al 1974). As a preliminary to studying the magnetic excitation spectra of these crystals, a full knowledge of their phonon spectra is desirable. This is especially so for the case where coupling between the phonons and the magnons is possible (Lockwood et al 1983).

For AMX_3 type crystals, the Raman and infrared active modes are in two mutually exclusive groups. The frequencies of the Raman active modes have been determined by Breitling et al (1976).

The infrared active modes have been studied by McPherson et al (1973) using powders imbedded in Nujol mulls between polyethylene plates. Spectra of imbedded powders are known to yield misleading results due to the finite size of the crystallites forming the powder and to the influence of the imbedding medium (Frohlich 1948 and Martin 1970). The absorption maxima obtained using powders fall between the transverse and longitudinal mode frequencies of the crystal. Furthermore, powdered samples lead to spectra involving all of the infrared-active modes. Spectra involving single crystals and polarized radiation are necessary to help with phonon assignments.

Chadwick et al (1971) used Kramers-Kronig analysis of the reflectivity spectra from single crystals to deduce the oscillator frequencies of $CsNiCl_3$ and $CsCoCl_3$. These results did not agree with values they obtained from infrared transmission spectra.They also reported infrared transmission spectra for several other crystals of this type.

No studies of the infrared active phonons in $CsNiCl_3$ type crystals have previously used thin, single crystals to accurately determine and assign the phonon frequencies.

The first part of this chapter reviews the theory of normal modes of vibration in crystals and applies this in particular to the $CsNiCl_3$ structure. Following the work of Campbell and Vickers (1983) on $CdCl_2$ type crystals, polarized transmission spectra using thin, single crystals and slightly off-axis radiation were obtained to determine the longitudinal optic (LO) modes as well as the transverse optic (TO) modes for crystals of the $CsNiCl_3$ class. The experimental results are presented in the latter half of this chapter.

4.2 DETERMINATION OF NORMAL MODES

The number and type of normal modes in a crystal for long wavelengths (zero wavevector,K=0) can be found by a factor group analysis (Burns 1977). The factor group of a space group is isomorphic with its point group. This means that all the symmetry operations under which the unit cell remains unchanged can be represented by the point group operations plus translations of the lattice as a whole.

A crystal having N atoms in a unit cell has 3N degrees of freedom at K=0 (one for each of the x,y and z directions of motion for each atom). A matrix for each symmetry operation can be constructed which represents the transformations of these displacements under the symmetry operation. These matrices or representations can then be reduced to irreducible representations which label the normal modes of the crystal. The trace of the representation matrix (the character) is unchanged by the reduction which is given by

$$\chi(R) = \Sigma_j n_j \chi_j(R) \ ,$$

where $\chi(R)$ is the character of the reducible representation,

$\chi_j(R)$ is the character of the jth irreducible representation

n_j the number of times the jth irreducible representation occurs in the reducible representation and

R is the symmetry operation involved.

The number and types of normal mode are given by

$$n_j = \frac{1}{h}\Sigma_R \ \chi_j^*(R) \qquad \text{(Burns 1977 p59)}$$

where h is the number of symmetry operations in the unit cell group (i.e. the order of the group) and * indicates a complex conjugate.

In considering the representation of a symmetry operation on the crystal only those atoms which map onto themselves under the operation need be considered as only these atoms contribute to the trace. Also the specific transformation of the x,y and z components of the atomic displcements need not be considered, since for an atom mapping onto itself the contribution to the trace $\chi_t(R)$ is given by

$$\chi_t(R) = \pm 1 + 2\cos\theta \quad ,$$

where θ is the angle of rotation for the symmetry operation.

+ is used for proper rotations (no reflection involved), and - is used for improper rotations (reflections involved) For pure reflections $\chi_t(R)$ is equal to 1.

The trace for the reducible representation $\chi(R)$ is then found by the sum of $\chi_t(R)$ over all the atoms in the unit cell of the crystal.

4.3 DETERMINATION OF SYMMETRY CO-ORDINATES

Linear combinations of symmetry co-ordinates give eigenvectors which show the motions of atoms corresponding to the normal modes of the crystal. If only one normal mode transforms as a given irreducible representation then the symmetry co-ordinate is the eigenvector which corresponds to the normal mode. The symmetry co-ordinates are obtained using projection operator techniques (Burns 1977) where the character projection operator is

$$V^m = \frac{1_m}{h}\Sigma_R \; \chi_m^*(R)R$$

where R is a symmetry operation and

1_m is the number of partners of the mth irreducible representation. e.g. 2 (i.e x and y) for the E_{1u} mode of D_{6h}.

The factor of 1/h though is irrelevant because the function that results from the projection operators must be separately normalised.

For doubly degenerate modes more information on the symmetry co-ordinates can be gained by using the transfer projection operator V^m_{oi} where

$$V^m_{oi} = \frac{1_m}{h}\Sigma_R\ \Gamma_m^*(R)_{oi}R.$$

$\Gamma_m(R)_{oi}$ is the oi element of the mth irreducible representation.

The projection operators are used to operate on a particular atomic displacement (e.g. on x_1 for motion in the x direction of the 1st atom in a unit cell) and gives the symmetry co-ordinate associated with that particular atom in the direction of displacement.

4.4 CRYSTAL STRUCTURE OF $CsNiCl_3$ TYPE CRYSTALS

The crystals consist of chains of face-sharing MX_6^{4-} octahedra lying along the c axis, each chain being separated from its neighbour by A^+ ions. At least four structural types of such crystals have been identified (Longo et al. 1969) involving different repeat units along the c axis. The different types are labelled 2L,4L,6L and 9L, where the numeral denotes the size of the repeat unit in terms of the number of close packed layers.

The structure with the 2L repetition unit is usually referred to as the $CsNiCl_3$ type structure.It has two formula units to the unit cell. Such crystals include $CsNiCl_3$, $CsMgCl_3$, $CsFeCl_3$, $CsCoCl_3$, $RbFeCl_3$, $RbCoCl_3$, $RbNiCl_3$, $CsMgBr_3$, $CsMnBr_3$, $CsCoBr_3$, $CsNiBr_3$, $RbMnBr_3$ and $RbCoBr_3$.

A diagram of the $CsNiCl_3$ unit cell is shown in figure 4.1 where each atom is numbered for ease of reference. This structure has space group D_{6h}^4 which has a factor group isomorphic to the point group D_{6h}.

4.5 NORMAL MODES OF $CsNiCl_3$ TYPE CRYSTALS

The factor group analysis method is now applied specifically to the $CsNiCl_3$ type structure. Table 4.1 gives the characters ,$\chi_t(R)$, of the representation for all the symmetry operations of the group D_{6h}. The characters are used to construct the column headed $CsNiCl_3$ in table 4.2 which gives the number of times each normal mode or irreducible representation occurs in the representation. The infrared active modes are those which transform in the same way as the cartesian co-ordinates x,y and z. In D_{6h} symmetry these are the A_{2u} and E_{1u} modes. As can be seen from table 4.2 there are 4 E_{1u} modes and 3 A_{2u} modes. One each of these modes corresponds to a pure translation of the crystal leaving 3 E_{1u} and 2 A_{2u} infrared active modes.

In order to find out which ions contribute to each of the modes, a factor group analysis was carried out, grouping the ions into molecular groupings. Care must be taken in any

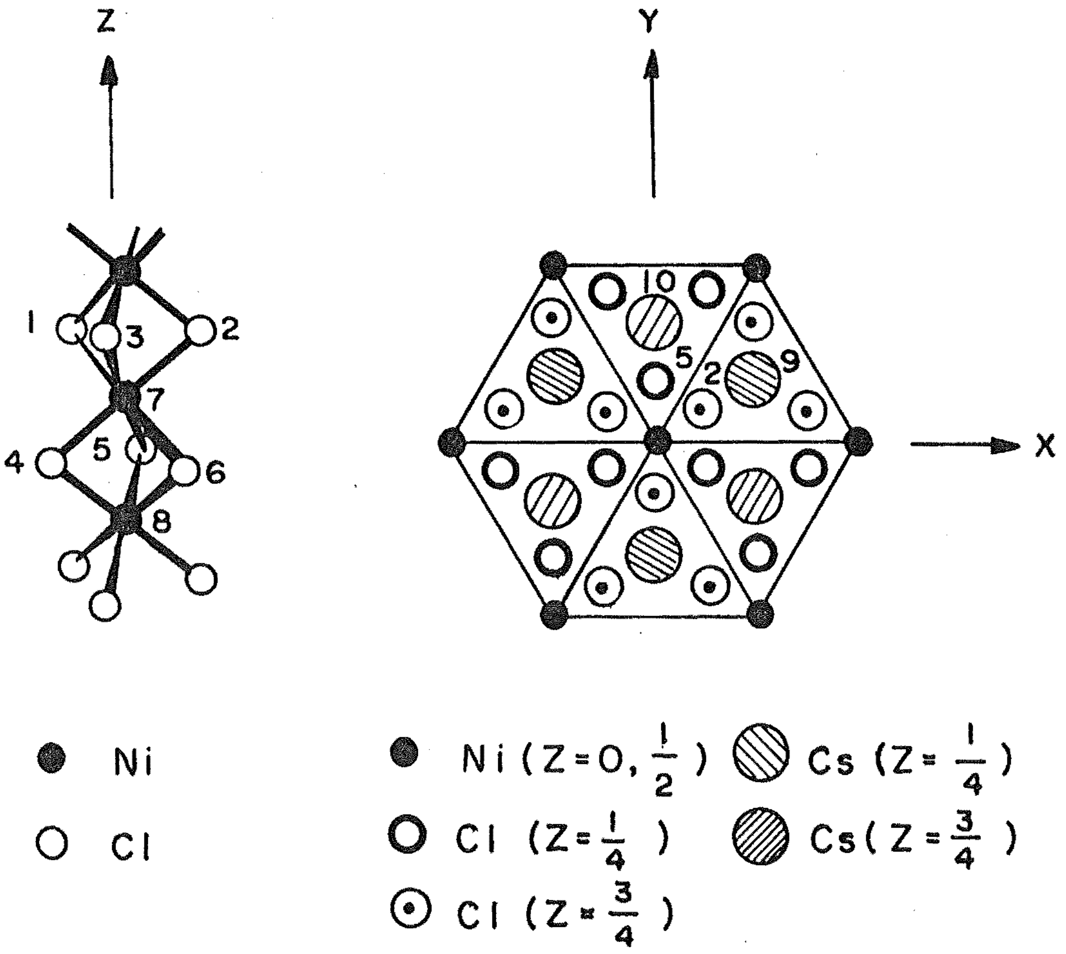

Figure 4.1 The $CsNiCl_3$-Type structure.

(from Johnstone et al 1981)

	Chlorine						Nickel		Caesium		
	1	2	3	4	5	6	7	8	9	10	$\chi(R)$
E	3	3	3	3	3	3	3	3	3	3	30
$2C_6$	0	0	0	0	0	0	0	0	0	0	0
$2C_3$	0	0	0	0	0	0	0	0	0	0	0
C_2	0	0	0	0	0	0	0	0	0	0	0
$3C_2'$	0	0	0	0	0	0	-1	-1	0	0	-6
$3C_2''$	0	0	-1	0	-1	0	0	0	-1	-1	-12
i	0	0	0	0	0	0	-3	-3	0	0	-6
$2S_3$	0	0	0	0	0	0	0	0	-2	-2	-8
$2S_6$	0	0	0	0	0	0	0	0	0	0	0
$\sigma_h(x,y)$	1	1	1	1	1	1	0	0	1	1	-8
$3\sigma_d$	0	0	0	0	0	0	0	0	0	0	0
$3\sigma_v$	0	0	1	0	1	0	1	1	1	1	18

TABLE 4.1 Reducible representation for the $CsNiCl_3$ structure (D_{6h}).

The atom numbers correspond to the numbers in figure 4.1.

Modes	Molecular groupings		
	$CsNiCl_3$	$CsNi(Cl_3)$	$Cs(NiCl_3)$
A_{1g}	1	1	1
A_{2g}	1	0	0
B_{1g}	0	0	0
B_{2g}	2	2	1
E_{1g}	1	0	0
E_{2g}	3	2	1
A_{1u}	0	0	0
A_{2u}	3	3	2
B_{1u}	2	1	1
B_{2u}	1	0	0
E_{1u}	4	3	2
E_{2u}	2	1	1

TABLE 4.2 : Number of normal modes for each molecular grouping

conclusions drawn from this method as the molecular groupings may not be unique. Tables 4.3 and 4.4 gives the reducible representations while the number of modes found for each grouping is summarized in table 4.2 and compared to the case were there are no groupings of ions.

If the chlorine ions are grouped together then there are only 2 E_{1u} and 2 A_{2u} infrared active modes indicating that one of the E_{1u} modes may involve internal motions of the chlorine ions. Taking this a step further and grouping $(NiCl_3)^-$ together then 1 E_{1u} mode and 1 A_{2u} mode remain, indicating that one mode (for each set of normal modes) may involve the internal motion of the nickel ion versus the chlorine ions. This leaves the last mode which possibly consists of motions of the caesium ion and the $(NiCl_3)^-$ molecules against each other.

The frequency of each normal mode vibration depends on the masses and force constants involved. Assuming the force constants are comparable, the lowest frequency mode is the mode involving the heaviest species of molecule, $(NiCl_3)^{1-}$. The mode with the next higher frequency is the mode involving the $(Cl_3)^{3-}$ molecule. The highest frequency mode is the mode involving internal motions of the $(Cl_3)^{3-}$.

As the modes become more "internal", a decrease in the amplitude of the motion of the "caesium" ion is expected because the mass of the "molecule" opposing the caesium ion decreases. One mode therefore should be more dependent on the changing of the caesium ion to rubidium, say, than the other two modes. A similar argument can be advanced to indicate

	Cl_3		Nickel		Caesium		
	1	4	7	8	9	10	$\chi(R)$
E	3	3	3	3	3	3	18
$2C_6$	0	0	0	0	0	0	0
$2C_3$	0	0	0	0	0	0	0
C_2	0	0	0	0	0	0	0
$3C_2'$	0	0	-1	-1	0	0	-6
$3C_2''$	-1	-1	0	0	-1	-1	-12
i	0	0	-3	-3	0	0	-6
$2S_3$	-2	-2	0	0	-2	-2	-16
$2S_6$	0	0	0	0	0	0	0
$\sigma_h(x,y)$	1	1	0	0	1	1	4
$3\sigma_d$	0	0	0	0	0	0	0
$3\sigma_v$	1	1	1	1	1	1	18

TABLE 4.3 Reducible representation for $CsNi(Cl_3)$

	$NiCl_3$		Caesium		
	1	7	9	10	$\chi(R)$
E	3	3	3	3	12
$2C_6$	0	0	0	0	0
$2C_3$	0	0	0	0	0
C_2	0	0	0	0	0
$3C'_2$	-1	-1	0	0	-6
$3C''_2$	0	0	-1	-1	-6
i	-3	-3	0	0	-6
$2S_3$	0	0	-2	-2	-8
$2S_6$	0	0	0	0	0
$\sigma_h(x,y)$	0	0	1	1	2
$3\sigma_d$	0	0	0	0	0
$3\sigma_v$	1	1	1	1	12

FIGURE 4.4 Reducible representation for $Cs(NiCl_3)$

that one mode (the mode involving internal motions between $(Cl)^{3-}$ and Ni^{2+}) would be more dependent on the replacement of the nickel ion by another transition metal ion than the other modes. All modes should be highly sensitive to the replacement of the chlorine ions.

Whether the frequency decreases or increases with the replacement of a particular ionic species within the crystal depends on the change in the lattice force constants and the mass of the replacement ion. An increase in mass will tend to decrease the frequency and a stronger force constant will tend to increase the frequency.

Symmetry co-ordinates are now calculated using projection operator techniques. Tables 4.5 and 4.6 show how a displacement by one ion maps onto other ions under the symmetry operations. These lead to the symmetry co-ordinates, for the infrared active E_{1u} and A_{2u} modes, which are given in table 4.7. These co-ordinates are consistant with those given by Johnstone et al 1981. The E_{1u} mode involves displacements in the x-y plane while the A_{2u} mode displacements are in the z direction. The normal co-ordinates, which show the actual motion of the ions, are linear combinations of the symmetry co-ordinates. This indicates that if the electric field of the input radiation in an absorption spectrum of $CsNiCl_3$ is polarized parallel (pi polarization) to the c axis of the crystal (ie the z axis) then the absorption due to two A_{2u} modes should be observed. If the radiation is polarized perpendicular to the c axis (the sigma polarization) then the absorption due to three E_{1u} modes should be observed.

E	x_3	y_3	z_3
C_6^1	$0.5x_4-0.87y_4$	$0.5y_4+0.87x_4$	z_4
C_6^5	$0.5x_6+0.87y_6$	$0.5y_6-0.87x_6$	z_6
C_3^1	$-0.5x_1-0.87y_1$	$-0.5y_1+0.87x_1$	z_1
C_3^2	$-0.5x_2+0.87y_2$	$-0.5y_2-0.87x_2$	z_2
C_2	$-x_5$	$-y_5$	z_5
$^1C_2'$	x_5	$-y_5$	$-z_5$
$^2C_2'$	$-0.5x_4+0.87y_4$	$+0.5y_4+0.87x_4$	$-z_4$
$^3C_2'$	$-0.5x_6-0.87y_6$	$+0.5y_6-0.87x_6$	$-z_6$
$^1C_2''$	$-x_3$	y_3	$-z_3$
$^2C_2''$	$+0.5x_2-0.87y_2$	$-0.5y_2-0.87x_2$	$-z_2$
$^3C_2''$	$+0.5x_1+0.87y_1$	$-0.5y_1+0.87x_1$	$-z_1$
i	$-x_5$	$-y_5$	$-z_5$
S_3^1	$-0.5x_1+0.87y_1$	$-0.5y_1+0.87x_1$	$-z_1$
S_3^2	$-0.5x_2+0.87y_2$	$-0.5y_2-0.87x_2$	$-z_2$
S_6^1	$+0.5x_4-0.87y_4$	$+0.5y_4+0.87x_4$	$-z_4$
S_3^5	$+0.5x_6+0.87y_6$	$+0.5y_6-0.87x_6$	$-z_6$
$\sigma_h(x,y)$	x_3	y_3	$-z_3$
$^1\sigma_d$	$-0.5x_4+0.87y_4$	$+0.5y_4+0.87x_4$	z_4
$^2\sigma_d$	$-0.5x_6-0.87y_6$	$+0.5y_6-0.87x_6$	z_6
$^3\sigma_d$	x_5	$-y_5$	z_5
$^1\sigma_v$	$-x_3$	y_3	z_3
$^2\sigma_v$	$+0.5x_2-0.87y_2$	$-0.5y_2-0.87x_2$	z_2
$^3\sigma_v$	$+0.5x_1+0.87y_1$	$-0.5y_1+0.87x_1$	z_1

TABLE 4.5 Mapping of the Chlorine atoms under the symmetry operations of D_{6h}.

E	x_7	z_7	x_9	z_9
C_6^1	$0.5x_8-0.87y_8$	Z_8	$0.5x_{10}-0.87y_{10}$	z_{10}
C_6^5	$0.5x_8+0.87y_8$	z_8	$0.5x_{10}+0.87y_{10}$	z_{10}
C_3^1	$-0.5x_7-0.87y_7$	z_7	$-0.5x_9\ -0.87y_9$	z_9
C_3^2	$-0.5x_7+0.87y_7$	z_7	$-0.5x_9\ +0.87y_9$	z_9
C_2	$-x_8$	z_8	$-x_{10}$	z_{10}
$^1C_2'$	x_7	$-z_7$	x_9	$-z_9$
$^2C_2'$	$-0.5x_7+0.87y_7$	$-z_7$	$-0.5x_9\ +0.87y_9$	$-z_9$
$^3C_2'$	$-0.5x_7-0.87y_7$	$-z_7$	$-0.5x_9\ -0.87y_9$	$-z_9$
$^1C_2''$	$-x_8$	$-z_8$	$-x_9$	$-z_9$
$^2C_2''$	$+0.5x_8-0.87y_8$	$-z_8$	$0.5x_9\ -0.87y_9$	$-z_9$
$^3C_2''$	$+0.5x_8+0.87y_8$	$-z_8$	$0.5x_9\ +0.87x_9$	$-z_9$
i	$-x_7$	$-z_7$	$-x_{10}$	z_{10}
S_3^1	$-0.5x_8-0.87y_8$	$-Z_8$	$-0.5x_9\ -0.87y_9$	z_9
S_3^2	$-0.5x_8+0.87y_8$	$-z_8$	$-0.5x_9\ +0.87y_9$	$-z_9$
S_6^1	$+0.5x_7-0.87y_7$	$-z_7$	$+0.5x_{10}-0.87y_{10}$	$-z_{10}$
S_6^5	$+0.5x_7+0.87y_7$	$-z_7$	$+0.5x_{10}+0.87y_{10}$	$-z_{10}$
$\sigma_h(x,y)$	x_8	$-z_8$	x_9	$-z_9$
$^1\sigma_d$	$-0.5x_7+0.87y_7$	z_7	$-0.5x_{10}+0.87y_{10}$	z_{10}
$^2\sigma_d$	$-0.5x_7-0.87y_7$	$-z_7$	$-0.5x_{10}-0.87y_{10}$	$-z_9$
$^3\sigma_d$	x_7	z_7	x_{10}	z_{10}
$^1\sigma_v$	$-x_7$	z_7	x_9	z_9
$^2\sigma_v$	$+0.5x_7-0.87y_7$	z_7	$0.5x_9\ -0.87y_9$	z_9
$^3\sigma_v$	$+0.5x_7+0.87y_7$	z_7	$0.5x_9\ +0.87x_9$	z_9

TABLE 4.6 Mapping of the Caesium and Nickel atoms under the symmetry operations of D_{6h}.

Mode	Symmetry co-ordinates
E_{1u}	$4a_1(x_3+x_5) + (a_1+3a_2)(x_1+x_2+x_4+x_6)$ $+\sqrt{3}(a_1-a_2)(y_1-y_2-y_4+y_6) + a_3(x_7+x_8) + a_4(x_9+x_{10})$ $4a_1(y_3+y_5) + (a_1+3a_2)(y_1+y_2+y_4+y_6)$ $+\sqrt{3}(a_2-a_1)(x_1-x_2-x_4+x_6) + a_3(y_7+y_8) + a_4(y_9+y_{10})$
A_{2u}	$c_1(z_1+z_2+z_3+z_4+z_5+z_6) + c_2(z_7+z_8) + c_3(z_9+z_{10})$

TABLE 4.7 : Symmetry co-ordinates for the E_{1u} and A_{2u} modes.

Note : The constants a_1, a_2, a_3 etc. are dependent on the actual force constants and ions involved in each mode.

The symmetry co-ordinates also support the ideas outlined above for the possibility of the molecular groupings playing an important role in the normal mode motions. In particular they show that the "internal" motion of the chlorine ions are in the x-y plane and not in the z direction.

4.6 FAR INFRARED SPECTRA OF $CSNICL_3$ TYPE CRYSTALS

Typical polarized single crystal spectrum of phonons in $CsNiCl_3$ type crystals are shown in figure 4.2. The sample is less than 0.1mm thick which is typical for the phonon work. This spectra, of $CsNiBr_3$, shows clearly the absorption due to the three modes in the sigma polarization and the two in the pi polarization. The frequency of the transverse optical modes are at the point of maximum absorption. Where the maximum absorption is a flat region of zero transmission the transverse mode frequency is near the low frequency edge of the absorption (see chapter 3). In the pi polarized spectrum absorption lines also occur at the longitudinal mode frequencies of the transverse modes seen in the sigma polarization spectra. These longitudinal mode frequencies tend to be at the high frequency edge of the broad absorptions in the sigma polarization spectra.

The hardest phonon mode line position to estimate is the highest frequency line of the pi polarization. In many spectra a reliable estimate of the position could not be given.

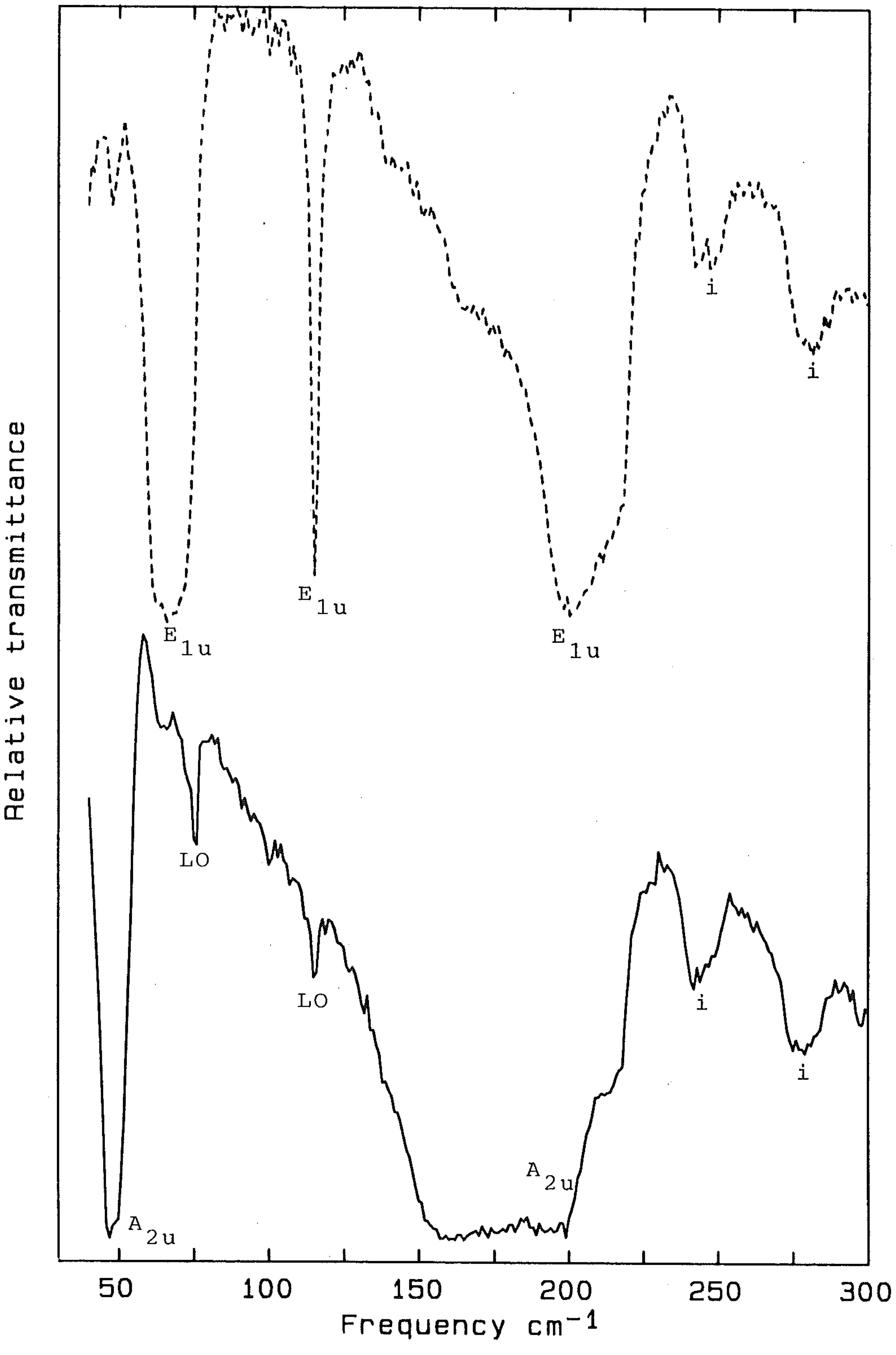

Figure 4.2 The polarization spectra for $CsNiBr_3$ at 1.5K. These are typical phonon spectra for the $CsNiCl_3$ type crystals showing all 3 E_{1u}(TO) and 2 A_{1u}(TO) modes. Various associated LO modes and unpolarized absorptions (i) probably due to water vapour attack of the surface are also prominent.

------ σ polarization ———— π polarization

The two unpolarized absorption lines above 230 wavenumbers are possibly due to the attack of water on the hygroscopic crystal surface. In other crystals water lines often appeared between the lowest two phonon absorption lines in the sigma polarization. The water attack lines can be identified because their absorption strength does not depend on the crystal thickness. Also these lines are often unpolarized.

Table 4.8 gives the frequencies of the transverse optical modes for thirteen of the $CsNiCl_3$ type crystals. Where a pi spectrum absorption is determined to be a longitudinal optical mode frequency this frequency is given in table 4.9.

The only way of assigning the five transverse optic phonon lines to particular motions of the ions in a crystal is to examine the shift in line positions when a particular species of ion is replaced by another.

Figures 4.3 and 4.4 show the effect of exchanging chlorine for bromine in $CsNiX_3$. The largest shift in line frequency is in the relatively sharp middle line of the sigma polarization. This is identified with a mode consisting of mainly "internal" motions of the halide ion. Firstly the "internal" halide ion mode is predicted to appear only in the sigma polarization. The lower frequency absorption line in each polarization are of similar shape and width as are each of the two highest absorption lines in each polarization. The "odd man out" then is the narrow middle line in the sigma polarization. Secondly the ratio of the

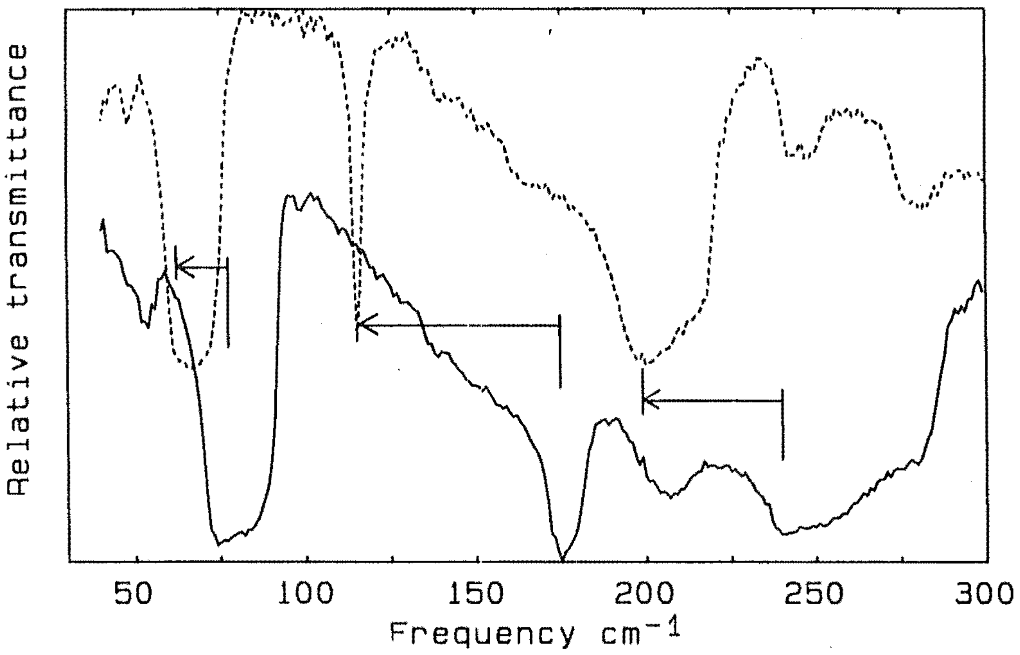

(a) S polarized

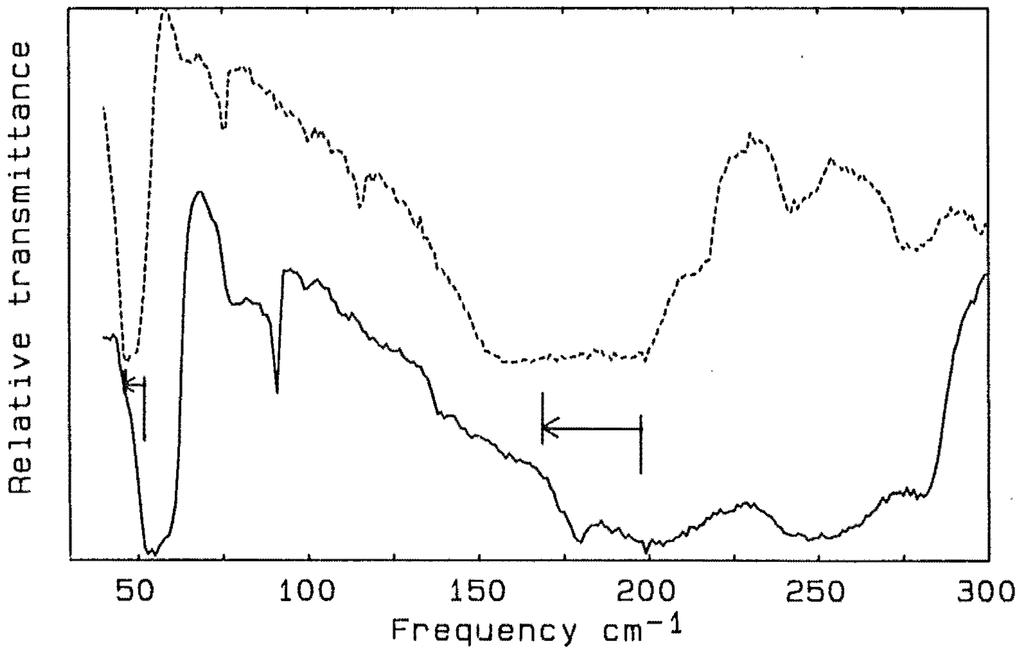

(b) P polarized

Figure 4.3 The effect on the phonon spectra of altering the X ion in $CsNiX_3$

—— $CsNiCl_3$ ---- $CsNiBr_3$ ⟵| line shift : Cl to Br

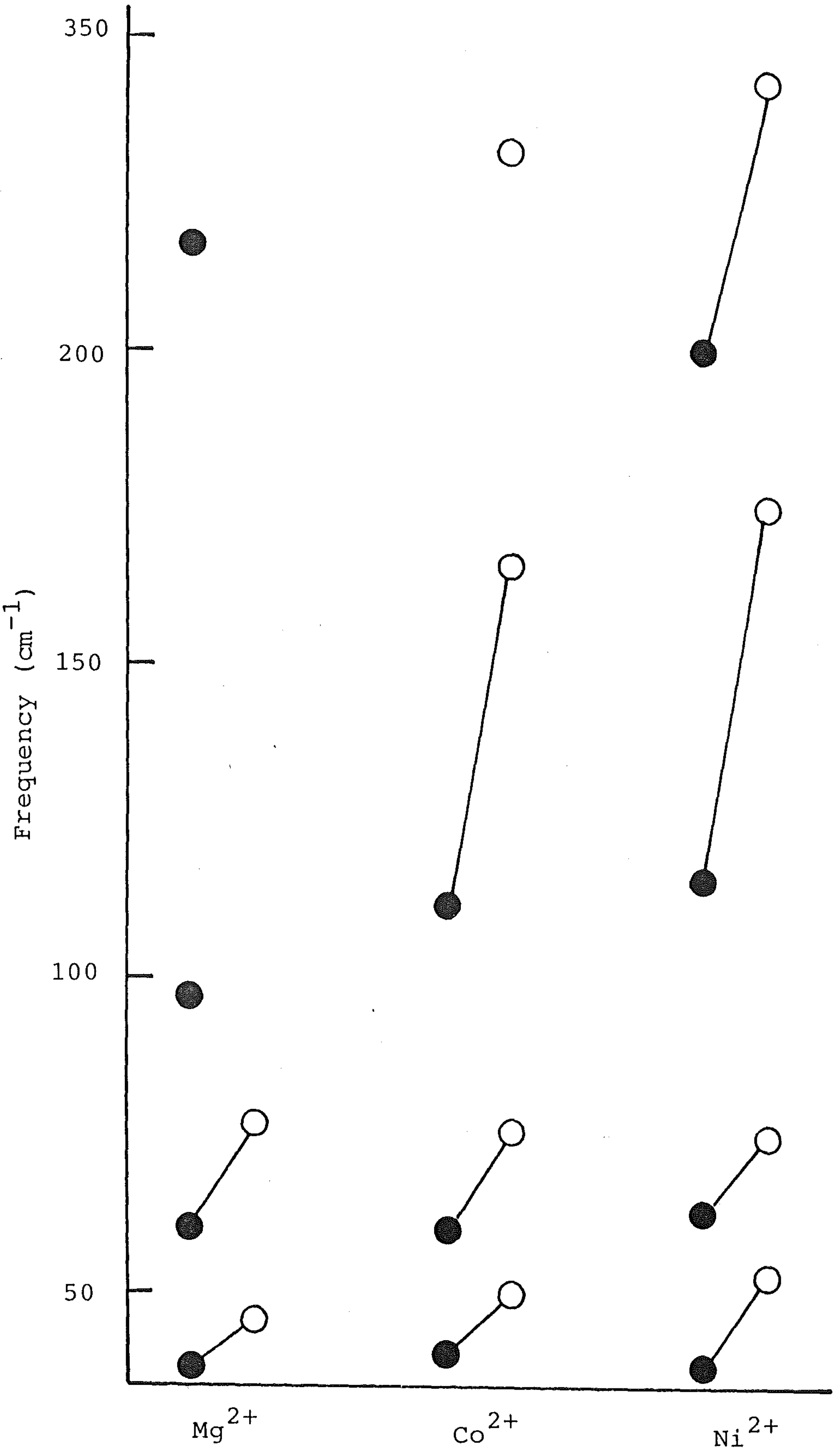

FIGURE 4.4 The effect on the phonon spectra of replacing the X$^-$ ion in CsMX$_3$ crystals. The highest A_{2u} mode has not been plotted because of its large uncertainties

● Br$^-$ ○ Cl$^-$

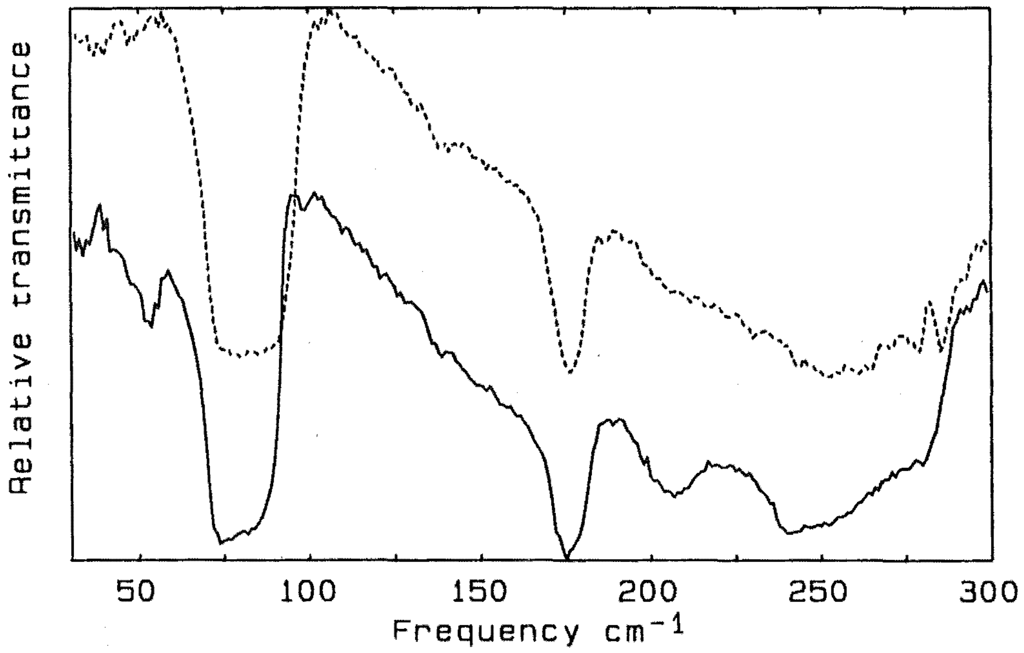

(a) S polarized

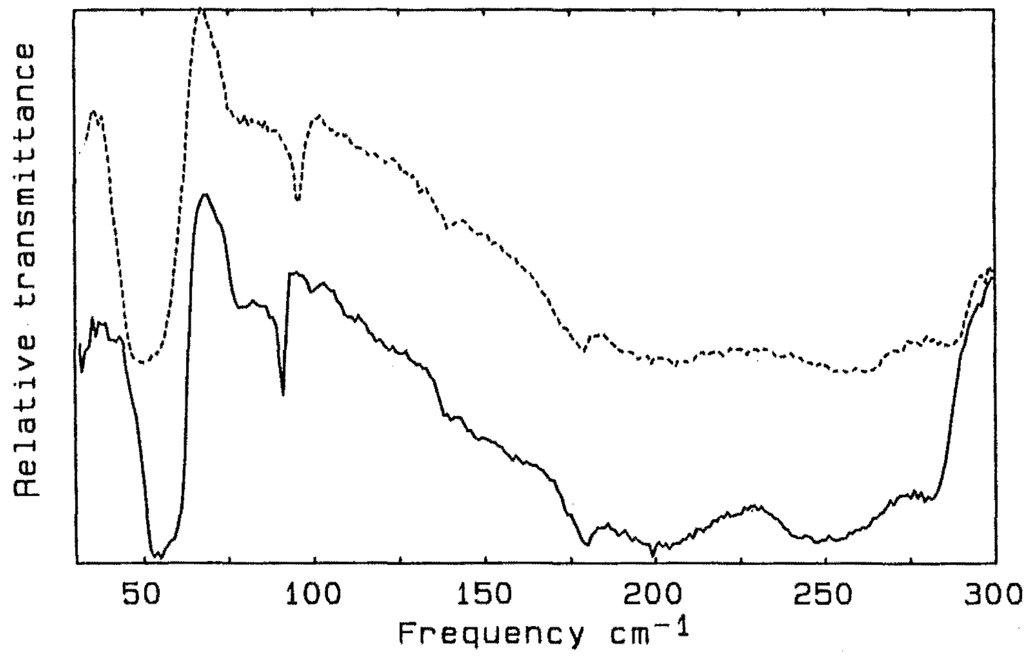

(b) P polarized

Figure 4.5 A comparison of the spectra of $CsNiCl_3$ (——) and $RbNiCl_3$ (---) at 1.7K.

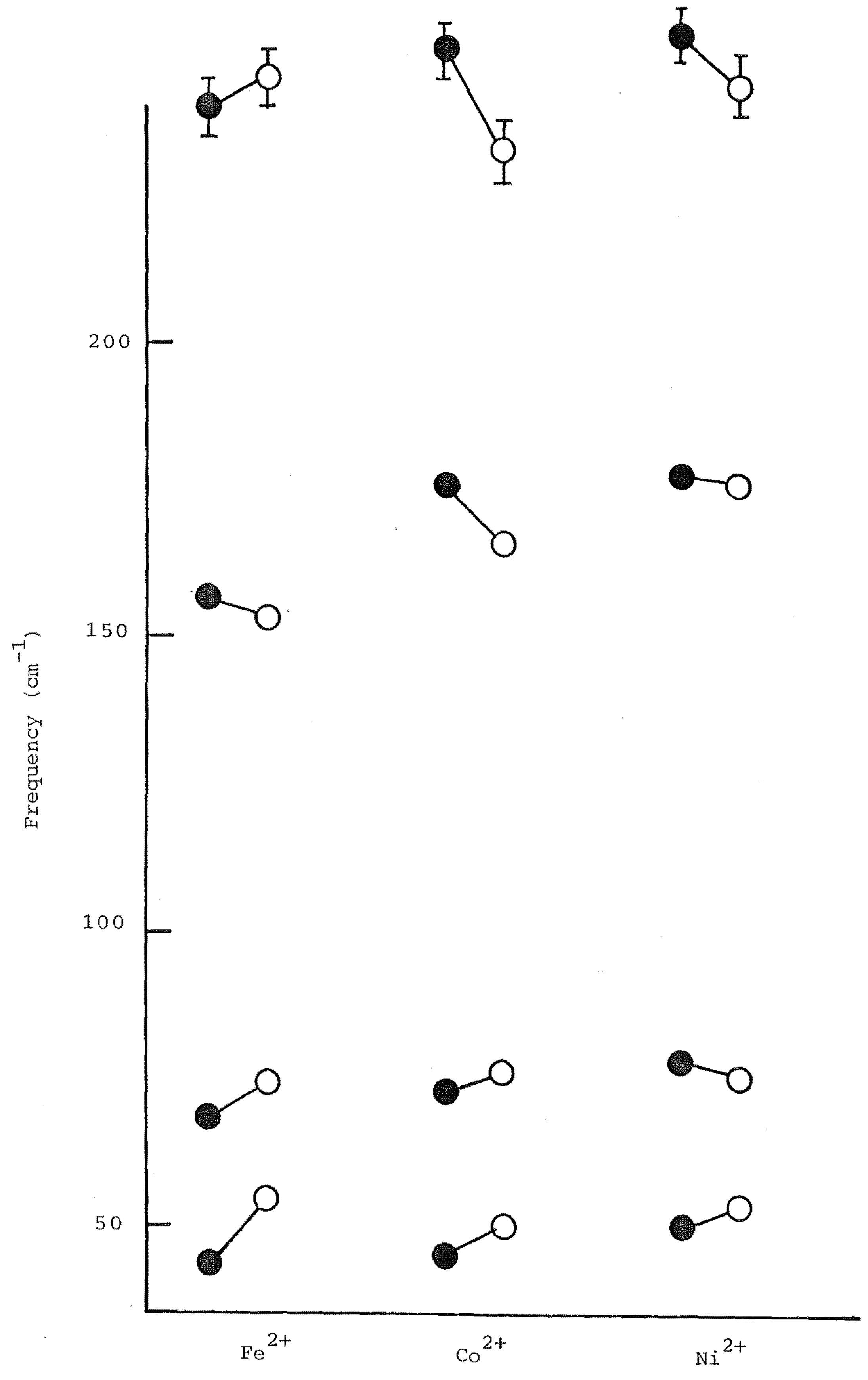

Figure 4.6 The effect on the phonon spectra of replacing the A$^+$ ion in AMCl$_3$ crystals.

● Rb$^+$ ○ Cs$^+$

inverse square root of the masses of the chlorine and bromine ions is almost exactly the same as the ratio of the frequency shift for the middle line (table 4.10). If there is no force constant change between these compounds this is what would be expected for a mode consisting mainly of internal motions of the halide ion.

The frequency of the "internal" halide mode being the middle of the three sigma polarization modes is not what was expected from consideration of the masses of the "molecules" involved in each mode. This points to the force constants involved in the "internal" motion of the halides being quite weak compared to the forces involved in the other modes.

The effect on the mode frequencies of altering the monovalent alkali metal ion is illustrated in figure 4.5 which compares the spectra of $CsNiCl_3$ and $RbNiCl_3$. Figure 4.6 illustrates the frequency changes for the chlorine compounds. These figures show that altering the monovalent ion has little effect on the frequencies. There may be a small effect on the lower two absorption lines. The only conclusion that can be drawn from this is that any decrease in the mass change when replacing rubidium with caesium is offset by a compensating change in the force constants involved.

The effect of altering the transition metal ion is demonstrated in figure 4.7 which shows the differences between the spectra of $CsNiCl_3$ and $CsCoCl_3$. The frequency changes are illustrated in figures 4.8 and 4.9. These show that the frequency of the modes generally increase as the transition metal mass is increased. Hence for the transition

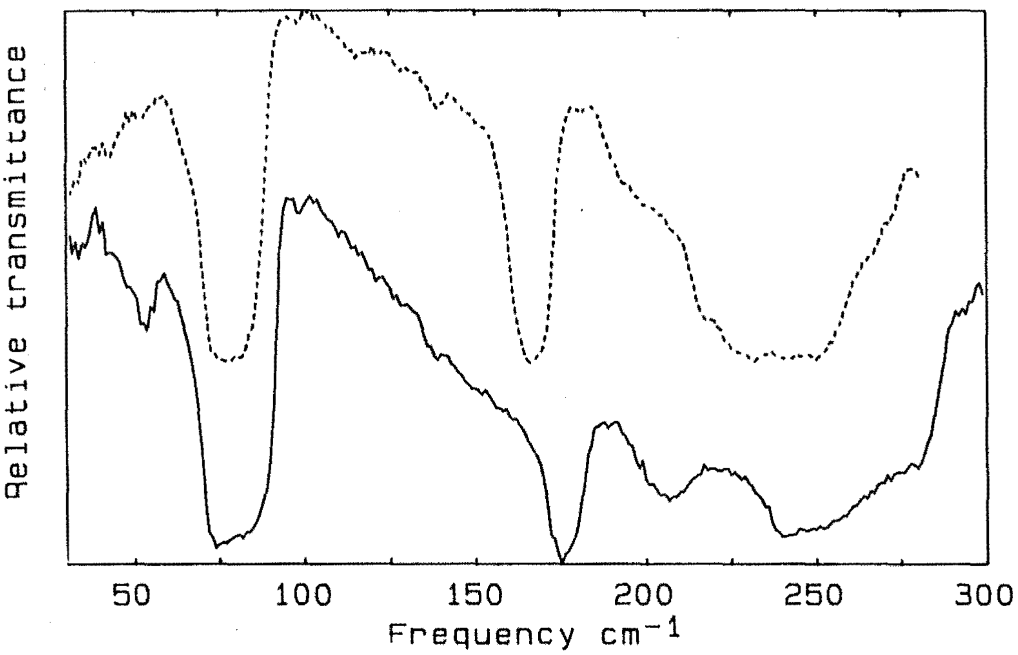

(a) S polarized

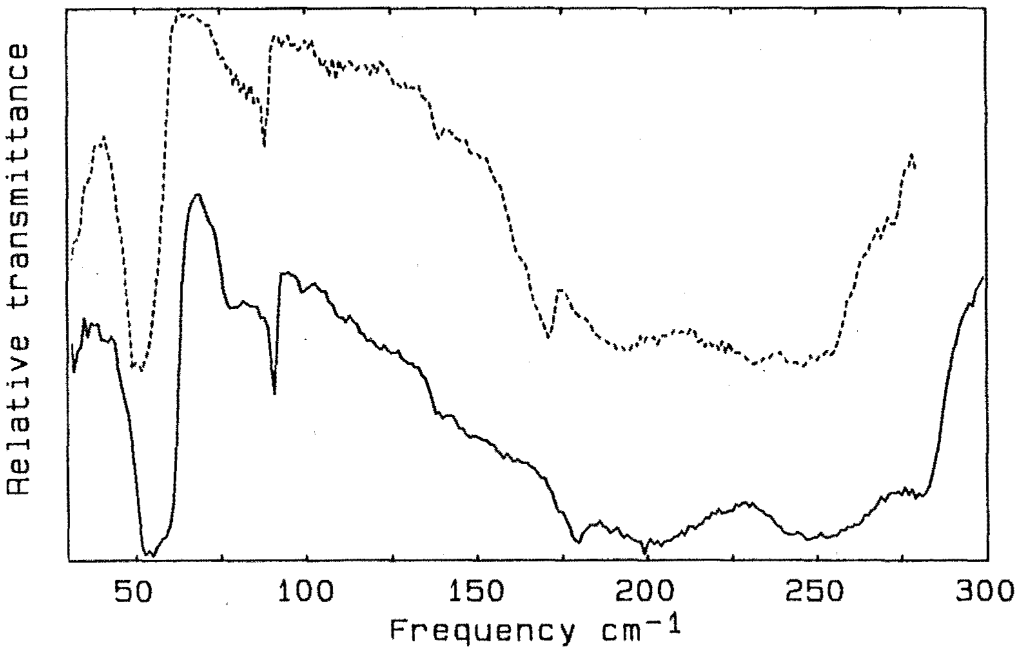

(b) P polarized

Figure 4.7 A comparison of the spectra of $CsNiCl_3$ (——) and $CsCoCl_3$ (---) at 1.7K.

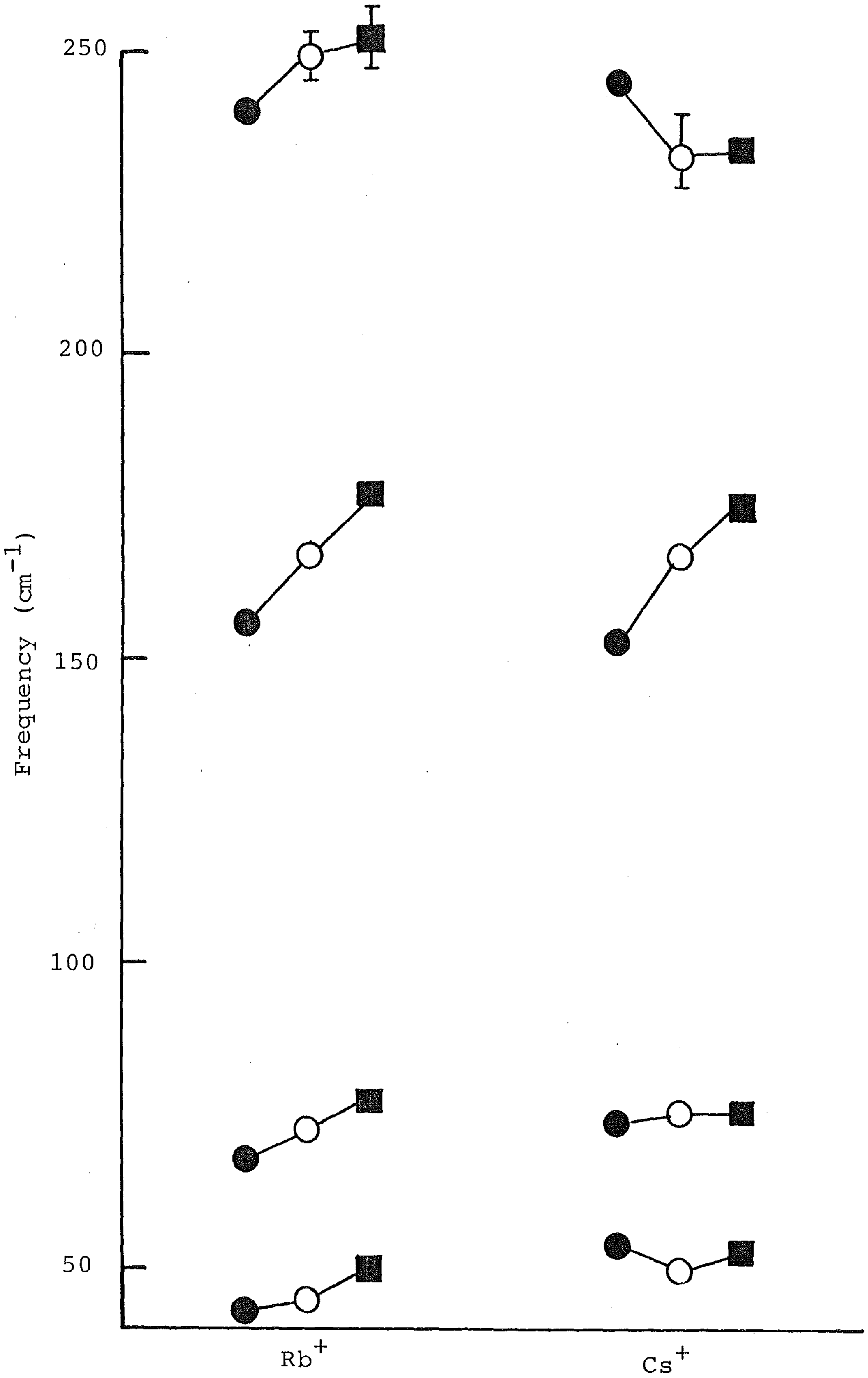

FIGURE 4.8 The effect on the phonon spectra of replacing the M^{2+} ion in $AMCl_3$. The uncertainties are contained within the symbol unless shown otherwise.

● Fe^{2+} ○ Co^{2+} ■ Ni^{2+}

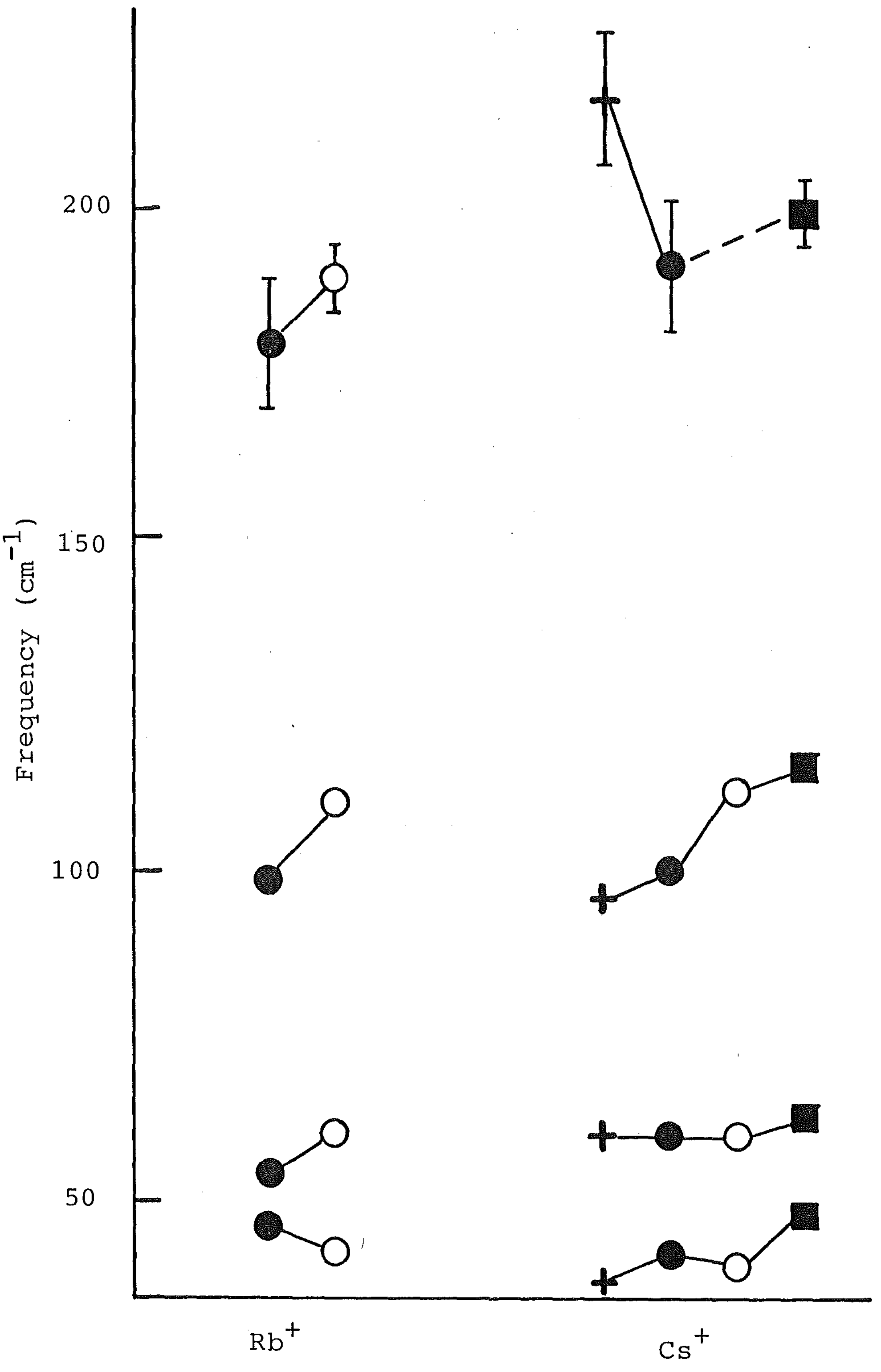

FIGURE 4.9 The effect on the phonon spectra of replacing the M^{2+} ion in AMBr$_3$. The uncertainties are contained in the symbols unless shown otherwise.

✚ Mg^{2+} ● Mn^{2+} ○ Co^{2+} ■ Ni^{2+}

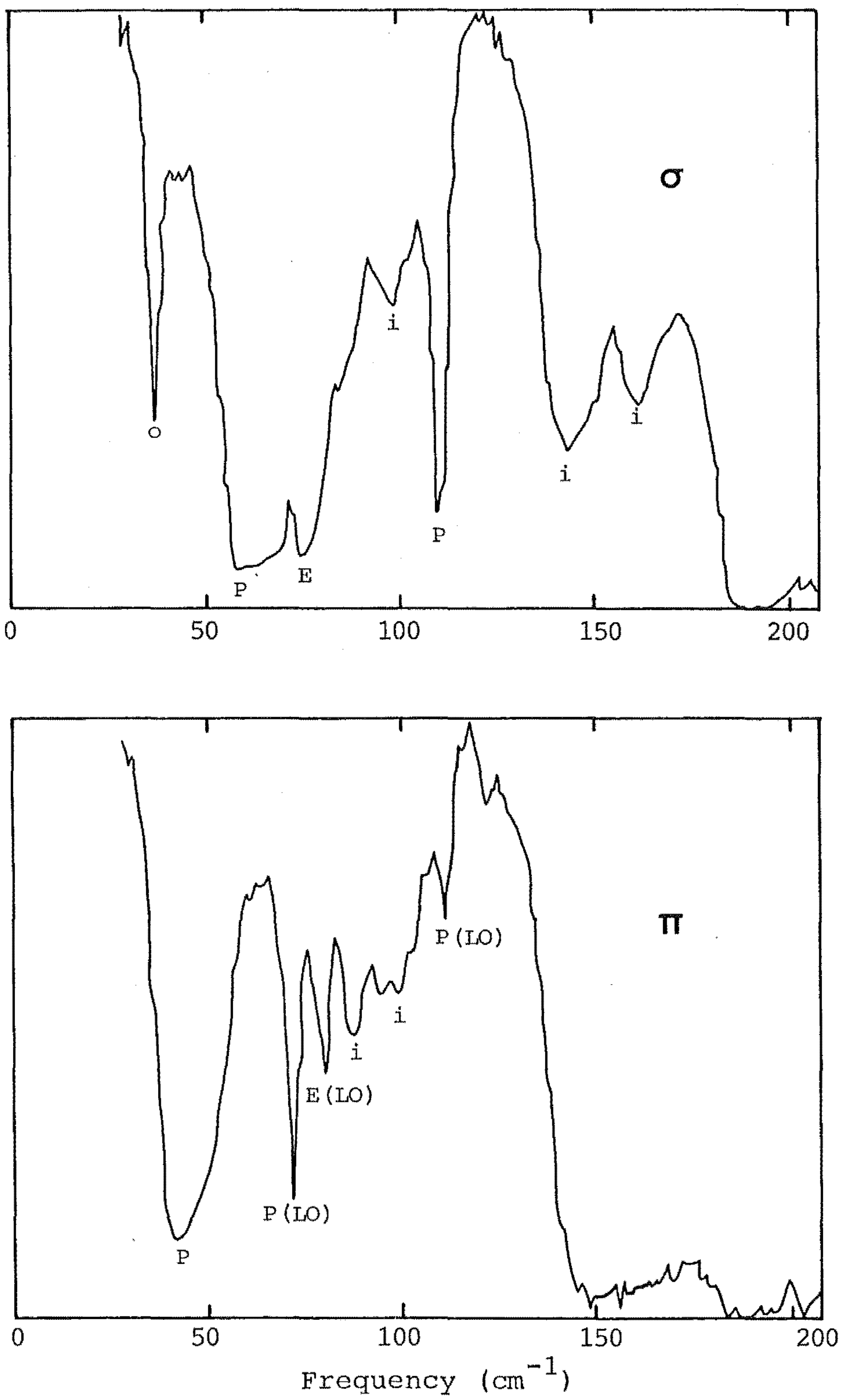

Figure 4.10 Polarized spectra of $RbCoBr_3$ at 1.7 K. Sample thickness 0.08 mm. E and O are extra "phonon" lines seen only in $RbCoBr_3$ and $RbMnBr_3$. i are unknown impurity lines.

	E_{1u}			A_{2u}	
$RbFeCl_3$	68^{+3}_{-1}	156^{+2}_{-1}	240^{+5}_{-1}	43^{+3}_{-1}	176*
$RbCoCl_3$	73^{+2}_{-2}	176^{+2}_{-1}	250^{+5}_{-5}	45^{+2}_{-2}	180*
$RbNiCl_3$	78^{+3}_{-3}	177^{+2}_{-2}	252^{+5}_{-5}	50^{+2}_{-2}	207*
$RbMnBr_3$	54^{+3}_{-3}	99^{+1}_{-1}	180^{+10}_{-10}	46^{+3}_{-1}	144*
$RbCoBr_3$	60^{+5}_{-1}	110^{+1}_{-1}	190^{+5}_{-5}	42^{+2}_{-1}	160*
$CsMgCl_3$	77^{+2}_{-1}	-	-	46^{+1}_{-1}	-
$CsFeCl_3$	74^{+2}_{-1}	153^{+3}_{-1}	245^{+5}_{-5}	54^{+2}_{-2}	190*
$CsCoCl_3$	76^{+2}_{-2}	167^{+2}_{-2}	233^{+7}_{-5}	50^{+2}_{-1}	195*
$CsNiCl_3$	75^{+3}_{-1}	176^{+1}_{-1}	244^{+5}_{-2}	53^{+1}_{-1}	200*
$CsMgBr_3$	60^{+1}_{-1}	96^{+5}_{-5}	217^{+10}_{-10}	38^{+1}_{-1}	142*
$CsMnBr_3$	60^{+2}_{-1}	100^{+1}_{-1}	192^{+10}_{-10}	42^{+2}_{-2}	150*
$CsCoBr_3$	60^{+5}_{-2}	112^{+2}_{-1}	-	40^{+5}_{-5}	-
$CsNiBr_3$	63^{+3}_{-1}	116^{+1}_{-1}	200^{+5}_{-5}	48^{+1}_{-1}	170*

frequencies listed in cm^{-1}

* the uncertainty in these line positions is ±20 cm^{-1}

TABLE 4.8 Transverse Optic Phonons in $CsNiCl_3$-Type Crystals

	TO	LO	$\frac{\nu_{LO}}{\nu_{TO}}$	TO	LO	$\frac{\nu_{LO}}{\nu_{TO}}$
$RbFeCl_3$	68	91	1.34	156	-	-
$RbCoCl_3$	73	93	1.27	167	-	-
$RbNiCl_3$	78	97	1.24	177	180	1.02
$RbMnBr_3$	54	-	-	99	-	-
$RbCoBr_3$	60	72	1.2	110	111	1.01
$CsMgCl_3$	77	98	1.27	-	-	-
$CsFeCl_3$	74	87	1.18	153	-	-
$CsCoCl_3$	76	89	1.17	167	172	1.03
$CsNiCl_3$	75	92	1.23	176	181	1.03
$CsMgBr_3$	60	77	1.28	96	-	-
$CsMnBr_3$	60	69	1.15	100	102	1.02
$CsCoBr_3$	60	75	1.25	112	-	-
$CsNiBr_3$	63	76	1.21	116	117	1.01

TABLE 4.9 Frequencies (in cm^{-1}) of the LO Modes in $CsNiCl_3$-Type Crystals at 1.7K. The uncertainties are typically ±2 cm^{-1}.

metal ion the force constant change plays a more important role in the change of frequency than the mass change. The mode which has the least relative change is the highest frequency one which either indicates that the force constant change is the least for this mode or conversely the force constant change is counteracted by the mass change.

In summary all the 5 absorption lines of the phonon modes in $CsNiCl_3$ type crystals have been observed. The lowest frequency absorption line in each polarization is attributed mainly to motions of the "$(NiCl_3)^-$" and the "Cs^+" ion, on the basis of the heavy ions involved. The middle frequency absorption line of the sigma polarization involves the "internal" motion of the halide ions. This assignment is given because it is the "odd man out" of the modes and because of its strong dependence on the mass of the halide ion. The highest frequency absorption line in each polarization is attributed to mainly motions of the transition metal ion versus the halide ions moving together on the basis of the lighter masses involved (compared to the lowest frequency mode). Table 4.11 summarizes these assignments.

4.7 EXTRA "PHONON" LINES IN $RBCOBR_3$ AND $RBMNBR_3$

In thin crystals (0.1mm thick) of $RbCoBr_3$ and $CsMnBr_3$ two extra lines are present which do not seem to be due to water attack (figure 4.10). The first line is strongly absorbing and is very close to, and in thicker crystals merges with, the lowest mode in the sigma polarization. In

$$\frac{\text{Frequency - Br crystal}}{\text{Frequency - Cl crystal}}$$

	E_{1u}			A_{2u}	
	1	2	3	1	2
$CsNiX_3$	0.84	0.66	0.82	0.91	-
$CsCoX_3$	0.79	0.67	-	0.80	-
$RbCoX_3$	0.82	0.66	0.82	0.93	-

$$\text{c.f.} \sqrt{\frac{M_{Cl}}{M_{Br}}} = 0.666$$

Table 4.10 Ratio of observed phonon frequencies when Cl is replaced by Br in AMX_3

the pi polarization there is an absorption line which could be at the longitudinal optical mode frequency of this extra line. The second line is sharper and appears in the sigma polarization at about 40cm^{-1} in both crystals. The presence of these phonon like lines raises the possibility that $RbCoBr_3$ and $RbMnBr_3$ have a slightly different structure to $CsNiCl_3$. This may indicate that the x-ray crystallographic data for these two compounds should be re-examined.

Frequency	Polarization	Mode	"Molecule" involved
"high"	σ π	E_{1u} A_{2u}	Cs^+, Ni^{2+} vs $(Cl_3)^{3-}$
"medium"	σ	E_{1u}	$(Cl_3)^{3-}$ internal
"low"	σ π	E_{1u} A_{2u}	Cs^+ vs $(NiCl_3)^-$

Table 4.11 Assignment of the lattice modes observed for $CsNiCl_3$-Type crystals.

CHAPTER 5

MAGNONS IN $RbCoBr_3$

5.1 INTRODUCTION

Magnetic excitations in $ACoX_3$ type crystals have been extensively studied because of the simplicity of the theory involved in their one-dimensional antiferromagnetic nature.

Magnons have been reported in $CsCoBr_3$ by Johnstone et al (1980a,1980b) and by Lehmann (1981) using Raman spectroscopy and in $CsCoCl_3$ by Lehmann et al (1981) using Raman spectroscopy, by Brun et al (1980) using far infrared absorption and by Breitling et al (1977) using a magnetic field to sweep the magnon line through far infrared laser lines. More recently, magnetic excitations in $RbCoCl_3$ have been studied by Lockwood et al (1983) using Raman scattering and Jorke and Durr (1983) using far infrared absorption and far infrared laser resonance.

Theoretical work has been presented by Shiba (1980) and extended by Nagler et al (1983) , Johnstone et al (1980b) and Lehmann et al (1981).

So far no studies have been made of the magnetic excitations in the only other cobalt compound isostructural to the above, ie $RbCoBr_3$. This may be due to the difficulty of growing $RbCoBr_3$.

$RbCoBr_3$ has been reported as having the same magnetic structure as $CsCoCl_3$ (Melamud et al. 1974) and so the magnon spectra may well be expected to be similar to $CsCoCl_3$.

Part 5.2 of this chapter outlines the theory of magnons in quasi-one-dimensional antiferromagnets. The results of far infrared absorption and Zeeman studies of $RbCoBr_3$ and their comparison with $CsCoCl_3$ is given in section 5.3. Part 5.4 reports the observation of a possible antiresonance line in $RbCoBr_3$ and section 5.5 outlines preliminary work in the search for magnons in other $CsNiCl_3$ type crystals.

5.2 THEORY OF MAGNONS IN $ACoX_3$ TYPE ANTIFERROMAGNETS

The cobalt ions in $ACoX_3$ type crystals are in linear chains well separated by A^+ ions with the magnetic moments of the cobalt ions parallel to the chain direction. It is not surprising therefore that the magnetic interactions within the crystal are dominated by this linear chain. The magnetic excitations of one chain can be described by the effective spin 1/2 Ising antiferromagnetic Hamiltonian (Jorke and Durr 1983)

$$H_o = 2J\ \Sigma_j (S^z_j S^z_{j+1} + \varepsilon(S^x_j S^x_{j+1} + S^y_j S^y_{j+1})) + \Sigma_j g\mu_b B_o S^z_j$$

where there is an external magnetic field (B_o) parallel to the c (=z) axis.

Here J is the longitudinal intrachain exchange interaction strength.

ε is the relative intrachain transverse interaction strength

There are two limits to the Hamiltonian. $\varepsilon=1$ gives the totally isotropic Heisenberg model. $\varepsilon=0$ gives the 1-dimensional (linear chain) Ising model.

For the Ising model the first excited state is highly degenerate at $\nu= 2J$ for an infinitely long chain of atoms. However for a perturbation on the Ising model ε, is small and non-zero. In this case the degeneracy is lifted and the first excited state is a continuum from $2J(1-2\varepsilon)$ to $2J(1+2\varepsilon)$ for zero wavevector ($K=0$).

Below a transition temperature T_{N1} (the first Neel temperature), the relatively weak interchain interactions must be taken into account. This is done by adding to the above Hamiltonian the perturbing term

$$H' = -\Sigma_j (-1)^j h$$

which is valid provided the molecular field (h) and εJ are much smaller than J (Shiba 1980). This is called the molecular field approximation where only the interchain longitudinal antiferromagnetic exchange interaction (J') is considered (Jorke and Durr). The addition of this term quantizes the excitation continuum into a series of discrete levels.

Depending on the magnetic state of the nearest neighbour cobalt chains, several sets of these levels can be expected. For example if all the six nearest neighbour magnetic ions are antiparallel then the molecular field ,h, is $6J'$ giving one set of energy levels. If 4 of the nearest neighbour chain ions are antiparallel and 2 are parallel then the molecular field is $2J'$.

Two different three-dimensional magnetic phases have been observed in the $ACoX_3$ compounds (Shiba 1980).

The first, for temperatures below T_{N1}, has two thirds of the chains antiferromagnetically aligned (the α and β chains) and the other third (γ) disordered (figure 5.1a). The γ chains always experience zero net molecular field from the surrounding chains. For the α and β chains 3 antiferromagnetic surrounding chains give a field 3J'. The other 3 surrounding chains can contribute +J' or -J' each to the field. There are 8 possible combinations of the three disordered chains (+++, ++-, +-+, -++, +--, -+-, --+ and ---). So for 1/8 th of the α and β sites these chains contribute 3J' giving a total field of 6J', for 3/8th of the sites they contribute 1J' giving a total field of 4J', for 3/8th of the sites they contribute -1J' giving a total field of 2J' and the last 1/8th contribute -3J' to give a total field of 0J'. The probabilities for each contribution to the field are then 1/12th for 6J' (2/3rds of the chains α and β) for 1/8th of the sites) 1/4 for 4J' (2/3rds of the chains for 3/8th of the sites), 1/4 for 2J' (2/3rds of the chains for 3/8th of the sites) and 5/12th for 0J' (1/3rd of the chains (γ) for all sites and 2/3rds of the chains 1/8th of the sites) giving 3 sets of lines (called the A, B_1 and B_2 lines for 6J', 4J' and 2J') and a continuum for 0J'.

The second magnetic phase of $ACoX_3$ compounds occurs for temperatures lower than T_{N2}. In this phase, next nearest neighbours have the same spin direction (figure 5.1b). In this case 1/3rd of the chains experience a net interchain

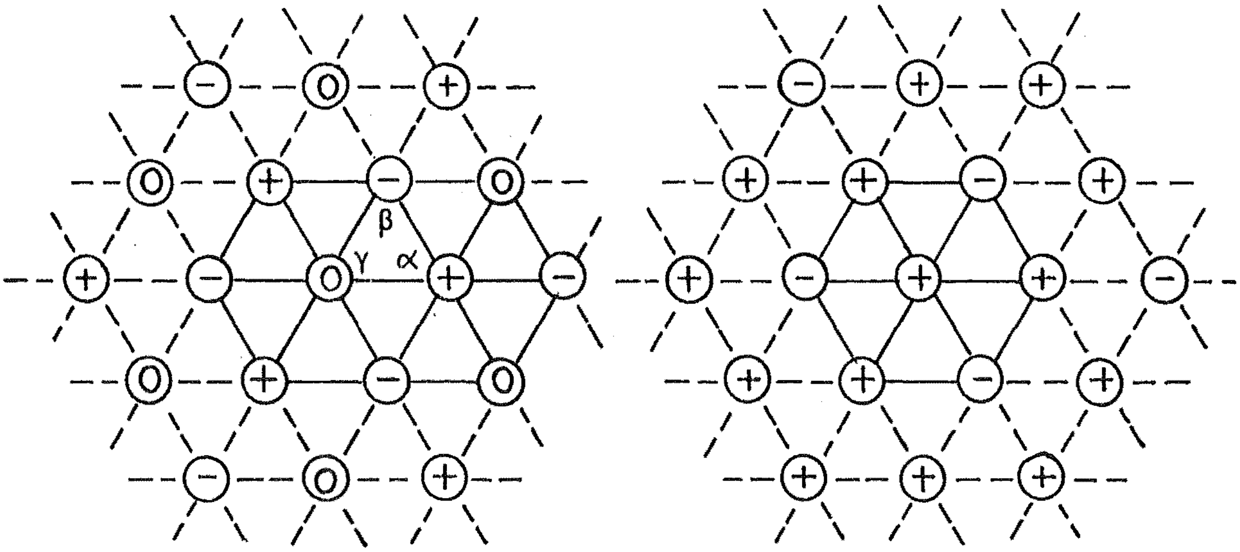

(a) $T_{N2} < T < T_{N1}$

(b) $T < T_{N2}$

Figure 5.1 The ordered structures for $RbCoBr_3$ in the ab plane. Only the Co^{2+} chains are shown with their spin direction marked by up(+), down (-) or random (0).

field of 0J' and 2/3rds have a field 6J'. These give rise to the continuum and the A series of discrete lines respectively.

At the Brillouin zone centre (K=0) the frequency of the lines in the magnon spectra can be calculated from the tridiagonal matrix (Johnstone et al. 1980b)

$$\begin{aligned}\langle\psi_{2i-1}|H/2J|\psi_{2i'-1}\rangle &= \{1+\frac{3}{2}\varepsilon^2-\frac{\varepsilon^2}{2}\delta_{i,1}+(2i-1)\frac{h}{J}\} \text{ for } i=i' \\ &= \varepsilon \text{ for } i=i'\pm 1 \\ &= 0 \text{ elsewhere}\end{aligned}$$

The eigenvalues of this matrix are the quantum energies of the magnons in units of 1/2J. The values of J, ε, and h for the appropriate material can therefore be determined by comparing the experimentally determined magnon frequencies with the eigenvalues of the above matrix.

5.3 RESULTS

In magnon studies using far infrared spectroscopy it is necessary to optimize the thickness of the sample. On the one hand this must be thin enough to permit general transmission in the region of interest (which also includes absorption by lattice phonons) and on the other hand must be thick enough so that any discrete magnon absorption lines show above the background noise level of the signal. For $RbCoBr_3$ at 1.7K, a 1mm thickness was found to be optimum.

The far infrared pi polarized spectra for $CsCoCl_3$ is shown in figure 5.2a. The lower frequency edge of the continuum absorption can be easily seen at 82cm-1. Some 15 discrete magnon lines are observed within the range 80 to 140 cm^{-1}. These are listed in table 5.1 and agree with the values reported previously by Lehmann et al. (1981). The magnon line widths are typically less than $0.5cm^{-1}$. The magnon at $89cm^{-1}$ coincides with the frequency of a longitudinal optic mode of a phonon which raises the possibility of a phonon-magnon interaction.

The transition temperature to the fully ordered phase (T_{N2}) in $CsCoCl_3$ is approximately 9 Kelvin (Melamud et al. (1974). Below this temperature the A series of lines should have the strongest absorption intensity. This is not the case for the $CsCoCl_3$ far infrared spectrum presented here. All the magnon lines seem to be of similar intensity. This is in contrast to the Raman results of Lehmann et al. (1981) where the A series dominates the 2K spectra but all series have approximately equal strengths in the 10K spectra.

Temperature dependent studies need to be carried out on $CsCoCl_3$ to determine whether the B_1 and B_2 series of lines become stronger above the lower transition temperature of 9 Kelvin (i.e T_{N2}).

The far infrared spectrum for $RbCoBr_3$, in contrast to $CsCoCl_3$, has only two magnetically dependent lines (magnons) observable below 140 cm^{-1} (figure 5.2b) Their widths (aproximately 3 cm^{-1}) are considerably more than the magnon lines in $CsCoCl_3$. The low frequency edge of the continuum absorption for $RbCoBr_3$ is hard to positively identify because of the proximity of the strongly absorbing phonon at 160 cm^{-1} although it may tentatively be given as 89 cm^{-1}.

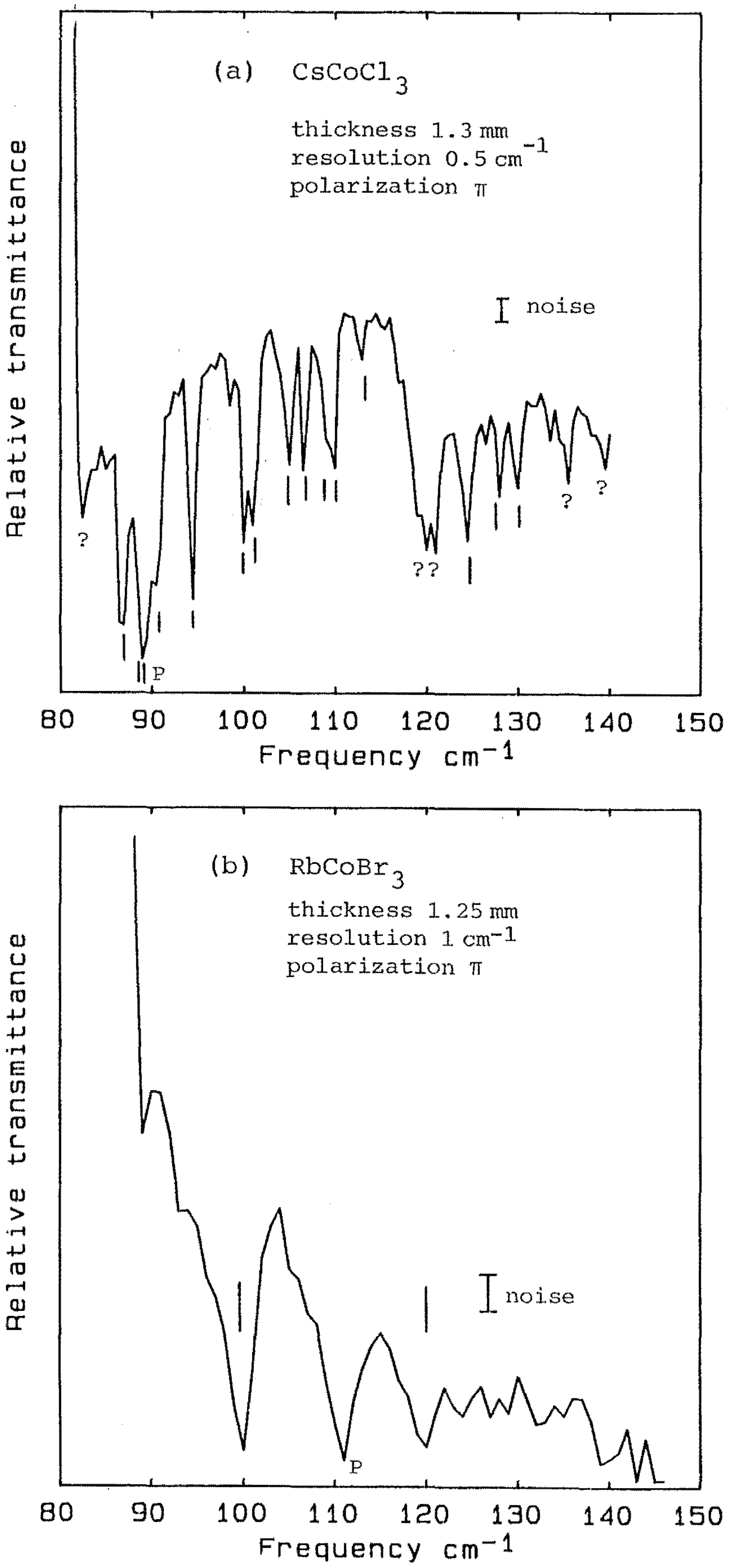

Figure 5.2 A comparison of the magnon spectra of $CsCoCl_3$ and $RbCoBr_3$ at 1.7 Kelvin.

P phonon | magnon ? not known

CsCoCl$_3$	RbCoBr$_3$	
	Experimental	Calculated
82.5 +	100	100.0
86.5	120	119.7
87.0	---	134.7
89.0	---	147.6
90.5 *		
94.5		
98.5		
100.0		
101.0		
105.0		
106.5 *		
110.0		
113.0		
120.0 +		
121.0		
124.5		
128.0 *		
130.0		
133.5 +		
135.5 +		
139.5 +		

Table 5.1 Observed magnon line frequencies for CsCoCl$_3$ and RbCoBr$_3$.

* The A series of lines as assigned by Lehmann et al. (1981).

+ Possible magnon lines not seen by other workers.

The first lower energy magnon at $100cm^{-1}\pm 0.5\ cm^{-1}$ is the stronger having approximately twice the absorption strength of the magnon at $120\pm 0.5cm^{-1}$. Both lines have Zeeman splittings corresponding to a g value of 3.8 ± 0.4 figure 5.3) as compared to 4.8 for $CsCoCl_3$, 4.2 for $CsCoBr_3$ Lehmann et al. 1981) and an average value of 4.2 for $RbCoCl_3$ (Jorke and Durr).

The absorption at 111 cm^{-1} is at the frequency of a longitudinal optic phonon. Because of the absence of other strong lines, the magnon lines are assigned to the A series of lines where h=6J'. The absence of any other series of lines indicates that $RbCoBr_3$ at 1.7 Kelvin is in the fully ordered 3 dimensional phase as expected.

The eigenvalues of the tridiagonal matrix can now be fitted to the two magnon lines in terms of the longitudinal intrachain exchange strength (J), the transverse intrachain exchange strength (ε) and the longitudinal interchain exchange strength (J').

Because there are only two lines observed but 3 parameters in the matrix, one of the parameters must be fixed. ε is chosen to be 0.13 as this is the value for both $CsCoCl_3$ and $CsCoBr_3$ (Johnstone et al. 1980b). The matrix was limited to 10 dimensions (which corresponds to a chain of ten atoms) as there was very little change in the first ten eigenvalues when the number of dimensions was increased to 15 and the least change was in the lowest frequency values. The results of this fit for $RbCoBr_3$ are reported in Table 5.1. A

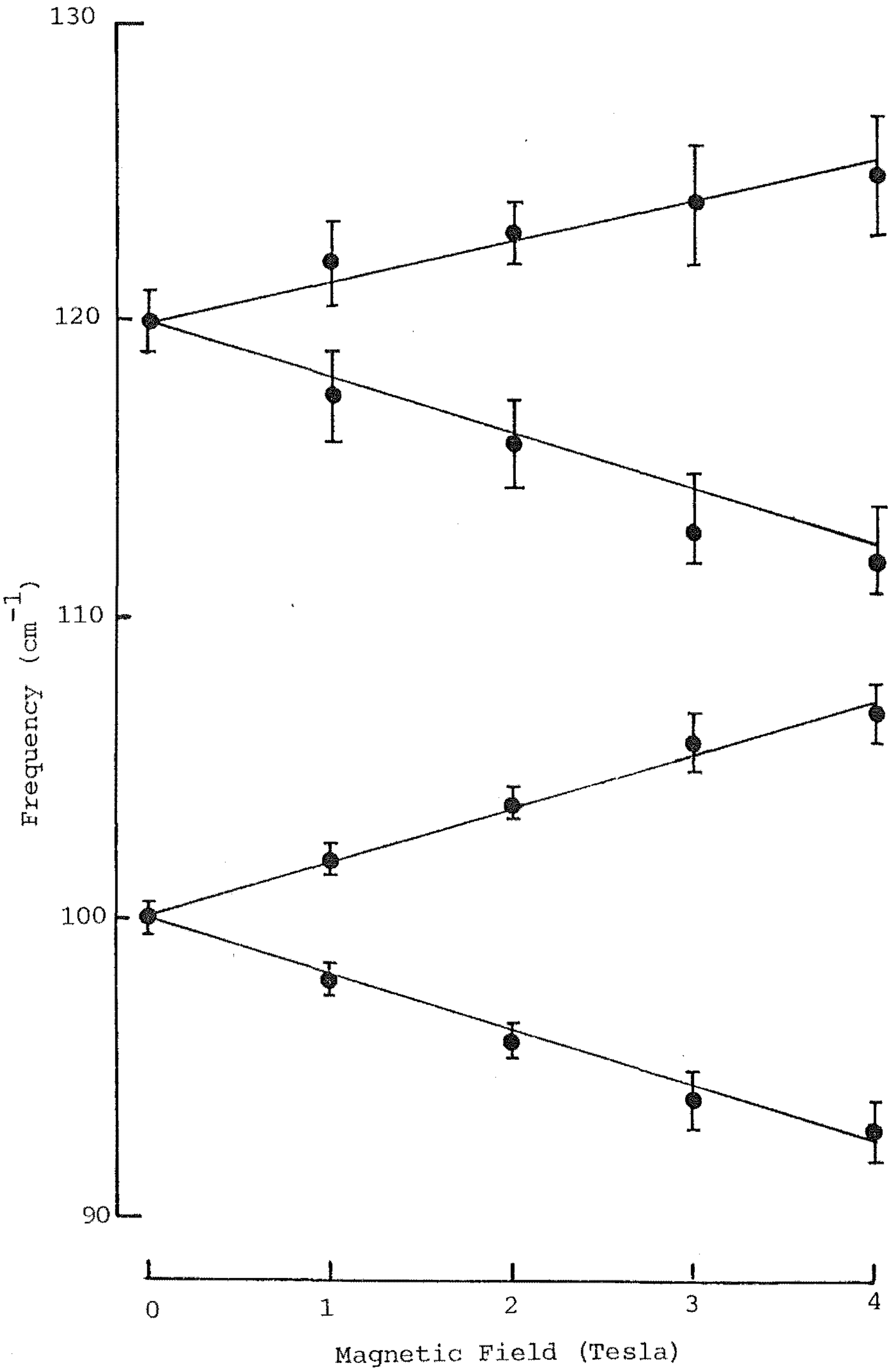

FIGURE 5.3 Zeeman splitting for magnons in $RbCoBr_3$ at 1.7 K. The solid lines correspond to level shifts for g=3.8.

	$CsCoBr_3$	$RbCoBr_3$	$CsCoCl_3$
Interchain lattice constants (A^o)	7.52	7.34	7.202
Intrachain lattice constants (A^o)	6.32	6.26	6.05
Intrachain exchange (J)	50.5	51	49.2
Interchain exchange ($\frac{h}{J}$)	0.11	0.06	0.037
Anisotropy (ε)	0.13	0.13	0.13

Table 5.2 Comparison of inter and intrachain parameters for $CsCoBr_3$, $RbCoBr_3$ and $CsCoCl_3$. The $CsCoBr_3$ and $CsCoCl_3$ exchange parameters are from Johnstone et al. 1980. The interchain and intrachain lattice spacings are from Ackerman et al. 1974

comparison of the parameters from this fit with those previously reported for $CsCoCl_3$ and $CsCoBr_3$ are given in table 5.2 where it can be seen that the interchain exchange parameters are sensitive to interchain spacing. There is little change for the intrachain parameters even though the intrachain distance change is comparable to the interchain change.

Temperature dependent studies need to be carried out on $RbCoBr_3$ to find out whether there is a transition to partial three dimensional ordering between 1.7K and the Neel temperature at 36 Kelvin (Melamud et al. 1974). If there is a transition then the appearance of the B_1 and B_2 series of lines would enable a better fit of the parameters ε,J and J'.

5.4 A POSSIBLE ANTIRESONANCE IN $RBCOBR_3$

In high resolution runs ($0.2cm^{-1}$) of the absorption spectra in $RbCoBr_3$ using sigma polarization, an unusual feature was observed at 114.6 cm^{-1} (figure 5.4). It has the features of an antiresonance line.

When a transition takes place into a discrete state superimposed on a continuum state, and when both states interact, the line shape of the absorption shows a characteristic asymmetric peak or dip. This phenomenon is known as antiresonance (Kishishita and Kaifu 1972).

The effect has been reported in many systems; in the $2s2p\,^1P$ resonance of He observed by inelastic scattering of electrons (Fano 1961); in the sharp electronic energy levels

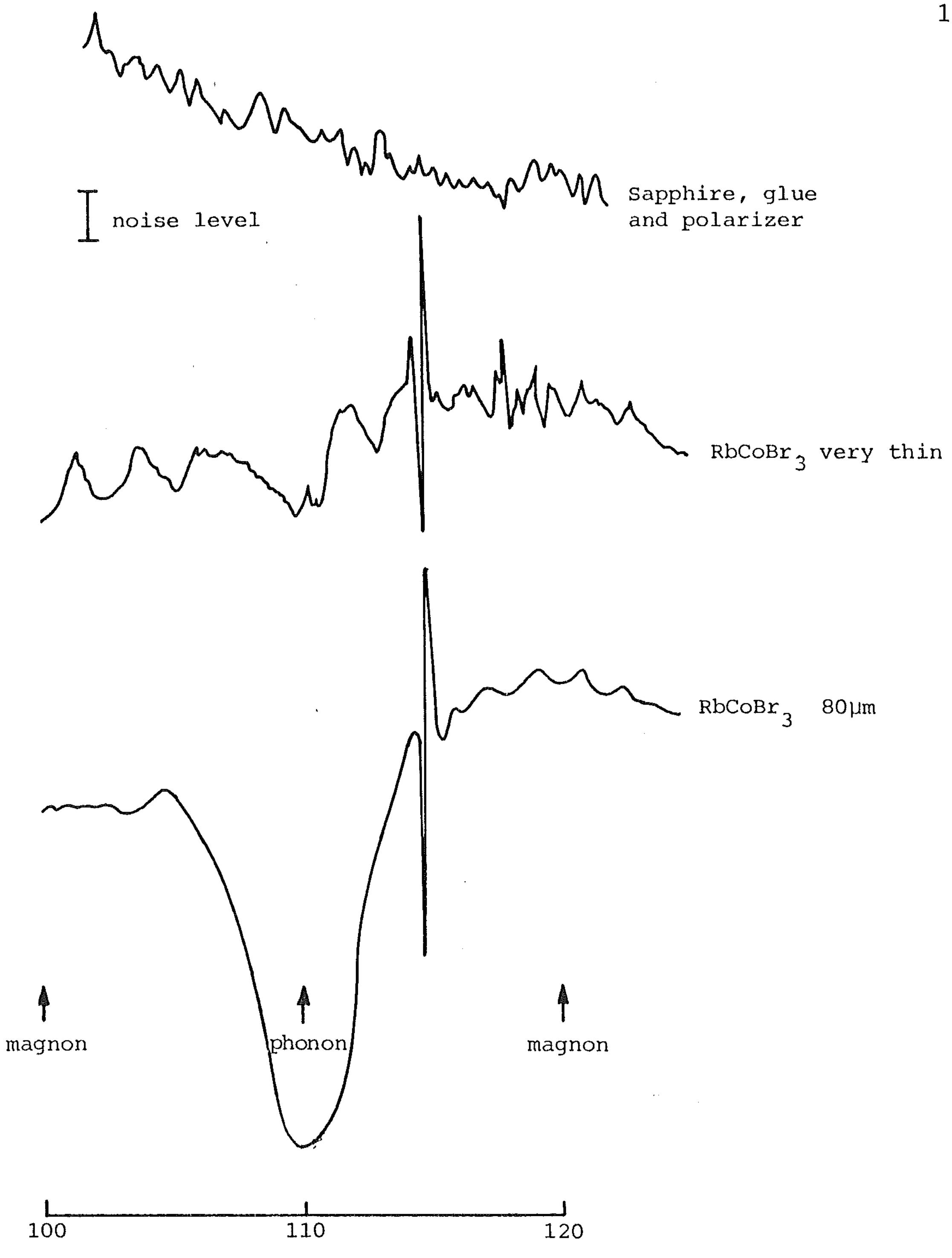

Figure 5.4 Antiresonance line observed in RbCoBr$_3$ at 1.7 K. The thin crystals are bonded to a sapphire substrate with cyanoacrylate glue.

Resolution 0.2cm^{-1} Polarization σ

observed in x-ray irradiated calcium fluoride doped with dysprosium superimposed on a broad background of colour centre absorption (Taylor 1969); in interference between exciton resonance of copper iodide micro-crystals and the light scattered from these crystals imbedded in potassium iodide (Kishishita and Kaifu 1972) and even in string instruments where the effect is due to the coupling between a string resonance and the principle body resonance of the instrument (Gouth 1985).

The feature shows strongly in high resolution, sigma polarization spectra of $RbCoBr_3$ (Figure 5.4). It does not occur in high resolution background spectra of the polarizer or sapphire and glue or both. This clearly indicates that the effect requires the presence of $RbCoBr_3$.

In thicker samples the feature is easily lost on the side of the nearby phonon (at $110cm^{-1}$). However the strength of the feature does not follow the thickness of the sample. This indicates a surface effect, possibility due to an interaction between the crystal and the glue. There is a possibility that water attack at the surface of the crystal is involved.

The feature appears in the pi polarization spectra but is much weaker and is hard to distinguish from the noise level.

Since antiresonance occurs in general when a discrete state coincides with a continuum absorption there is a possibility that some very sharp magnon interacts with the magnon continuum state (J'=0). This though is countered by the fact that the "antiresonance" line position does not correspond to any known magnon line in $RbCoBr_3$. The magnons are also seen only in the pi and not the sigma polarization.

This phenomena is reported here for completeness. Further work needs to be done to determine whether this effect occurs in other crystals having similar structure to $RbCoBr_3$.

5.5 A PRELIMINARY SEARCH FOR MAGNONS IN OTHER $CSNICL_3$ TYPE CRYSTALS

Magnons were also searched for in various other magnetic crystals of the same structure as $RbCoBr_3$. These included $RbMnBr_3$, $RbNiCl_3$, $CsNiBr_3$, $CsNiCl_3$, $CsFeCl_3$ and $RbFeCl_3$. Various lines other than the expected lattice phonons were observed in polarized spectra of thick (1mm) samples. Some of the lines subsequently were found to be at the longitudinal optic frequencies of phonon modes. This highlighted the need for the phonon spectra to be well understood as in chapter 4.

Table 5.3 lists the absorption lines that are not accounted for by the transverse optic phonons, longitudinal optic phonons or obvious water attack. As most of the remaining lines fall into distinct groups, including one group of three or four lines between 100 and $140cm^{-1}$ and one of a line at about $30cm^{-1}$, most may yet be attributed to water vapour attack.

Magnons can only be clearly distinguished from phonons

	σ					π	
$RbNiCl_3$	120	132	140			123	140
$CsNiCl_3$	112	116	133	142		36	
$CsCoCl_3$	109	114	119	126	131	33	
$CsMnBr_3$	127					-	

TABLE 5.3 Unassigned absorption lines in thick crystals of the $CsNiCl_3$ structure. Sample thickness are typically 1 mm.

and impurity absorption lines by their temperature dependence or by their behaviour in a magnetic field. However bear in mind that some phonons couple to magnons of similar energy (Lockwood et al. 1983) and they therefore have a magnetic field dependence. Apparatus for variable temperature measurements was not available for the far infrared measurements reported in this thesis. Some Zeeman experiments were attempted before the bolometer element was fully shielded from the magnetic field but no conclusive results were obtained. Insufficient liquid helium prevented a later Zeeman search of Mn, Fe and Ni based $CsNiCl_3$ type crystals.

This work could form the basis of a future project.

CHAPTER 6

CONCLUSIONS

A Commodore PET microcomputer has been interfaced to the Grubb Parsons IS3 far infrared interferometer to control the interferometer and to allow the Fourier transform of the spectra to be carried out in real time. This has resulted in a considerable increase in productive experiment time.

A new He^3 cooled bolometer has been designed and constructed. This involved considerable development in the design of suitable He^3 refrigerators. The bolometer was incorporated into a new superconducting magnet and Dewar system which enabled Zeeman experiments to be carried out in magnetic fields up to 5 Tesla. The magnet is placed as low as possible in the Dewar to maximize the running time at high fields. The resulting problems of the magnetic field of the magnet effecting the bolometer element have been successfully overcome by magnetically shielding the element with a superconducting shield.

The theory of the transmission of radiation through slabs of non-isotropic dielectric crystals mounted on a dielectric substrate has been developed. These slab equations show that radiation incident normally onto thin films produces absorption lines at the transverse optic modes only but at non-normal incidence absorption lines are produced also at the longitudinal mode frequencies. For large angles of incidence and low dielectric constants another, smaller, absorption line is expected above the longitudinal mode frequency. This is an effect similar to total internal reflection in an isotropic dielectric.

As the sample thickness increases, the transverse optic mode lines broaden asymmetrically but longitudinal mode lines broaden symmetrically. For thick samples the transverse mode frequency is near the lower frequency edge of the absorption band while the longitudinal mode frequency is near the higher frequency edge of the absorption band. The slab equations reproduce all the main features of the far infrared absorption spectra of $CsNiCl_3$ type crystals.

The infrared active phonons in thirteen crystals of the $CsNiCl_3$ type structure have been reported. A factor group analysis of the structure, together with polarization studies, have enabled the absorption lines to be identified with particular phonon modes of the crystal. For $RbCoBr_3$ and $RbMnBr_3$, extra phonon lines indicate that these may be of a slightly different structure than the $CsNiCl_3$ structure. Further x-ray diffraction work at low temperatures needs to be undertaken to test this hypothesis.

Two magnon lines have been identified in $RbCoBr_3$ at $100\pm0.5cm^{-1}$ and $120\pm0.5cm^{-1}$ through polarized Zeeman spectroscopy. Each magnon has a g value of 3.8 ± 0.4. Using the perturbed Ising (linear chain) model, and assuming a relative transverse magnetic exchange interaction (anisotropy constant) of $\varepsilon=0.13$, the magnon energies determine a longitudinal intrachain magnetic exchange interaction J of value $51cm^{-1}$ and a relative interchain exchange interaction h/J of 0.06. These values are consistent with those reported by other workers for $CsCoCl_3$ and $CsCoBr_3$ in their fully ordered, three dimensional magnetic structure where neighbours in the next nearest chains have spins in the same direction.

A possible antiresonance line was found at 114.6 cm^{-1} in $RbCoBr_3$ at 1.7K. The line strength does not vary with thickness thus indicating a surface effect. Further work is needed to investigate the cause of this phenomena. In particular, high resolution, polarized Zeeman spectra are needed.

Magnons in $ACoX_3$ crystals have been reported by other workers using Raman Spectroscopy. The dark crystals of $AMnX_3$, $AFeCl_3$ and $ANiX_3$ are not easily examined by Raman spectroscopy. These crystals are amenable to study using far infrared, polarized, Zeeman spectroscopy as shown by the preliminary spectra reported in this thesis. Such a study could form the basis of a future project.

APPENDIX 1

Fourier transform program written in Basic to run on a Commodore PET microcomputer

```
1 GOTO90:REM**FTS***21/03/83***
2 REM**DRAW BOX**
3 PRINT"▒▒";
4 PRINT"        ▓▓▓▓▓▓▓▓▓▓▓▓▓▓▓▓▓▓▓▓▓▓▓▓▓▓▓▓▓▓▓▓▓▓▓▓ ";
5 PRINT"100▒▒ ▒-                                   -▒";
6 FOR I=1TO4
7 FORJ=1TO3
8 PRINT"    ▒▒ ▒                                   ▒";:NEXTJ
9 PRINT100-I*20"▒▒▒ ▒-                               -▒";
10 NEXTI
11 FORJ=1TO3
12 PRINT"    ▒▒ ▒                                   ▒";:NEXTJ
13 PRINT"  0▒▒ ▒-                                   -▒";
18 PRINT"    ▒▒▓▓▓▓▓▓▓▓▓▓▓▓▓▓▓▓▓▓▓▓▓▓▓▓▓▓▓▓▓▓▓▓▓▓▓▓▓▒ ";
19 PRINT"ER="INT(ER*100)/100;
20 FORL=0TO5
21 X=(KBIG+L*XS-KSTART)/DK
22 JL X,-4,X,-1
24 JL X,164,X,162
28 NEXT L
30 RETURN:REM**********************
40 K1=K1+KV:K2=K2+INC:APOD=APOD-32768/NS
41 IF K1>32760 THEN K1=K1-32760
42 IF K2>32760 THEN K2=K2-32760
43 POKE24549,K1/256:POKE24548,K1AND255
44 POKE24436,K2/256:POKE24428,K2AND255
45 IF APOD<0 THEN APOD=0
46 POKE24068,APOD/256:POKE24069,APODAND255
47 RETURN
50 REM**PLOTTING OF SPECTRUM*****
52 POKE48895,6
54 SCLEAR10,183,315,25
58 SY=160/(PEEK(24075)*256+PEEK(24076))
59 JM 1,(PEEK(14950)*256+PEEK(14949))*SY
60 FOR J=1TONN
62 S=PEEK(14952-2*J)*256+PEEK(14951-2*J)
64 IF S>=32768 THEN S=-(S-32768)
66 JD J,S*SY
68 NEXTJ
88 RETURN:REM*************
90 DATA 10,1,0,250,1,N,999/9
92 READ DX,DK,KSTART,KND,TC,S$,N$
94 PRINT"▒STEPPING INTERVAL "DX:PRINT"TIME INTERVAL "TC
95 PRINT"MAXIMUM RESOLUTION "DK:PRINT"START AND END FREQUENCIES "KSART"▒,"KND
96 PRINT"SAMPLE NAME    ";S$:PRINT"FILE NAME (EXP NO./RUN NO.)   ";N$
98 IF VAR$="" THEN VAR$="1":GOTO 103
100 PRINT"▒▒▒DO YOU WANT TO CHANGE VARIABLES (Y/N)?"
101 GET VAR$:IF VAR$<>"N" AND VAR$<>"Y" THEN101
```

```
102 PRINT"□                                                    ▓":IFVAR$="N"GOTO106
103 PRINT"▓"TAB(17);:INPUTDX  :PRINTTAB(13);:INPUTTC:PRINTTAB(18);:INPUTDK
104 PRINTTAB(25);:INPUTKSTART,KND:PRINTTAB(12);:INPUTS$:PRINTTAB(27);:INPUTN$
105 GOTO94
106 PRINT"▓STARTING SCAN"
107 NK=(KND-KSTART)/DK
108 NN=NK-1
110 POKE48895,6:JX:GMODE1
130 SETWIN0,0,0,319,199
155 SETWIN3,30,25,315,187
160 CLEAR
170 SCALE 0,0:CHSCALE0:WINDOW0:XFFLG1
195 REM***DRAW X AXIS AND AXES LABELS***
200 OFFSET 40,23
210 XT$="FREQUENCY(CM-1)":YT$="RELATIVE INTENSITY"
230 JM 100,-23:JC XT$
240 JM -34,30:CHROT 1:CHAR YT$:CHROT 0
243 XS=50*DK
245 KBIG=XS*(1+INT(KSTART/XS))
250 FOR L=0 TO 5
260 KAXIS=KBIG+L*XS
270 JM (KAXIS-KSTART)/DK-14,-15:JC STR$(KAXIS)
280 NEXT L
295 JM 250-LEN(S$)*6,170:JC S$
412 T=TI
490 DOPEN#1,(N$),W
500 PRINT#1,S$
501 IF DS>20 THEN 20000
510 PRINT#1,DX
520 FOR J=1 TO NN
540 POKE14952-2*J,0:POKE14951-2*J,0
560 NEXT J
570 POKE24075,1
600 KV=KSTART*DX*1E-4*32760
620 INC=DK*DX*1E-4*32760
640 NS=1/(1E-4*DX*DK)
760 APOD=32768:POKE24068,128:POKE24069,0
800 POKE48895,1
801 POKE40975,0
802 POKE40974,127
803 POKE40975,4
820 POKE40963,0
840 POKE40962,0
860 POKE40963,4
880 POKE40961,0
900 POKE40960,0
920 POKE40961,60
940 A=PEEK(40960)
950 POKE48895,6
1370 POKE24401,NN/256:POKE24396,NN-256*INT(NN/256)-1
1380 POKE48895,1
1390 TI$="000000"
1400 T=TI:BASE=0
1450 FORI=1 TO 10
1460 IF TI-T<TC*60 THEN1460
1500 SYS23153:BASE=BASE+PEEK(24064)*256+PEEK(24065)
1502 FOR Z=1 TO DX/5:POKE40976,252:NEXTZ
1504 T=TI
1520 NEXT I
1550 BASE=BASE/10:PRINT"BASELINE = ";BASE
1560 PRINT#1,BASE
```

```
1570 SS=210-DX*2
1575 FORI=1TOSS:POKE40976,252:NEXTI
1578 FOR Z=1TODX/5
1579 POKE48895,1:IF PEEK(40974)<128 THEN POKE40976,252:POKE48895,6
1580 NEXTZ
1589 T=TI
1590 IF TI-T<TC*60 THEN1590
1600 POKE48895,1:SYS23153:POKE48895,6: A2=PEEK(24065)+256*PEEK(24064):PRINT A2;
1610 IF A2<1.2*BASE THEN A1=A2:GOTO1578
1611 TEMP=A2
1612 T=TI
1613 IFTI-T<TC*60THEN1613
1614 POKE48895,1:SYS23153:POKE48895,6
1615 A2=PEEK(24065)+256*PEEK(24064):PRINTA2
1616 IF(A2<TEMP-10)OR(A2>TEMP+10)THEN TEMP=A2:GOTO1612
1620 FORZ=1TODX/5
1621 POKE48895,1:IF PEEK(40974)<128 THEN POKE40976,252:POKE48895,6
1622 NEXTZ:PRINTCHR$(7)
1630 TEMP=0
1660 T=TI
1680 IF TI-T<TC*60 THEN1680
1700 POKE48895,1:SYS23153:POKE48895,6
1712 A3=PEEK(24065)+256*PEEK(24064):PRINTA3
1715 IF (A3<TEMP-10)OR(A3>TEMP+10)THEN TEMP=A3:GOTO1660
1720 IF A3>A2 THEN A1=A2:A2=A3:GOTO 1620
1721 FORZ=1TODX/5
1722 POKE48895,1:IF PEEK(40974)<128THEN POKE40976,252:POKE48895,6:NEXTZ
1723 T=TI
1727 ER=(A3-A1)/((A1+A3-2*A2)*2)
1728 PRINT#1,ER;CHR$(13);CHR$(A2/256);CHR$(A2-256*INT(A2/256));
1729 PRINTER;A1;A2;A3
1780 K1=32760.5+KV*ER
1785 IF K1>32760 THEN K1=K1-32760
1790 K2=32760.5+INC*ER
1795 IF K2>32760 THEN K2=K2-32760
1800 POKE24549,K1/256:POKE24548,K1-256*INT(K1/256)
1805 POKE24436,K2/256:POKE24428,K2-256*INT(K2/256)
1820 X=BASE*2*(0.5+ER):POKE24066,X/256:POKE24067,X-256*INT(X/256)
2150 A4=A2*(0.5+ER)
2170 POKE24064,A4/256:POKE24065,A4-256*INT(A4/256)
2190 SYS24224
2200 PRINT"□0 "A2
8000 GOSUB2:WINDOW3:PVMEM:GOSUB50
8040 GOSUB40
8400 X=BASE*2:POKE24066,X/256:POKE24067,X-256*INT(X/256)
8460 POKE24064,A3/256:POKE24065,A3-256*INT(A3/256)
8470 PRINT#1,CHR$(A3/256);CHR$(A3-256*INT(A3/256));
8480 SYS24224
8490 PRINT"▩1 ";A3
8600 FOR I=2 TO NS
8710 IF TI-T<TC*60 THEN8710
8711 B=INT((TI-T)/6)/10
8720 POKE48895,1:SYS23153
8721 FOR Z=1TODX/5
8722 IF PEEK(40974)>127THEN 10120
8723 POKE40976,252
8725 NEXT Z
8728 POKE48895,6
8730 T=TI
```

```
8800 PRINT "█"I;PEEK(24064)*256+PEEK(24065)"█  ";TI$;B"█     "
8802 PRINT#1,CHR$(PEEK(24064));CHR$(PEEK(24065));
8804 GOSUB40
8850 SYS24224
9001 GETA$:IF A$="U" THEN GOSUB50
9002 IF A$="S" THEN 10120
9003 IF A$="A" THEN GOSUB 50:SS=I:F$="A":GOTO 18030
10000 IF A$="F" THEN PRINT"███"TAB(35)"█F";F$="F"
10100 NEXT I
10120 GOSUB50
10150 SS=I
16000 DCLOSE#1
16500 NS$="S"+N$
17000 DOPEN#2,(NS$),W:IF DS>20THEN20000
17010 PRINT#2,S$:PRINT#2,KSTART+DK:PRINT#2,DK
17025 PRINT#2,CHR$(PEEK(24075));CHP$(PEEK(24076));
17100 FOR I= 1 TO NN
17200 PRINT#2,CHR$(PEEK(14952+2*-I));CHR$(PEEK(14951+2*-I));
17300 NEXT I
17400 DCLOSE#2
17425 SMAX=PEEK(24075)*256+PEEK(24076)
17450 KAXIS=(KBIG-KSTART)/DK
17490 POKE48895,1:POKE40968,0:POKE40970,0
17492 FORK=1TO1000:NEXTK
17500 POKE40974,255:Z1=0:Z2=250:Z3=1:Z4=50:Y1=0:Y2=5
17510 GOSUB20700
17515 FORI=0TO225STEP 25
17516 FORJ=0TO25
17517 POKE40970,I+J:NEXTJ
17518 FORK=1TO70:NEXTK
17520 POKE40968,245
17522 FORK=1TO70:NEXTK
17524 POKE40968,250
17526 FORK=1TO70:NEXTK
17528 NEXTI
17529 KAXIS=KAXIS-50
17530 Z1=250:Z2=0:Z3=-1:Z4=-50:Y1=250:Y2=245
17534 GOSUB20700
17540 FORI=250TO25STEP-25
17549 FORJ=0TO25
17550 POKE40970,I-J:NEXTJ
17552 FORK=1TO100:NEXTK
17554 POKE40968,5
17556 FORK=1TO100:NEXTK
17558 POKE40968,0
17560 FORK=1TO100:NEXTK
17580 NEXTI
17600 FORI=1TO NN
17650 S=PEEK(14952-2*I)*256+PEEK(14951-2*I)
17700 IFS>32768 THEN S=1
17750 S=S*250/SMAX
17751 IF S=SO THEN 17760
17752 X=1:A2=1/(S-SO)
```

```
17754 IF S<SO THEN X=-1
17760 FOR L=SO TO S STEP X
17770 POKE40970,L
17800 IFI<255 THEN  POKE40968,I+A2*(L-SO)
17860 NEXTL
17870 SO=S
17900 NEXTI
17901 POKE40974,0
18000 N=VAL(RIGHT$(N$,LEN(N$)-4))
18010 N$=LEFT$(N$,4)+RIGHT$(STR$(N+1),LEN(STR$(N+1))-1)
18030 POKE48895,1:NO=SS*DX/5+230
18040 FORL=1TONO:POKE40976,254:NEXTL
18042 FOR I=1TO1000:NEXTI
18043 GETA$:IF A$="F" THEN F$="F"
18045 IF F$="A" THEN DCLOSE:SCRATCH (N$):F$="F"
18049 IF  F$="F"THEN POKE48895,6:JP:F$="":GOTO94
18050 GOTO490
20000 X=1
20300 IF X=1 THEN  PRINT"▩"CHR$(7);
20400 PRINTDS$"□":X=-X:GOTO20300
20700 FOR I=Z1TOZ2 STEP Z3
20710 POKE40968,I
20720 IF I<>KAXIS THEN 20750
20730 FORK=1TO100:NEXTK:POKE40970,Y1:POKE40970,Y2:FORK=1TO100:NEXTK
20740 POKE40970,Y1:FORK=1TO100:NEXTK
20745 KAXIS=KAXIS+Z4
20750 NEXTI
20780 RETURN
```

Machine code routine for Fourier transform program.
The code is written to run on the Commodore PET's
6502 microprocessor.

```
" ,  5A71 A9 34    LDA #$34
" ,  5A73 8D 01 A0 STA $A001
" ,  5A76 A9 FF    LDA #$FF
" ,  5A78 E9 01    SBC #$01
" ,  5A7A D0 FC    BNE $5A78
" ,  5A7C A9 FF    LDA #$FF
" ,  5A7E E9 01    SBC #$01
" ,  5A80 D0 FC    BNE $5A7E
" ,  5A82 A9 3C    LDA #$3C
" ,  5A84 8D 01 A0 STA $A001
" ,  5A87 AD 01 A0 LDA $A001
" ,  5A8A 10 FB    BPL $5A87
" ,  5A8C EA       NOP
" ,  5A8D EA       NOP
" ,  5A8E EA       NOP
" ,  5A8F EA       NOP
" ,  5A90 EA       NOP
" ,  5A91 EA       NOP
" ,  5A92 AD 00 A0 LDA $A000
" ,  5A95 8D 01 5E STA $5E01
" ,  5A98 AD 02 A0 LDA $A002
" ,  5A9B 29 0F    AND #$0F
" ,  5A9D 8D 00 5E STA $5E00
" ,  5AA0 60       RTS
" ,  5AA1 AA       TAX
"
"

" ,  5DF3 AD E4 5F LDA $5FE4
" ,  5DF6 E9 F8    SBC #$F8
" ,  5DF8 AD E5 5F LDA $5FE5
" ,  5DFB E9 7F    SBC #$7F
" ,  5DFD 4C 12 5E JMP $5E12
" ,  5E00 00       BRK
"
"

" ,  5E12 90 10    BCC $5E24
" ,  5E14 AD E4 5F LDA $5FE4
" ,  5E17 E9 F8    SBC #$F8
" ,  5E19 8D E4 5F STA $5FE4
" ,  5E1C AD E5 5F LDA $5FE5
" ,  5E1F E9 7F    SBC #$7F
" ,  5E21 8D E5 5F STA $5FE5
" ,  5E24 60       RTS
" ,  5E25 AA       TAX
"
```

```
" ,  5EA0 A9 00    LDA #$00
" ,  5EA2 8D 0D 5E STA $5E0D
" ,  5EA5 8D 0E 5E STA $5E0E
" ,  5EA8 8D 0B 5E STA $5E0B
" ,  5EAB 8D 0C 5E STA $5E0C
" ,  5EAE A9 68    LDA #$68
" ,  5EB0 8D C8 5F STA $5FC8
" ,  5EB3 A9 67    LDA #$67
" ,  5EB5 8D CE 5F STA $5FCE
" ,  5EB8 A9 3A    LDA #$3A
" ,  5EBA 8D C9 5F STA $5FC9
" ,  5EBD 8D CF 5F STA $5FCF
" ,  5EC0 8E 0A 5E STX $5E0A
" ,  5EC3 0E 01 5E ASL $5E01
" ,  5EC6 2E 00 5E ROL $5E00
" ,  5EC9 EA       NOP
" ,  5ECA EA       NOP
" ,  5ECB EA       NOP
" ,  5ECC EA       NOP
" ,  5ECD EA       NOP
" ,  5ECE EA       NOP
" ,  5ECF 38       SEC
" ,  5ED0 AD 01 5E LDA $5E01
" ,  5ED3 ED 03 5E SBC $5E03
" ,  5ED6 8D 01 5E STA $5E01
" ,  5ED9 AD 00 5E LDA $5E00
" ,  5EDC ED 02 5E SBC $5E02
" ,  5EDF 8D 00 5E STA $5E00
" ,  5EE2 B0 10    BCS $5EF4
" ,  5EE4 A9 01    LDA #$01
" ,  5EE6 ED 01 5E SBC $5E01
" ,  5EE9 8D 01 5E STA $5E01
" ,  5EEC A9 80    LDA #$80
" ,  5EEE ED 00 5E SBC $5E00
" ,  5EF1 8D 00 5E STA $5E00
" ,  5EF4 A0 00    LDY #$00
" ,  5EF6 0E 01 5E ASL $5E01
" ,  5EF9 2E 00 5E ROL $5E00
" ,  5EFC 90 01    BCC $5EFF
" ,  5EFE C8       INY
" ,  5EFF 8C 0A 5E STY $5E0A
" ,  5F02 A9 00    LDA #$00
" ,  5F04 8D 06 5E STA $5E06
" ,  5F07 8D 07 5E STA $5E07
" ,  5F0A A2 10    LDX #$10
" ,  5F0C 4E 04 5E LSR $5E04
" ,  5F0F 6E 05 5E ROR $5E05
" ,  5F12 90 13    BCC $5F27
" ,  5F14 18       CLC
" ,  5F15 AD 07 5E LDA $5E07
" ,  5F18 6D 01 5E ADC $5E01
" ,  5F1B 8D 07 5E STA $5E07
" ,  5F1E AD 06 5E LDA $5E06
" ,  5F21 6D 00 5E ADC $5E00
" ,  5F24 8D 06 5E STA $5E06
" ,  5F27 4E 06 5E LSR $5E06
" ,  5F2A 6E 07 5E ROR $5E07
" ,  5F2D CA       DEX
```

```
.,  5F2E F0 03     BEQ $5F33
.,  5F30 4C 0C 5F  JMP $5F0C
.,  5F33 AD 06 5E  LDA $5E06
.,  5F36 8D 00 5E  STA $5E00
.,  5F39 AD 07 5E  LDA $5E07
.,  5F3C 8D 01 5E  STA $5E01
.,  5F3F 4C 4A 5F  JMP $5F4A
.,  5F42 AA        TAX
.,  5F43 AA        TAX
.,  5F44 AA        TAX
.,  5F45 AA        TAX
.,  5F46 AA        TAX
.,  5F47 AA        TAX
.,  5F48 AA        TAX
.,  5F49 AA        TAX
.,  5F4A 38        SEC
.,  5F4B A9 F8     LDA #$F8
.,  5F4D ED 0E 5E  SBC $5E0E
.,  5F50 A9 00     LDA #$00
.,  5F52 ED 0D 5E  SBC $5E0D
.,  5F55 B0 03     BCS $5F5A
.,  5F57 60        RTS
.,  5F58 28        PLP
.,  5F59 5E A9 00  LSR $00A9,X
.,  5F5C 6D 0E 5E  ADC $5E0E
.,  5F5F 8D 0E 5E  STA $5E0E
.,  5F62 A9 00     LDA #$00
.,  5F64 6D 0D 5E  ADC $5E0D
.,  5F67 8D 0D 5E  STA $5E0D
.,  5F6A 18        CLC
.,  5F6B A9 14     LDA #$14
.,  5F6D 6D E4 5F  ADC $5FE4
.,  5F70 8D E4 5F  STA $5FE4
.,  5F73 A9 00     LDA #$00
.,  5F75 6D E5 5F  ADC $5FE5
.,  5F78 8D E5 5F  STA $5FE5
.,  5F7B 20 F2 5D  JSR $5DF2
.,  5F7E 4C 98 5F  JMP $5F98
.,  5F81 AA        TAX
.,  5F82 AA        TAX
.,  5F83 AA        TAX
.,  5F84 AA        TAX
.,  5F85 AA        TAX
.,  5F86 AA        TAX
.,  5F87 AA        TAX
.,  5F88 AA        TAX
.,  5F89 AA        TAX
.,  5F8A AA        TAX
.,  5F8B AA        TAX
.,  5F8C AA        TAX
.,  5F8D AA        TAX
.,  5F8E AA        TAX
.,  5F8F AA        TAX
.,  5F90 AA        TAX
.,  5F91 AA        TAX
.,  5F92 AA        TAX
.,  5F93 AA        TAX
.,  5F94 AA        TAX
.,  5F95 AA        TAX
```

```
.,  5F96 AA       TAX
.,  5F97 AA       TAX
.,  5F98 38       SEC
.,  5F99 AD C8 5F LDA $5FC8
.,  5F9C E9 02    SBC #$02
.,  5F9E 8D C8 5F STA $5FC8
.,  5FA1 8D EB 60 STA $60EB
.,  5FA4 AD C9 5F LDA $5FC9
.,  5FA7 E9 00    SBC #$00
.,  5FA9 8D C9 5F STA $5FC9
.,  5FAC 8D EC 60 STA $60EC
.,  5FAF 38       SEC
.,  5FB0 AD CE 5F LDA $5FCE
.,  5FB3 E9 02    SBC #$02
.,  5FB5 8D CE 5F STA $5FCE
.,  5FB8 8D F1 60 STA $60F1
.,  5FBB AD CF 5F LDA $5FCF
.,  5FBE E9 00    SBC #$00
.,  5FC0 8D CF 5F STA $5FCF
.,  5FC3 8D F2 60 STA $60F2
.,  5FC6 EA       NOP
.,  5FC7 AD 76 38 LDA $3876
.,  5FCA 8D 08 5E STA $5E08
.,  5FCD AD 75 38 LDA $3875
.,  5FD0 8D 09 5E STA $5E09
.,  5FD3 4C E6 5F JMP $5FE6
.,  5FD6 AA       TAX
.,  5FD7 AA       TAX
.,  5FD8 AA       TAX
.,  5FD9 AA       TAX
.,  5FDA AA       TAX
.,  5FDB AA       TAX
.,  5FDC AA       TAX
.,  5FDD AA       TAX
.,  5FDE AA       TAX
.,  5FDF AA       TAX
.,  5FE0 AA       TAX
.,  5FE1 AA       TAX
.,  5FE2 AA       TAX
.,  5FE3 02       ???
.,  5FE4 74       ???
.,  5FE5 13       ???
.,  5FE6 AD E5 5F LDA $5FE5
.,  5FE9 8D E3 5F STA $5FE3
.,  5FEC AD E4 5F LDA $5FE4
.,  5FEF A2 03    LDX #$03
.,  5FF1 4E E3 5F LSR $5FE3
.,  5FF4 6A       ROR
.,  5FF5 CA       DEX
.,  5FF6 F0 03    BEQ $5FFB
.,  5FF8 4C F1 5F JMP $5FF1
.,  5FFB 18       CLC
.,  5FFC 69 69    ADC #$69
.,  5FFE 8D 0A 60 STA $600A
.,  6001 AD E3 5F LDA $5FE3
.,  6004 69 3A    ADC #$3A
.,  6006 8D 0B 60 STA $600B
.,  6009 AD D7 3C LDA $3CD7
.,  600C 8D 04 5E STA $5E04
.,  600F AD 0A 60 LDA $600A
.,  6012 69 00    ADC #$00
```

```
.,  6014 8D 20 60 STA $6020
.,  6017 AD 0B 60 LDA $600B
.,  601A 69 10    ADC #$10
.,  601C 8D 21 60 STA $6021
.,  601F AD D7 4C LDA $4CD7
.,  6022 8D 05 5E STA $5E05
.,  6025 EA       NOP
.,  6026 EA       NOP
.,  6027 EA       NOP
.,  6028 EA       NOP
.,  6029 EA       NOP
.,  602A EA       NOP
.,  602B EA       NOP
.,  602C AC 0A 5E LDY $5E0A
.,  602F 0E 05 5E ASL $5E05
.,  6032 2E 04 5E ROL $5E04
.,  6035 90 01    BCC $6038
.,  6037 C8       INY
.,  6038 A9 00    LDA #$00
.,  603A 8D 06 5E STA $5E06
.,  603D 8D 07 5E STA $5E07
.,  6040 A2 10    LDX #$10
.,  6042 4E 04 5E LSR $5E04
.,  6045 6E 05 5E ROR $5E05
.,  6048 90 13    BCC $605D
.,  604A 18       CLC
.,  604B AD 07 5E LDA $5E07
.,  604E 6D 01 5E ADC $5E01
.,  6051 8D 07 5E STA $5E07
.,  6054 AD 06 5E LDA $5E06
.,  6057 6D 00 5E ADC $5E00
.,  605A 8D 06 5E STA $5E06
.,  605D 4E 06 5E LSR $5E06
.,  6060 6E 07 5E ROR $5E07
.,  6063 CA       DEX
.,  6064 F0 03    BEQ $6069
.,  6066 4C 42 60 JMP $6042
.,  6069 C0 01    CPY #$01
.,  606B D0 03    BNE $6070
.,  606D 38       SEC
.,  606E B0 01    BCS $6071
.,  6070 18       CLC
.,  6071 6E 06 5E ROR $5E06
.,  6074 6E 07 5E ROR $5E07
.,  6077 AD 08 5E LDA $5E08
.,  607A 10 11    BPL $608D
.,  607C 38       SEC
.,  607D A9 00    LDA #$00
.,  607F ED 09 5E SBC $5E09
.,  6082 8D 09 5E STA $5E09
.,  6085 A9 80    LDA #$80
.,  6087 ED 08 5E SBC $5E08
.,  608A 8D 08 5E STA $5E08
.,  608D AD 06 5E LDA $5E06
.,  6090 10 11    BPL $60A3
.,  6092 38       SEC
.,  6093 A9 00    LDA #$00
.,  6095 ED 07 5E SBC $5E07
```

```
" ,   6098 8D 07 5E STA $5E07
" ,   609B A9 80    LDA #$80
" ,   609D ED 06 5E SBC $5E06
" ,   60A0 8D 06 5E STA $5E06
" ,   60A3 18       CLC
" ,   60A4 AD 09 5E LDA $5E09
" ,   60A7 6D 07 5E ADC $5E07
" ,   60AA 8D 09 5E STA $5E09
" ,   60AD AD 08 5E LDA $5E08
" ,   60B0 6D 06 5E ADC $5E06
" ,   60B3 8D 08 5E STA $5E08
" ,   60B6 10 14    BPL $60CC
" ,   60B8 38       SEC
" ,   60B9 A9 00    LDA #$00
" ,   60BB ED 09 5E SBC $5E09
" ,   60BE 8D 09 5E STA $5E09
" ,   60C1 A9 80    LDA #$80
" ,   60C3 ED 08 5E SBC $5E08
" ,   60C6 8D 08 5E STA $5F08
" ,   60C9 4C E7 60 JMP $60E7
" ,   60CC 38       SEC
" ,   60CD AD 09 5E LDA $5E09
" ,   60D0 ED 0C 5E SBC $5E0C
" ,   60D3 AD 08 5E LDA $5E08
" ,   60D6 ED 0B 5E SBC $5E0B
" ,   60D9 90 0C    BCC $60E7
" ,   60DB AD 09 5E LDA $5E09
" ,   60DE 8D 0C 5E STA $5E0C
" ,   60E1 AD 08 5E LDA $5E08
" ,   60E4 8D 0B 5E STA $5E0B
" ,   60E7 AD 08 5E LDA $5E08
" ,   60EA 8D 76 38 STA $3876
" ,   60ED AD 09 5E LDA $5E09
" ,   60F0 8D 75 38 STA $3875
" ,   60F3 4C 4A 5F JMP $5F4A
" ,   60F6 AA       TAX
"
```

APPENDIX 2

Thin film spectra of the infrared-active lattice modes in $CdCl_2$ type crystals.

Published in J Phys C : Solid State Phys, 16 (1983) 999-1008 (with J.A. Campbell).

J. Phys. C: Solid State Phys., **16** (1983) 999–1008. Printed in Great Britain

Thin film spectra of the infrared-active lattice modes in $CdCl_2$ type crystals†

J A Campbell and R E M Vickers
Department of Physics, University of Canterbury, Christchurch, New Zealand

Received 27 July 1982

Abstract. Expressions are derived for the far-infrared transmission at non-normal incidence of thin films of anisotropic single crystals. The sellotape stripping technique is used to produce suitable films of $CdCl_2$ type crystals with the crystal *c* axis perpendicular to the plane of the film. With these films the frequencies of the E_u(TO) and A_{2u}(LO) infrared-active modes have been measured for $CdCl_2$, $CdBr_2$, CdI_2, $MgCl_2$, $MnCl_2$, $FeCl_2$, $CoCl_2$, $NiCl_2$, $CoBr_2$ and $NiBr_2$ at low temperatures. Although CdI_2 has a slightly different structure from the $CdCl_2$ type structure it has a similar spectrum. Powdered samples are shown to yield misleading results due to the finite size of the platelets forming the powder and the preferred orientation of the platelets.

1. Introduction

$CdCl_2$ type crystals are excellent hosts for the study of magnetic ions (Mn^{2+}, Fe^{2+}, Co^{2+}, Ni^{2+}) as isolated magnetic ions, as ion pairs and as clusters in the magnetically ordered lattices.

These crystals may be considered close packed layers of anions with a hexagonal layer of metal ions sandwiched between every second pair of anion layers. Lockwood (1973) has carried out a factor group analysis for this type of lattice (D_{3d}) to show that there are two Raman-active (E_g and A_{1g}) and two infrared-active modes (E_u and A_{2u}) in the long-wavelength limit ($k = 0$). Each infrared-active mode has transverse optical (TO) and longitudinal optical (LO) components.

The two Raman-active mode frequencies are comparatively easily determined and are unambiguously assigned on the basis of polarisation studies (Lockwood 1973). In contrast, the infrared-active modes have not been determined precisely, because the very strong absorption of these modes has required previous workers to study powdered samples dispersed in polyethylene or nujol (Lockwood 1973, Pollini *et al* 1980, Anderson *et al* 1981). The spectra reported by these authors show the infrared-active modes as two broad overlapping bands. Fröhlich (1948) and Martin (1970) have shown that for powdered samples of ionic crystals the fundamental absorption does not occur at the transverse optical frequency of the crystal, but between this and the longitudinal optical frequency. Furthermore the frequency of maximum absorption also depends on the embedding media.

---

† Work done in partial fulfilment of the requirements for the MSc Dissertation of R E M Vickers.

0022-3719/83/050999 + 10 $02.25

Campbell (1978) used a sellotape stripping technique to produce very thin (typically 5 μm) films of single crystals of $CdBr_2$ to obtain unambiguously the E_u(TO) mode. This technique has now been extended to reveal other infrared-active modes.

Section 2 presents the theory behind the interpretation of the results and § 3 gives the experimental techniques. Section 4 gives the results of thin-film, single-crystal, infrared transmission experiments and compares the spectra obtained with theoretical curves deduced from first principles.

2. Theory

The layered $CdCl_2$ structure has D_{3d}^5 symmetry with a trigonal axis (the c axis) perpendicular to the plane of the layers. The two infrared-active modes of vibration are the 'in-plane' E_u mode and the 'out-of-plane' A_{2u} mode (figure 1). Both of these modes have transverse optical (TO) and longitudinal optical (LO) components.

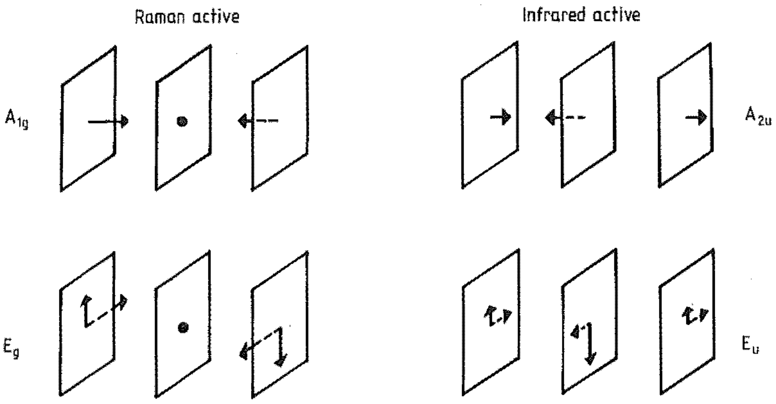

Figure 1. Symmetry coordinates for the long-wavelength optical modes of $CdCl_2$. The planes represent a plane of cadmium ions sandwiched between two planes of chloride ions.

Born and Huang (1954) have derived an expression for the transmission of radiation at normal incidence through thin films of isotropic dielectric, by matching the electric and magnetic fields of the radiation across the film surfaces. They showed that very thin films have a transmission minimum at the transverse optical phonon frequency ω_{TO}.

The results were generalised by Berreman (1963) for the case of non-normal incidence. For radiation polarised with the electric vector normal to the plane of incidence (the s wave) the transmission minimum is at the transverse optical frequency (ω_{TO}) while for radiation polarised with the electric vector in the plane of incidence (the p wave) an additional minimum occurs at the longitudinal optical frequency (ω_{LO}).

These results of Berreman (1963) can be generalised further to the case of anisotropic crystals with axial symmetry as follows.

The dielectric constant ε, the damping constant γ and both the ω_{TO} and ω_{LO} vibration frequencies have different values parallel and perpendicular to the crystal c axis and these components are specified by the subscripts $\|$ and $\perp$ respectively.

For the case of a thin film ($d \ll \lambda$), with the c axis normal to the surface, and with radiation incident at an angle θ to the normal, the transmission ratio for the p-polarised wave is

$$T_p = \left[1 + \frac{\omega^2 d}{c}\left(\frac{\sin^2\theta}{\cos\theta}\frac{\gamma_\parallel}{\varepsilon_{\infty\parallel}}\frac{(\omega_{LO\parallel}^2 - \omega_{TO\parallel}^2)}{(\omega_{LO\parallel}^2 - \omega^2)^2 + \gamma_\parallel^2\omega^2}\right.\right.$$
$$\left.\left. + \frac{\gamma_\perp\varepsilon_{\infty\perp}\cos\theta(\omega_{LO\perp}^2 - \omega_{TO\perp}^2)}{(\omega_{TO\perp}^2 - \omega^2)^2 + \gamma_\perp^2\omega^2}\right)\right]^{-1}$$

while for the s-polarised wave

$$T_s = \left(1 + \frac{\omega^2 d}{c}\frac{\gamma_\perp\varepsilon_{\infty\perp}}{\cos\theta}\frac{(\omega_{LO\perp}^2 - \omega_{TO\perp}^2)}{(\omega_{LO\perp}^2 - \omega^2)^2 + \gamma_\perp^2\omega^2}\right)^{-1}.$$

Here d is the film thickness and c is the vacuum speed of light. The p-wave transmission ratio has a minimum at both $\omega = \omega_{LO\parallel}$ and $\omega = \omega_{TO\perp}$, while the s-wave transmission ratio has a minimum at $\omega = \omega_{TO\perp}$ only. For unpolarised light both transmission minima are expected. For $CdCl_2$ type crystals these minima are expected to be at the frequencies of the E_u(TO) and the A_{2u}(LO) lattice vibration modes.

For the case of the crystal c axis parallel to the film surface and normal to the plane of incidence the transmission ratio for the p-polarised wave is

$$T_p = \left[1 + \frac{\omega^2 d}{c}\left(\frac{\sin^2\theta}{\cos\theta}\frac{\gamma_\perp}{\varepsilon_{\infty\perp}}\frac{(\omega_{LO\perp}^2 - \omega_{TO\perp}^2)}{(\omega_{TO\perp}^2 - \omega^2)^2 + \gamma_\perp^2\omega^2} + \frac{\gamma_\perp\varepsilon_{\infty\perp}\cos\theta(\omega_{LO\perp}^2 - \omega_{TO\perp}^2)}{(\omega_{TO\perp}^2 - \omega^2)^2 + \gamma_\perp^2\omega^2}\right)\right]^{-1}$$

having minima at E_u(LO) and E_u(TO) mode frequencies, while for the s-polarised wave

$$T_s = \left(1 + \frac{\omega^2 d}{c}\frac{\gamma_\parallel\varepsilon_{\infty\parallel}}{\cos\theta}\frac{(\omega_{LO\parallel}^2 - \omega_{TO\parallel}^2)}{(\omega_{TO\parallel}^2 - \omega^2)^2 + \gamma_\parallel^2\omega^2}\right)^{-1}$$

having a minimum at the A_{2u}(TO) mode frequency.

For the case of the crystal c axis parallel to the film surface and parallel to the plane of incidence

$$T_p = \left(1 + \frac{\omega^2 d}{c}\left|\frac{\sin^2\theta}{\cos\theta}\frac{\gamma_\perp}{\varepsilon_{\infty\perp}}\frac{(\omega_{LO\perp}^2 - \omega_{TO\perp}^2)}{(\omega_{LO\perp}^2 - \omega^2)^2 + \gamma_\perp^2\omega^2} + \frac{\gamma_\parallel\varepsilon_{\infty\parallel}\cos\theta(\omega_{LO\parallel}^2 - \omega_{TO\parallel}^2)}{(\omega_{TO\parallel}^2 - \omega^2)^2 + \gamma_\parallel^2\omega^2}\right|\right)^{-1}$$

having minima at E_u(LO) and A_{2u}(TO) mode frequencies and

$$T_s = \left(1 + \frac{\omega^2 d}{c}\frac{\gamma_\perp\varepsilon_{\infty\perp}}{\cos\theta}\frac{(\omega_{LO\perp}^2 - \omega_{TO\perp}^2)}{(\omega_{TO\perp}^2 - \omega^2)^2 + \gamma_\perp^2\omega^2}\right)^{-1}$$

having a minimum at the E_u(TO) mode frequency.

If a thin film of thickness much less than the wavelengths used is deposited on a metal surface then the mode associated with vibrations parallel to the metal surface is not excited because the component of the electric field parallel to the metal surface is zero at the metal surface. This technique was used by Berreman (1963) to observe the LO mode of alkali halide crystals. For reflection of radiation from a thin film deposited on a metal the following expressions are obtained when the c axis is perpendicular to the film surface:

$$R_s = 1$$

$$R_p = \left(1 - 2\frac{\omega^2 d}{c}\frac{\gamma_\parallel}{\varepsilon_{\infty\parallel}}\frac{(\omega_{LO\parallel}^2 - \omega_{TO\parallel}^2)}{(\omega_{LO\parallel}^2 - \omega^2)^2 + \gamma_\parallel^2\omega^2}\right)\Big/\left(1 + 2\frac{\omega^2 d}{c}\frac{\gamma_\parallel}{\varepsilon_{\infty\parallel}}\frac{(\omega_{LO\parallel}^2 - \omega_{TO\parallel}^2)}{(\omega_{LO\parallel}^2 - \omega^2)^2 + \gamma_\parallel^2\omega^2}\right).$$

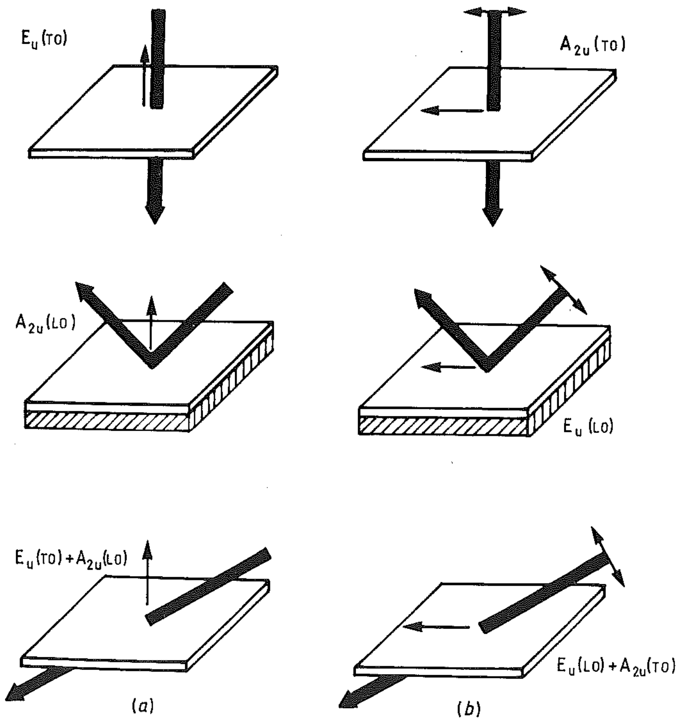

Figure 2. Configurations for obtaining all four infrared-active modes unambiguously from thin-film spectra. The narrow single-ended arrow shows the crystal *c* axis, the broad arrow the beam direction and the double-ended arrow the polarisation of the beam where necessary. The metal reflector is hatched. It was not possible to produce thin enough films for the configurations in column (*b*).

Hence reflectivity spectra for thin films with the *c* axis perpendicular to the film surface yield only the A_{2u}(LO) mode.

Figure 2 shows the experimental configurations that may be used to identify all four infrared-active modes.

3. Experimental

The $CdCl_2$ type powders were first dried in a heated vacuum oven and then purified by passing dry HCl or HBr, as appropriate, through the molten material prior to sealing the material in quartz ampoules. Single crystals were grown by lowering the ampoules through a sharp temperature gradient as in the Bridgeman–Stockbarger technique. As most of the crystals are hygroscopic, the ampoules were opened and the samples prepared inside a dry box maintained at less than 15% humidity.

Because the crystals cleave easily along planes perpendicular to the *c* axis the samples were prepared by pressing sellotape against a freshly cleaved crystal surface and peeling off the sellotape. A thin layer of crystal adheres to the sellotape. Thinner samples can be prepared by sticking another piece of sellotape to the thin film and then peeling the two pieces of sellotape apart. The samples may then be covered with clear nail varnish to prevent hydration whilst transferring the sample from the dry box to the low-temperature dewar.

Powder samples were prepared by grinding a single crystal with a mortar and pestle and then sprinkling the resultant powder onto sellotape. Excess powder is scraped off with a razor blade.

The reflection experiments required thin films of crystal to be in close contact with a metal substrate. This was achieved using the Rutherford approach by compressing a layer of crystal between two aluminium plates using a hydraulic ram. A thin layer of crystal adhered to the metal plates. Surplus material was peeled off one of the plates leaving a very thin film in direct contact with the metal. However, this technique did not yield reproducible samples, so it was eventually dropped in favour of the tilted-sample transmission method which yields the E_u(TO) mode as well as the A_{2u}(LO) mode.

Far-infrared spectra were recorded using a Grubb–Parsons Model IS-3 Fourier transform spectrometer, with a ^{3}He-cooled, doped germanium bolometer as a detector. All samples were immersed in liquid helium at 1.7 K. Transmission spectra were taken using unpolarised radiation incident at 60° and 0° (axial) with respect to the normal of the plane of the sample (figure 2(*a*)) and then ratioed against background spectra of sellotape and varnish only. For the reflection spectra, radiation was incident at 45° to the normal and the spectra were ratioed against background spectra obtained from reflection from an identical metal substrate only. In all cases the beam was not collimated and had a beam spread of approximately 8° either side of the beam direction.

4. Discussion

4.1. $CdCl_2$ type crystal

The different configurations used for taking spectra of thin films with the crystal *c* axis perpendicular to the plane of the sample are given in figure 2(*a*). Figure 3(*a*) shows the spectra obtained for the $CdBr_2$ samples. The axial spectrum shows unambiguously the E_u(TO) mode at $113 \pm 1\ \mathrm{cm}^{-1}$ with a linewidth (FWHM) of $10\ \mathrm{cm}^{-1}$.

The reflection spectrum shows the A_{2u}(LO) mode at 182 ± 2 with a linewidth (FWHM) of $15\ \mathrm{cm}^{-1}$. The sample for this configuration is difficult to reproduce and has several drawbacks. The E_u(TO) mode is not completely eliminated due to the sample being too thick; the A_{2u}(LO) absorption line has a wide bottom indicating that the crystal does not cover all the sample area; the centre of this line also occurs below the A_{2u}(LO) absorption as found in the spectrum where radiation is incident at 60°. This is consistent with the observation that the sample is coloured white indicating that in compressing the crystal onto the metal plate the film is extensively fissured and thus behaves much like a powdered sample.

Because of the above difficulties it was found that more accurate and reproducible results could be obtained using tilted thin-film samples where radiation is incident on the film at 60° to the normal. Both the E_u(TO) and A_{2u}(LO) modes are observed with the A_{2u}(LO) line being at $184 \pm 1\ \mathrm{cm}^{-1}$ with linewidth $8\ \mathrm{cm}^{-1}$.

The shape of these spectra are in fair agreement with the theoretical expressions of § 2 as shown in figure 4. All of the unknown parameters (dielectric constant ε_∞, film thickness d, and unmeasured modes $\omega_{\mathrm{LO}\perp}$, $\omega_{\mathrm{TO}\parallel}$) were grouped into one constant. This constant and γ were varied in order to produce a best fit.

Unfortunately it was not possible to produce suitable samples for the experimental configurations shown in figure 2(*b*) where the crystal *c* axis is in the plane of the sample. The easy crystal cleavage plane in this case was perpendicular to the sample plane and

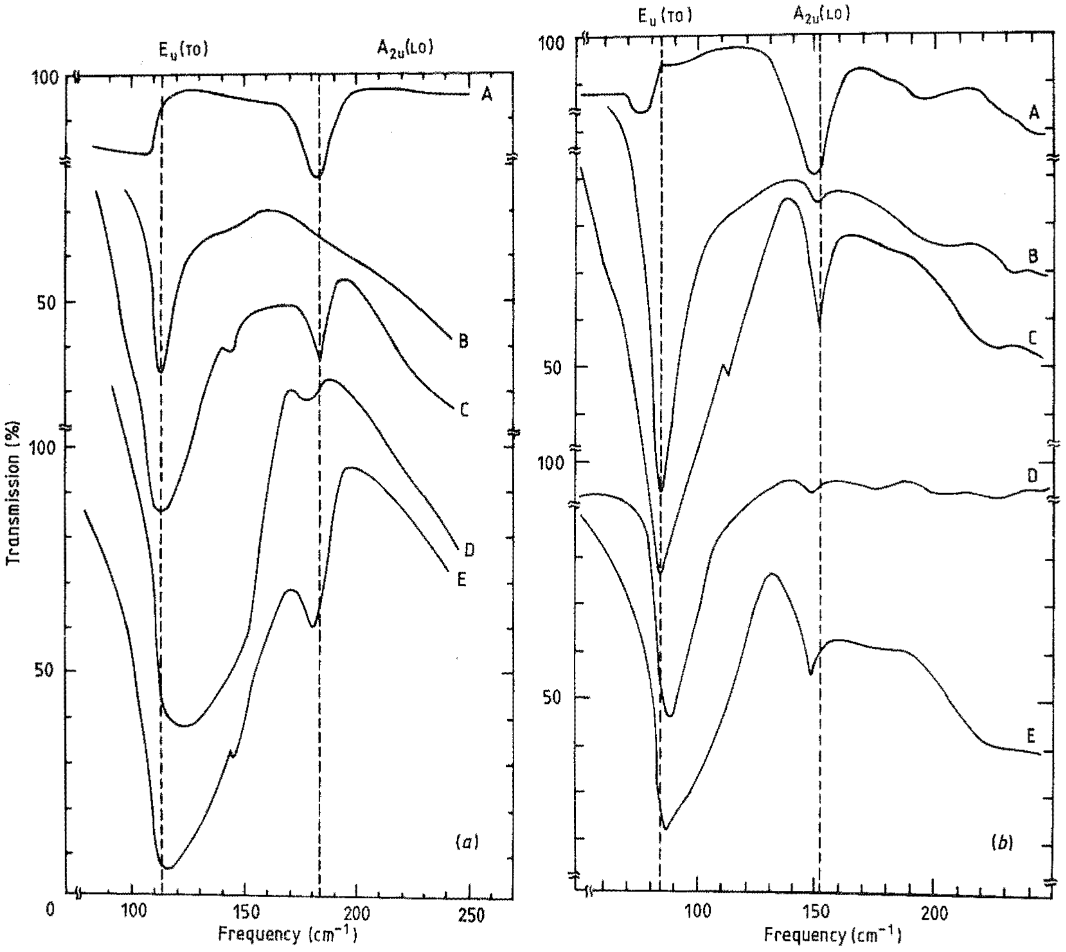

Figure 3. Comparison of thin-film spectra for (*a*) $CdBr_2$ and (*b*) CdI_2 obtained using the various experimental configurations shown in figure 2(*a*). All samples were at 1.7 K with spectral resolution of 1 cm^{-1} for transmission spectra and 2 cm^{-1} for reflection spectra. A, thin-film reflection; B, axial; C, tilted 60°; D, powder 0°; E, powder, tilted 60°.

such samples could not be produced quite thin enough without breaking up. Hence the E_u(LO) and A_{2u}(TO) mode frequencies could not be measured in this work.

The powder spectra for normal incidence shows a strong absorption near the E_u mode and a much weaker absorption near the A_{2u} mode. When radiation is incident at 60° the A_{2u} mode absorption is much more pronounced. This indicates that the powders have a preferred orientation. Electron microscope pictures show that the powder consists of small platelets of approximately 20 μm across, lying flat on the sellotape surface. This may account for the difficulties some authors have in resolving the A_{2u} mode in powder spectra. The absorption frequency for the E_u mode (116 cm^{-1} is just above the single crystal E_u(TO) mode (113 cm^{-1}) and the A_{2u} mode (180 cm^{-1}) is just below the crystal A_{2u}(LO) mode (184 cm^{-1}). This behaviour is consistent with the work of Martin (1970) on alkali halide powders.

Figure 5 shows the 60° spectra for a range of single-crystal films. The samples are thicker than those used for the axial spectra, in order to emphasise the A_{2u}(LO) mode.

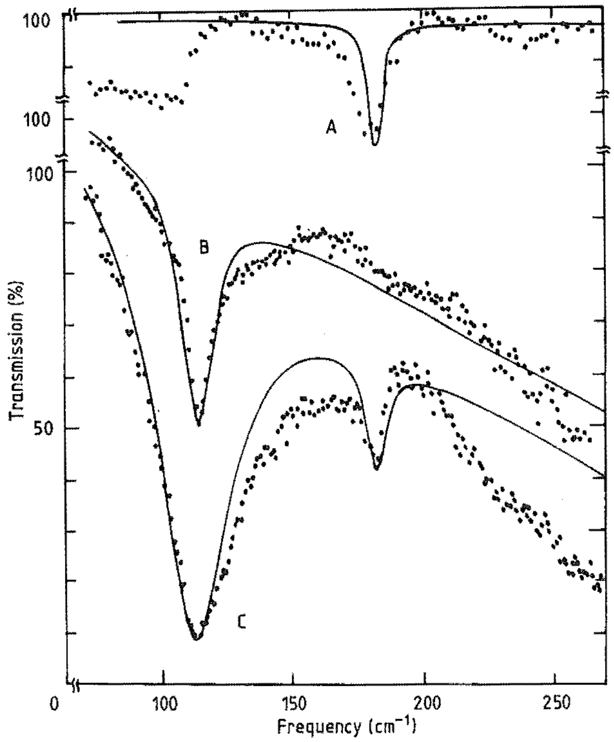

Figure 4. Theoretical fit (full curves) to experimental points (dots) for thin-film spectra of $CdBr_2$ using the expressions derived in § 2. A, reflection, $\gamma_\parallel = 6\,cm^{-1}$; B, axial, $\gamma_\perp = 10\,cm^{-1}$; C, tilted 60°, $\gamma_\perp = 10\,cm^{-1}$, $\gamma_\parallel = 6\,cm^{-1}$.

Table 1. Lattice modes of $CdCl_2$ and CdI_2 type crystals at liquid helium temperatures. E_u(TO) and A_{2u}(LO) are the infrared-active modes measured in this work from thin film spectra. The uncertainty of measurement is less than $\pm 1\,cm^{-1}$. Typical linewidths (FWHM) are less than $15\,cm^{-1}$. The frequencies of the Raman-active modes (E_g, A_{1g}) previously reported by other workers are also listed.

Compound	E_u(TO)	A_{2u}(LO)	E_g	A_{1g}	ref for E_g, A_{1g}
CdI_2	85	153	49	115	a
$CdBr_2$	113	184	81	151	b
$CdCl_2$	156	239	135	236	b
$MgCl_2$	250 ± 3	—	155	246	c
$MnCl_2$	184	287	150	242	b
$FeCl_2$	201	293	141	250	d
$CoCl_2$	213	292	157	253	e
$NiCl_2$	231	304	175	271	f
$CoBr_2$	167	235	98	161	g
$NiBr_2$	186	234	108†	169†	h

[a] Hayashi *et al* (1981)
[b] Christie (1973) (Co doped crystals)
[c] Jones and Tomblin (1978)
[d] Johnstone *et al* (1978)
[e] Christie and Lockwood (1971)
[f] Lockwood *et al* 1979a
[g] Lockwood *et al* (1979b)
[h] C W Tomblin (private communication)

† Liquid air temperature

The $CoCl_2$ spectrum shows evidence of water attack. A $CoCl_2$ film that was allowed to hydrate showed strong absorption lines at 150, 190, 220 and 260 cm^{-1} which correspond to the extra inflections and absorption lines in the spectrum shown. This made it difficult, if not impossible, to identify the weaker A_{2u}(LO) mode in the more hygroscopic crystals.

Table 1 gives the values for the E_u(TO) and A_{2u}(LO) modes measured in this work and, for comparison, the low-temperature Raman-active modes (E_g, A_{1g}) reported by previous workers. The linewidths of the infrared-active modes for all thin film samples were less than 15 cm^{-1} (FWHM) the narrowest being 7 cm^{-1} for the A_{2u}(LO) mode of $CdCl_2$. These appear to be much broader than the widths reported for the Raman-active modes which are usually resolution-limited below 12 K and hence are typically less than 2 cm^{-1} wide (Christie 1973, Johnstone *et al* 1978).

4.2. CdI_2

CdI_2 has a slightly different structure from $CdCl_2$ if grown from the melt (Montero and Kiefer 1973, Wyckoff 1963). The difference is in the repeat distance of the halide layer

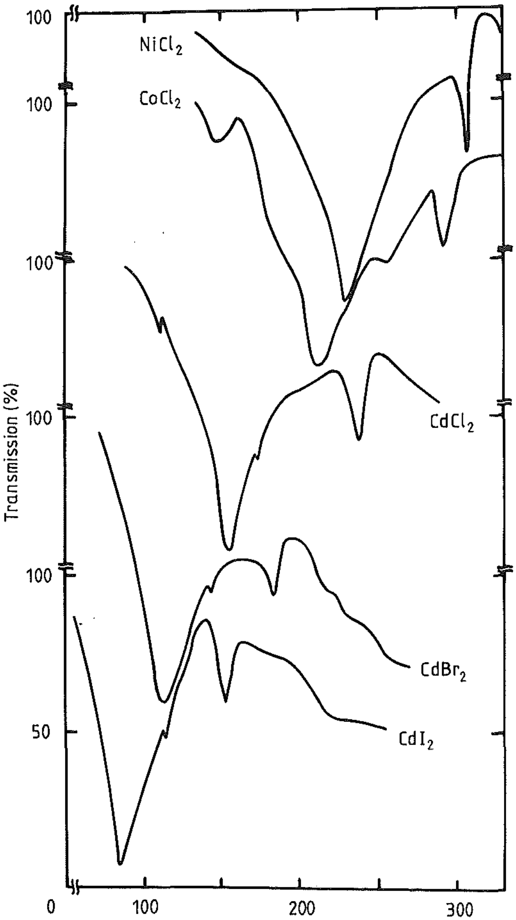

Figure 5. Thin-film absorption spectra of tilted samples of various metal dihalide crystals. Beam incident at 60° to the normal of the sample plane. Sample temperature 1.7 K. Resolution 1 cm^{-1}.

positions. In $CdCl_2$ every third chlorine layer is in an equivalent position, while in CdI_2 every fourth iodine layer is in an equivalent position. CdI_2 has a space group C_{6v}^4 which gives seven Raman-active modes and four infrared-active modes. Montero and Kiefer (1973) found only three Raman lines.

Nakashima (1975) and Zallen and Slade (1975) have both studied PbI_2 which has similar polytypes to CdI_2. Their work shows how PbI_2 transforms from the structure D_{3d}^3 to C_{6v}^4. Nakashima (1975) concludes that the space group C_{6v}^4 is equivalent to D_{3d}^3if the nearest-neighbour iodine layer interactions are small.

Figures 3 and 5 show that the infrared absorption spectrum of CdI_2 has the same general features as that of the $CdCl_2$ type crystals. This reinforces the view that as far as the $k = 0$ modes are concerned the important feature of these layered compounds is the basic I–Cd–I sandwich with strong forces between ions in this sandwich and only weak van der Waals bonding with the anions of adjacent sandwiches.

Lucovsky and White (1977) have reported room-temperature infrared reflection spectra of CdI_2 single crystals and fitted the reststrahlen bands using a dielectric function constructed from damped lorentzian oscillators. Their room-temperature results for the E_u(TO) (79 cm^{-1}) and A_{2u}(LO) (152 cm^{-1}) modes are within 6 cm^{-1} of the low-temperature values obtained by direct methods in this paper. This is quite good agreement since 6 cm^{-1} is a typical increase in frequency for $CdCl_2$ type lattice modes as the sample temperature is reduced from room temperature to that of liquid helium (Campbell 1978).

5. Conclusions

Expressions have been derived for the transmission at non-normal incidence of infrared radiation through thin films of anisotropic crystals. The sellotape stripping technique has proved to be a very convenient method for producing thin films of the metal halide layered structures with a crystal *c* axis perpendicular to the plane of the film. Such films yield unambiguously the frequencies of the E_u(TO) and A_{2u}(LO) infrared-active modes.

The nature of the easy cleavage planes in these materials precludes the fabrication of sufficiently thin films with the *c* axis in the plane of the film. This has meant that the frequencies of the E_u(LO) and A_{2u}(TO) modes cannot be determined directly by the same method. Measurement of the anisotropic dielectric constants at high and low frequencies would allow the frequencies of these modes to be deduced through use of the Lyddane–Sachs–Teller relation modified for anisotropic crystals as has been done by Richman *et al* (1963) for $LaCl_3$. Another indirect method is to measure the reflectivity from a bulk crystal as Lucovsky and White (1976) have done for CdI_2.

Transmission spectra of powdered samples are shown to give misleading results which must be corrected for the finite size of the sample, the possibility of a preferred orientation of the platelets forming the powder and the effect of the embedding medium.

Acknowledgments

This work was supported by the New Zealand University Grants Committee. The authors are indebted to Dr G D Jones, Dr R W G Syme and Dr Z Schlesinger (Cornell) for many helpful discussions and C W Tomblin for measuring the low-temperature Raman-active modes of $NiBr_2$.

References

Anderson A, Lo Y W and Todoeschuck J P 1981 *Spectrosc. Lett.* **14** 105–16
Benedek G, Pollini I, Piseri L and Tubino R 1979 *Phys. Rev.* B **20** 4303–7
Berreman D W 1963 *Phys. Rev.* **130** 2193–8
Born M and Huang K 1954 *Dynamical Theory of Crystal Lattices* (London: Oxford University Press) pp 124–5
Campbell J A 1978 *J. Phys. C: Solid State Phys.* **11** L795–7
Christie J H 1973 *PhD Thesis* University of Canterbury, NZ
Christie J H and Lockwood D J 1971 *Proc. 2nd Int. Conf. on Light Scattering in Solids* 145–50
Fröhlich H 1948 *Theory of Dielectrics* 2nd edn (London: Oxford University Press) pp 153–5
Hayashi T, Ohata T and Koshino S 1981 *Solid State Commun.* **38** 845–7
Johnstone I W, Lockwood D J and Mischler G 1978 *J. Phys. C: Solid State Phys.* **11** 2147–64
Jones G D and Tomblin C W 1978 *Phys. Rev.* B **18** 5990–4
Lockwood D J 1973 *J. Opt. Soc. Am.* **63** 374–82
Lockwood D J, Bertrand D, Carrara P, Mischler G, Billerey D and Terrier C 1979a *J. Phys. C: Solid State Phys.* **12** 3615–20
Lockwood D J, Mischler G, Johnstone I W and Schmidt M C 1979b *J. Phys. C: Solid State Phys.* **12** 1955–75
Lucovsky G and White R M 1977 *Nuovo Cim.* **38**B 291–9
Martin T P 1970 *Phys. Rev.* B **1** 3480–8
Montero S and Keifer W 1973 *J. Raman Spectrosc.* **1** 565–72
Nakashima S 1975 *Solid State Commun.* **16** 1059–62
Pollini I, Spinolo G and Benedek G 1980 *Phys. Rev.* B **22** 6369–90
Richman I, Satten R A and Wong E 1963 *J. Chem. Phys.* **39** 1833–46
Wyckoff R W G 1963 *Crystal Structures* vol 1, 2nd edn (New York: Wiley–Interscience) pp 266–75
Zallen R and Slade M L 1975 *Solid State Commun.* **17** 1561–6

REFERENCES

1. J.F. Ackerman, G.M. Cole and S.L. Holt, Inorganica Chimica Acta, 8 323 (1974).
2. R.J. Bell, Introductory Fourier Transform Spectroscopy, Academic Press, New York (1972).
3. D.W. Berreman, Phys. Rev., 130 2193 (1963).
4. M. Born and H. Huang, Dynamical Theory of Crystal Lattices, Clarendon Press, Oxford (1954).
5. G. Burns, Introduction of Group Theory with Applications, Academic Press, New York (1977).
6. W. Brietling, W. Lehmann, T.P. Srinivasan, R. Weber and U. Durr, Solid State Comm., 24 267 (1977).
7. A. Brun, P. Mayer and B. Brait, J. Phys. C : Solid State Phys., 13 5775 (1980).
8. J.A. Campbell, Ph.D. Thesis (1968).
9. J.A. Campbell and R.E.M. Vickers, J. Phys. C : Solid State Phys., 16 999 (1983).
10. J.A. Campbell, private communication.
11. A. Chadwick, J.T.R. Dunsmuir, I.W. Forrest and A.P. Lane, J. Chem. Soc.(A), 2794 (1971).
12. W. Cochran and R.A. Cowley, J. Phys. Chem. Solids, 23 447 (1962).
13. B.T. Draine and A.J. Sievers, Optic Comm., 16 425 (1976).
14. H.D. Drew and A.J. Sievers, Applied Optics, 8 2067 (1969).
15. U. Fano, Phys. Rev., 124 1866 (1961).
16. M.L. Forman, J. Opt. Soc. Amer., 56 978 (1966).
17. H. Frohlich, Theory of Dielectrics, London : Oxford University Press (1948).

18. C. Gouth, Phys. Bull., 36 196 (1985).

19. R.T. Hall and J.M. Dowling, J. Chem. Phys., 47 2454 (1967)

20. I.W. Johnstone and L. Dubicki, J. Phys. C : Solid State Phys., 13 4531 (1980a).

21. I.W. Johnstone, D.J. Lockwood and M.W.C. Dharma-Wardana, Solid State Comm., 36 593 (1980b).

22. I.W. Johnstone, G.D. Jones and D.J. Lockwood, Solid State Comm. 39 395 (1981).

23. R. Jorke and U. Durr, J. Phys. C : Solid State Phys., 16 L1129 (1983).

24. T. Kurosawa, J. Phys. Soc. Japan, 16 1298 (1961).

25. H. Kishishita and Y. Kaifu, J. Phys. Soc. Japan, 33 142 (1972).

26. W.P. Lehmann, W. Breitling and R. Weber, J. Phys. C : Solid State Phys., 14 4655 (1981).

27. D.J. Lockwood, I.W. Johnstone, H.J. Labbe and B. Brait, J. Phys. C : Solid State Phys., 16 6451 (1983)

28. J.M. Longo and J.A. Kafalas, J. Solid State Chem., 1 103 (1969).

29. T.P. Martin, Phys. Rev. B, 1 3480 (1970).

30. L. Mertz, Transforms in Optics, Wiley, New York (1965).

31. G.L. McPherson and J.R. Chang, Inorg. Chem., 12 1196 (1973).

32. M. Melamud, H. Pinto, J. Makovsky and H. Shaked, Phys. Stat. Sol. (b), 63 699 (1974).

33. S.E. Nagler, W.J.L. Buyers, R.L. Armstrong and B. Brait, Phys. Rev. B 27 1784 (1983).

34. S. Nakajima, Y. Toyozawa, R. Abe, The Physics of Elementary Excitations, Springer-Verlag, Berlin, Heidelberg, New York (1980).

35. H.H. Sample and L.G. Rubin, Cryogenics, 17 597 (1977).

36. H. Shiba, Prog. of Theor. Phys., 64 466 (1980.

37. M.J. Taylor, Phys. Rev. Lett., 23 405 (1969).

38. R.E.M. Vickers, M.Sc. Thesis, University of Canterbury (1981).

39. D. Walton, T. Timusk and A.J. Sievers, Rev. Scient. Inst., 42 8 (1971).

40. S. Zwerdling, R.A. Smith and J.P. Theriault, Infrared Phys., 8 271 (1968).